Cu-catalyzed Chemical Vapour Deposition of Graphene: Synthesis, Characterization and Growth Kinetics

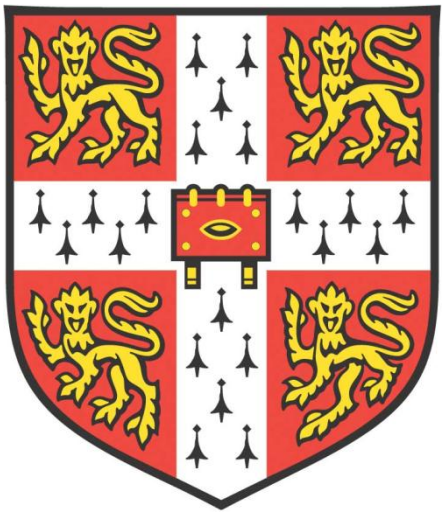

Xingyi Wu

St John's College

Electrical Engineering Division

Department of Engineering

University of Cambridge

This dissertation is submitted for the degree of Doctor of Philosophy

September 2017

This is for you, Dad.

DECLARATION

This dissertation is the result of my own work and includes nothing, which is the outcome of work done in collaboration except as declared in the Preface and specified in the text. It is not substantially the same as any that I have submitted, or, is being concurrently submitted for a degree or diploma or other qualification at the University of Cambridge or any other University or similar institution except as declared in the Preface and specified in the text. I further state that no substantial part of my dissertation has already been submitted, or, is being concurrently submitted for any such degree, diploma or other qualification at the University of Cambridge or any other University or similar institution except as declared in the Preface and specified in the text.

In accordance with the Department of Engineering guidelines, this thesis contains about 41,916 words and 61 figures, which do not exceed the length limit (65,000 words and 150 figures).

Xingyi Wu

Department of Engineering, University of Cambridge

Signed:_____

Date:_____

CU-CATALYZED CHEMICAL VAPOUR DEPOSITION OF GRAPHENE: SYNTHESIS, CHARACTERIZATION AND GROWTH KINETICS

Xingyi Wu

Graphene is a two dimensional carbon material whose outstanding properties have been envisaged for a variety of applications. Cu-catalyzed chemical vapour deposition (Cu-CVD) is promising for large scale production of high quality monolayer graphene. But the existing Cu-CVD technology is not ready for industry-level production. It still needs to be improved on some aspects, three of which include synthesizing industrially useable graphene films under safe conditions, visualizing the domain boundaries of the continuous graphene, and understanding the kinetic features of the Cu-CVD process. This thesis presents the research aiming at these three objectives. By optimizing the Cu pre-treatments and the CVD process parameters, continuous graphene monolayers with the millimetre-scale domain sizes have been synthesized. The process safety has been ensured by delicately diluting the flammable gases. Through a novel optical microscope set up, the spatial distributions of the domains in the continuous Cu-CVD graphene films have been directly imaged and the domain boundaries visualised. This technique is non-destructive to the graphene and hence could help manage the domain boundaries of the large area graphene. By establishing the novel rate equations for graphene nucleation and growth, this study has revealed the essential kinetic characteristics of general Cu-CVD processes. For both the edge-attachment-controlled and the surface-diffusion-controlled growth, the rate equations for the time-evolutions of the domain size, the nucleation density, and the coverage are solved, interpreted, and used to explain various Cu-CVD experimental results. The continuous nucleation and inter-domain competitions prove to have non-trivial influences over the growth process. This work further examines the temperature-dependence of the graphene formation kinetics leading to a discovery of the internal correlations of the associated energy barriers. The complicated effects of temperature on the nucleation density are explored. The criteria for identifying the rate-limiting step is proposed. The model also elucidates the kinetics-dependent formation of the characteristic domain outlines. By accomplishing these three objectives, this research has brought the current Cu-CVD technology a large step forward towards practical implementation in the industry level and hence made high quality graphene closer to being commercially viable.

ACKNOWLEDGEMENTS

I wish to thank my supervisor Prof. John Robertson who has been providing me advice since the start of my PhD at University of Cambridge. His lifelong passion for science has encouraged me to keep progressing. I am particularly indebted to Dr. Guofang Zhong for the daily supervision. His experience and insight in the field of chemical vapour deposition have taught me many experimental techniques and inspired many of my research ideas. I also wish to thank my advisor Prof. Stephan Hofmann who has motivated me to purse high quality research through his critical comments. I would like to thank Dr. Girish Rughoobur for training me in Matlab coding and showing me many experimental tricks. I also want to thank Dr. Yuzheng Guo, Dr. Xiaoming Yu, Hongfei Li, and Shan Zheng for useful discussions and helping me fit into the study and life in Cambridge.

Likewise I am thankful to Dr. Lorenzo D'Arsiè for helping me with Raman spectroscopy and charge carrier mobility measurements and to Dr. Alex W Robertson for the transmission electron microscopy characterization. I am grateful to Dr. Hisashi Sugime, Dr. Santiago Esconjauregui, and Dr. David Hasko for their professional advice on the material science. I also would like to thank Dr. Xingya Bian, Guohua Hu, Dr. Sabina Caneva and Haichang Lu for their friendship.

I also wish to acknowledge the Cambridge Trust for providing the scholarship.

Finally, I would like to thank my family for their understanding and constant love.

Thank you all.

LIST OF PUBLICATIONS

Peer-reviewed Journal Publications (during PhD study)

1. **Low Temperature Growth of Fully Covered Single-layer Graphene Using CoCu Catalyst** Hisashi Sugime, Lorenzo D'Arsié, Santiago Esconjauregui, Guofang Zhong, Eugen Hildebrandt, Xingyi Wu, Hikmet Sezen, Matteo Amati, Luca Gregoratti, Robert S. Weatherup, and John Robertson. Accepted by *Nanoscale*, (2017). DOI: 10.1039/C7NR02553J.

2. **Graphene-PVDF Multi-functional Ultra-thin Film Based Multi-dimensional Touch Sensing System for Flexible Interactive Displays** Shuo Gao, Xingyi Wu, Hanbin Ma, John Robertson and Arokia Nathan. *ACS Applied Materials&Interfaces*, **9**, 18410 (2017)

3. **Metal-Catalyst-Free Growth of Graphene on Insulating Substrates by Ammonia-assisted Microwave Plasma-Enhanced Chemical Vapour Deposition** Shan Zheng, Guofang Zhong, Xingyi Wu, Lorenzo D'Arsié, and John Robertson. *RSC Advances*, **7**, 33185 (2017)

4. **Adsorptive Graphene Doping: Effect of a Polymer Contaminant** William E Arter , Lorenzo D'Arsié, Xingyi Wu, Santiago Esconjauregui , and John Robertson. *Applied Physics Letters*, **110**, 223104 (2017)

5. **Stable And Efficient P-Type Doping Of Graphene By Nitric Acid** Lorenzo D' Arsiè, Santiago Esconjauregui, Robert Weatherup, Xingyi Wu, William Emrys Arter, Hisashi Sugime, Cinzia Cepek, and John Robertson. *RSC Advances*, **6**, 113185 (2016)

6. **Growth of Continuous Graphene by Open Roll-to-Roll Chemical Vapor Deposition** Guofang Zhong, Xingyi Wu, Lorenzo D'Arsié, Kenneth B. K. Teo, Nalin L. Rupesinghe, Alex Jouvray, and John Robertson. *Applied Physics Letters*, **109**, 193103 (2016)

7. **Nondestructive Optical Visualization of Graphene Domains and Boundaries** Xingyi Wu, Guofang Zhong, and John Robertson. *Nanoscale*, **8**, 16427 (2016)

8. **Growth of Continuous Monolayer Graphene with Millimeter-sized Domains Using Industrially Safe Conditions** Xingyi Wu, Guofang Zhong, Lorenzo D'Arsié, Hisashi Sugime, Santiago Esconjauregui, Alex W Robertson, and John Robertson. *Scientific Reports*, **6**, 21152 (2016)

Conference Presentations (during PhD study)

1. Xingyi Wu, Guofang Zhong, Hongfei Li, Lorenzo D'Arsié, Hisashi Sugime, Santiago Esconjauregui, Alex W. Robertson, and John Robertson. '*Effect of Cu Oxidation on Growth of Continuous Monolayer Graphene with Millimeter-sized Domains*', **E-MRS Spring Meeting 2016**, Lille, France. (**oral presentation**)

2. Xingyi Wu, Guofang Zhong, Santiago Esconjauregui, Lorenzo D'Arsié, and John Robertson. *'Synthesis of Graphene by Chemical Vapour Deposition Using 2% Diluted Hydrogen*', **IWEPNM 2015**, Kirchberg/Tirol, Austria. (**poster presentation**)

CONTENTS

1 INTRODUCTION

1.1 Motivation

Material science has always been contributing new functional materials for applications that have penetrated many corners of human life. Over the past decade one of the most extensively studied materials is graphene, an archetypal two-dimensional (2D) carbon material. The very nature of merely few-atom thickness has brought graphene into the limelight since its debut by Novoselov and Geim in 2004.[1] Before this it has been held for more than 70 years that any 2D materials are thermodynamically unstable in ambient conditions.[2–4] The uniqueness of graphene lies in not only its novel 2D structure but also a plethora of outstanding properties making it a potential enabler for generating new products that might not be readily achieved by the conventional materials.[5] For instance, it has an ultra-large specific surface area but is chemically inert. It conducts electricity and heat better than metals, but is transparent and flexible similar to plastics. Combinational utilization of its unique properties has inspired influential applications in electronics,[6–11] photonics, optoelectronics,[12] sensors,[13–18]transparent conductive films,[19–21] energy harvesting and storage,[22–27] polymer nano-composites,[28–31]etc. It is thereby reasonable to expect that graphene has the potential to become one of the next-generation disruptive technology platforms that can contribute to a large number of material-and device-orientated sectors.

The prospects of the graphene-underpinned new technologies are conditional to a couple of challenges. One of the most fundamental challenges is to develop a comprehensive set of production-worthy synthesis protocols that can yield commercially viable graphene while still maintaining as many of its record properties as

possible. The synthesis of a material is always the starting point of the corresponding value chain and graphene is no exception. The crystalline quality of the synthesized graphene decides the performance of most graphene-based applications. Meanwhile the scalability and hence the cost of graphene synthesis process closely influences the capacity of the subsequent device integration. In principle an ideal synthesis method aiming at high-end use should produce graphene fulfilling a list of industrial demands. First of all the graphene itself needs to be of high quality. The somewhat ambiguous term 'high quality' in the case of graphene production indicates having the least amount of defects including carbon atom voids, sp^2 bond deformation, elemental impurities, contaminating adsorbates, domain boundaries, film wrinkles, cracks, etc.[32–37] The graphene film also needs to be continuous and uniformly monolayer across large area. This is intended to ensure a high yield and performance homogeneity of any functional device arrays integrated in contact with graphene. From the perspective of manufacturing optimisation, the synthesis process itself is expected to be safe, reproducible, scalable, and economic.

The simplest way to obtain monolayer to few-layer graphene is mechanical cleavage from bulk graphite via Scotch tape. This was first demonstrated in 2004 by Novoselov and Geim.[1] In the later years a variety of fabrication methods have emerged to produce graphene with tailored properties for specific purposes. These include epitaxial growth on SiC,[38,39] liquid phase exfoliation (LPE),[40–48] metal-catalyzed chemical vapour deposition (CVD),[49–53],etc. The mainstream method currently used in laboratories to prepare large area research-grade graphene is CVD using Cu as catalysts. The Ruoff's group[53] opened the Cu-CVD route in 2009 in their widely acknowledged work. It mainly involves the Cu-catalyzed conversion of the gaseous hydrocarbon precursors to the solid graphene films. Compared to other production methods, the Cu-CVD method is relatively advantageous because it can produce graphene with simultaneously large area,[21,54–56] monolayer uniformity,[53,57,58] and high crystalline quality.[59,60] Recent advancements along the Cu-CVD route has further developed controllable technologies that can tailor the graphene nucleation density, the domain size,[59,61–63] the domain shape,[64–69] the growth rate,[61–63,70–72] etc. These lead to the Cu-CVD growth of ultra-large single crystalline graphene domains up to inch-scale which is about four orders of magnitude larger than the mechanically cleaved graphene flakes (micrometer-scale).[62,73]

However there are still several hurdles remaining to be cleared before the Cu-CVD technology is ready to be up-scaled from the laboratory to the industry level.

(1) One of the key problems is associated with the control of the graphene domains and domain boundaries. The Cu-CVD-derived continuous graphene is intrinsically a polycrystalline film consisting of the randomly positioned and orientated domains.[74,75] The boundaries unavoidably emerge from the coalescence of the neighbouring domains.[53] The defective domain boundaries could significantly degrade the electrically-active devices through defect scattering.[35,76,77] Since the boundaries are distributed in a disordered manner, they could also impair the spatial homogeneity of the performances of the graphene-based device arrays. In this sense it is essential to appropriately manage the domain boundaries. This goal can be divided into two objectives. First, the areal density of the domain boundaries in the continuous graphene needs to be effectively reduced. This in principle can be achieved by improving the domain size as the areal density of the boundaries is inversely proportional to the average domain area. Most of the current research efforts have pertained to the laboratory-scale growth of isolated graphene single crystals with ultra-large domain size.[59,62,72,78–82] Yet only the graphene films that are simultaneously continuous and of large domain size are industrially useable. The CVD technology towards an acceptable balance between the film continuity and the domain size is still in its infancy. Second, it is scarcely possible to remove all the boundaries merely via optimizing the CVD process. A compensating solution is to spatially visualize the residual graphene domains and boundaries, which, if possible, can enable identification of the boundary-infected device units. Yet the existing domain visualisation methods for large area graphene always cause detrimental damage or contamination to graphne.[83–88] A non-destructive visualization method is extraordinarily appealing for reliable assessment of the boundary-induced adverse effects, but is hitherto lacking.

(2) Another issue is about the safety of the Cu-CVD process. The safety issue always deserves much attention in design of general manufacturing processes. For Cu-CVD of graphene this is of particular concern because it involves the use of the flammable gases such as H_2 and CH_4 at elevated temperature (~1000 °C). The concentration of the flammable gases used in the current synthesis recipes is typically within the explosive ranges. This imposes potential risk of explosion. A safe Cu-CVD recipe is thereby valuable for mass production and worth research consideration.

(3) The Cu-CVD graphene formation kinetics needs to be thoroughly investigated. Particularly, it is of paramount importance to universally model the time evolution of the graphene domain size, domain density and areal coverage (i.e., the product of the

domain size and density). This knowledge could guide the controllable engineering of the synthesis process and delicate tailoring of the graphene properties (e.g., domain size, density, growth rate, etc). On the one hand, the current modelling studies of the reaction kinetics have claimed disagreeing mathematical forms that are only applicable to each own data. On the other hand, the numerical simulations have principally concentrated on the atomistic-level science of graphene formation, relatively far from the technologic aspects.[89–97]Therefore an universal growth model for the general Cu-CVD kinetics is still lacking which shall be instructive to the design and control of the practical growth processes.

1.2 Research Objectives

The objectives of this thesis are (1) to establish an industrial useable and safe Cu-CVD recipe for synthesizing high quality, continuous monolayer graphene with millimetre-scale domain sizes, (2) to develop a non-destructive characterization technique for spatial visualization of the Cu-catalyzed graphene domains and boundaries, (3) to model the general kinetics of the Cu-catalyzed graphene nucleation and growth.

1.3 Thesis structure

This thesis presents the author's experimental and theoretical work on the development, characterization and understanding of the Cu-catalyzed CVD graphene for future industrial up-scaling.

Chapter 2 introduces the reader to the basics of graphene including its fundamental properties and the envisaged applications. The graphene synthesis methods are also reviewed with heightened emphasis on the Cu-CVD approach.

Chapter 3 summarizes the main experimental techniques used in this research. The setup of a thermal CVD system for graphene synthesis is detailed. The graphene transfer method using the wet Cu etching is demonstrated. The characterization techniques for investigating the CVD graphene quality are presented.

Chapter 4 demonstrates the optimization of the Cu-CVD method towards the growth of continuous monolayer graphene with millimetre-sized domains using industrially safe conditions (diluted H_2 and CH_4). With the concentration of H_2 and CH_4 constrained below the lower explosive limit, a combinational use of Cu electro-polishing, non-reductive annealing and CH_4/H_2 composition optimization is shown to enable the growth of industrially useable graphene films.

Chapter 5 describes the non-destructive optical visualization of Cu-supported graphene domains and boundaries. The setup of a custom-modified optical microscope (OM) enabling the visualization is detailed and its mechanism discussed. The novel star-like ridge sets of the Cu-supported graphene are observed using the modified OM. Based on the star-like ridge sets a prototypic visualization method is developed and its reliability discussed. The variety of the star-like ridge morphologies is demonstrated and its correlation with the underlying Cu crystallographic structure is explored.

Chapter 6 presents the author's theoretical study on the kinetics of Cu-catalyzed graphene formation. The universal growth equations are established for both the edge-attachment-controlled and the diffusion-controlled growth with the underlying assumptions investigated. The crucial parameters shaping the growth kinetics are identified and their physical meanings interpreted. The analytical solutions under certain asymptotic limits and the general numerical solutions are presented with mathematical details. The solutions are confirmed to enable unified fitting of a broad range of kinetic CVD data. The derived conclusions are used to address how the graphene formation process is affected by the real CVD conditions. The kinetic-driven formation of graphene domain outlines is also illustrated.

This thesis will be concluded in Chapter 7 by summarizing the results and findings. A concluding overview of the values and limitations of this work is presented followed by an outlook for future work.

2 LITERATURE SURVEY

2.1 Graphene and Its Properties

Graphene, in the context of material sciences, is normally referred to as planar sheets consisting of sp^2-bonded carbon atoms. Its characteristics can be defined from four aspects: (1) In terms of the elemental composition graphene is an allotrope of carbon. Its sibling allotropes include fullerenes, carbon nanotubes, diamond, graphite, etc (see Figure 2.1). (2) The carbon atoms of graphene are bonded in sp^2 configuration which intrinsically differs from the sp^3-bonding of some of its allotropes such as diamond. (3) The carbon atoms of graphene form a planar network while those of the carbon nanotubes, although both sp^2 bonded, form a cylindrical network. (4) The most widely mentioned graphene by default has monolayer carbon sheet. It has the strictly defined characteristics of a 2D material in contrast to graphite, which, having many layers of carbon sheet, is a conventional 3D structure. Those consisting of a few layers of stacked carbon sheets have properties close to the monolayer graphene and hence are also under academic interest, normally named few-layer graphene.

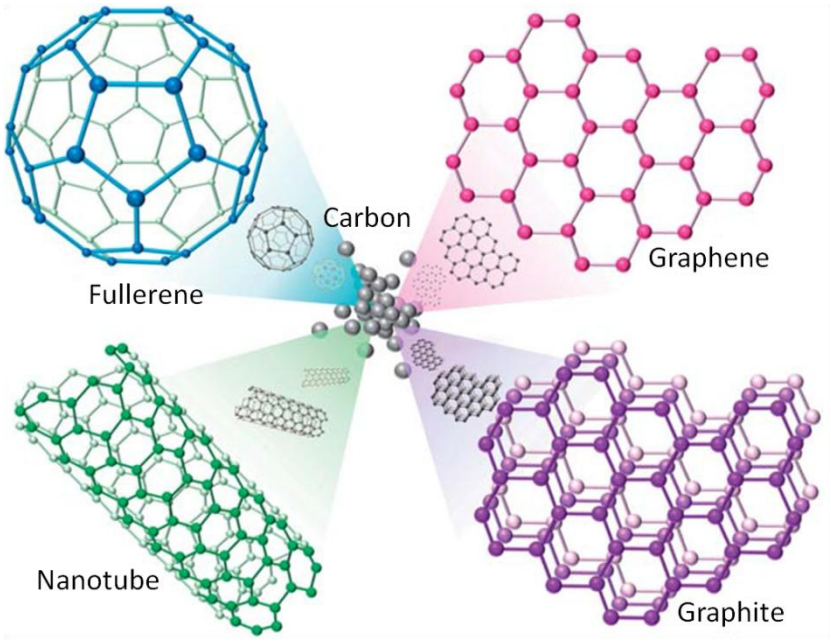

Figure 2.1: Schematic illustration for the carbon allotropes in various structures. Adapted from Cheng *et al*.[98]

2.1.1 Atomic Structure of Graphene

The planar sp^2-bonding configuration dictates that the graphene lattice is of periodic hexagonal honeycomb structure as Figure 2.2 shows. Its unit cell contains two geometrically different carbon atoms each forming the sub-lattices *A* and *B*. The two lattice unit vectors a_1 and a_2 are written as

$$a_1 = \frac{a_{C-C}}{2}\left(3, \sqrt{3}\right),\ a_2 = \frac{a_{C-C}}{2}\left(3, -\sqrt{3}\right)$$

where $a_{C-C} \approx 0.142$ nm is the carbon-carbon bond length. The corresponding reciprocal lattice vectors are

$$b_1 = \frac{2\pi}{3a_{C-C}}\left(1, \sqrt{3}\right),\ b_2 = \frac{2\pi}{3a_{C-C}}\left(1, -\sqrt{3}\right).$$

The Brillouin zone in the *k*-space, constructed from the reciprocal-lattice vectors, is also a hexagon as shown in Figure 2.2. The two vertices of the Brillouin zone *K* and *K'* , named Dirac points, are of particular importance for the physics of graphene:

$$K = \frac{2\pi}{3a_{C-C}}\left(1, \frac{\sqrt{3}}{3}\right),\ K' = \frac{2\pi}{3a_{C-C}}\left(1, -\frac{\sqrt{3}}{3}\right).$$

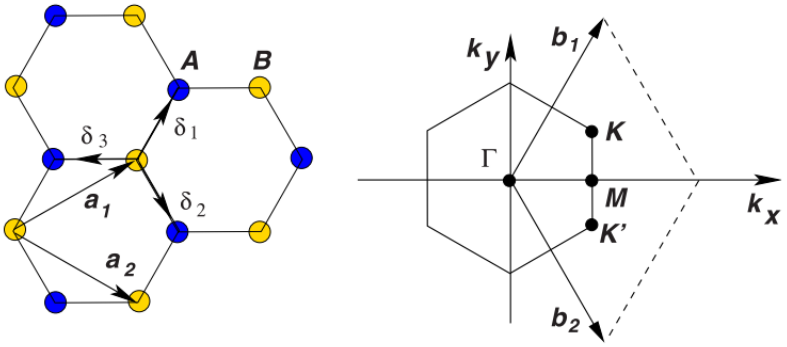

Figure 2.2: Left: Honeycomb lattice structure of graphene consisting of two triangular sub-lattices A and B. a_1 and a_2 are the two lattice unit vectors and δ_1, δ_2, δ_3 are the nearest-neighbour vectors. Right: The Brillouin zone of graphene. Adapted from Neto *et al*.[99]

2.1.2 Electronic Properties of Graphene

Material properties are closely related to their electronic band structures. For graphene the energy bands can be derived by the tight-binding approximation method.[100] The basic idea is to expand the wave function of an electron subject to the periodic crystal potential as a linear combination of the electron's atomic orbit (LCAO) around each of the lattice atoms. Since the graphene lattice consists of two sub-lattices (*A* and *B*), its electron wave function is written as

$$\Psi = c_A \Psi^A + c_B \Psi^B ,$$

where Ψ^A and Ψ^B are the linear combinations of the electron's orbits around the *A* atoms and *B* atoms, respectively.[100] The combination coefficients c_A and c_B are to be determined from the Schrodinger equation $H\Psi = E\Psi$, where *H* is the Hamiltonian and *E* is the eigenvalue. In the tight-binding approximation the overlapping between the nearest-neighbour and next nearest-neighbour atom orbits is regarded more significant than that between the more distant orbits. This leads to the approximate solution for the energy bands:[100]

$$E_{\pm}\left(\vec{k}\right) = \pm\gamma\sqrt{1+4\cos^2\left(\frac{\sqrt{3}k_y a_{C-C}}{2}\right)+4\cos\left(\frac{\sqrt{3}k_y a_{C-C}}{2}\right)\cos\left(\frac{3k_x a_{C-C}}{2}\right)}$$
$$-\gamma'\left(4\cos^2\left(\frac{\sqrt{3}k_y a_{C-C}}{2}\right)+4\cos\left(\frac{\sqrt{3}k_y a_{C-C}}{2}\right)\cos\left(\frac{3k_x a_{C-C}}{2}\right)-2\right),$$

where $\vec{k}$ is the wave vector, + applies to the upper band and – to the lower band. In this dispersion relation $\gamma\left(\approx 2.7 \text{ eV}\right)$ is the nearest-neighbour hopping energy (hopping between different sub-lattices) and γ' is the next nearest-neighbour hopping energy (hopping within the same sub-lattice). Figure 2.3(a) shows the full energy spectrum within the Brillouin zone.[99] If γ' is neglected, the upper and lower energy bands are symmetric around zero energy. Moreover the energy values at the Dirac points (*K* and *K'*) are equal for the upper and the lower band, which indicates a zero energy gap at the six corners of the Brillouin zone. Expanding $E_{\pm}\left(\vec{k}\right)$ around the Dirac points gives an approximately linear dispersion relation:[100]

$$E_{\pm}\left(\vec{q}\right) \approx \pm v\left|\vec{q}\right|$$

where $\vec{q}$ is the wave vector measured relative to the Dirac points and $v = 3\gamma a_{C-C}/2 \approx 1\times10^{6}$ m/s . Since the Dirac points correspond to the largest wave number within the Brillouin zone, v is indeed the Fermi velocity v_F . The linear dispersion relation indicates that the Fermi velocity in graphene is independent of the energy. This is in striking contrast to the conventional parabolic relation $E\left(q\right) = q^2/2m$ which states that the Fermi velocity varies substantially with energy.[99] Indeed the linear dispersion relation resembles that of a photon implying that the electrons and holes close to the Dirac points behave like massless fermions. A zero effective mass should in theory lead to infinite high charge carrier mobility. Yet the real graphene samples have defects, phonons, and finite concentration of charge carriers, which resist the electrical transport of the charge carriers. As a result the measured room temperature mobility is finite, but could still reach the order of 10^4 $cm^2V^{-1}s^{-1}$ when supported by the oxidized Si surface,[101] significantly higher than the typical electron mobility of Si (~1400 $cm^2V^{-1}s^{-1}$). Even higher mobility up to the order of 10^5 $cm^2V^{-1}s^{-1}$ has been obtained from graphene encapsulated in hexagonal boron-nitride.[102]

The zero band gap indicates the charge carriers of graphene can be continuously tuned between electrons and holes by the external gate voltage (Figure 2.3(b)). The inset energy spectrum *E*(*k*) in Figure 2.3(b) shows the Fermi level E_F is shifted away from the Dirac point by the gate voltage with electrons (holes) induced by positive (negative) voltage.[103] Hence graphene offers ambipolar electric field effect for potential electronic applications. There have been demonstrations of the field effect transistors (FET) using

graphene as the channel material.[1,8,104,105] The batch fabrication of graphene FET arrays with uniform electrical properties has shed light on integrating graphene into large scale electronics circuitry.[9] The high frequency graphene FET devices have been obtained using the top gate geometry, reaching a cut-off frequency of tens of up to one hundred GHz.[10,11] The advantages of graphene FETs compared to conventional semiconductor-based FETs lie in its superior charger carrier mobility and the atomic thickness. However the on-off current ratios (I_{on}/I_{off}) of the graphene FETs are relatively low because of the zero band gap, or in another word, the non-zero conductance at zero gate voltage. Current approaches to open the band gap for shutting off the current include epitaxially growing graphene on the SiC substrate,[106] applying electric field perpendicular to the bi-layer graphene,[107] confining the lateral sizes of the graphene channels into quasi-one-dimensional nano-ribbons,[108,109] etc.

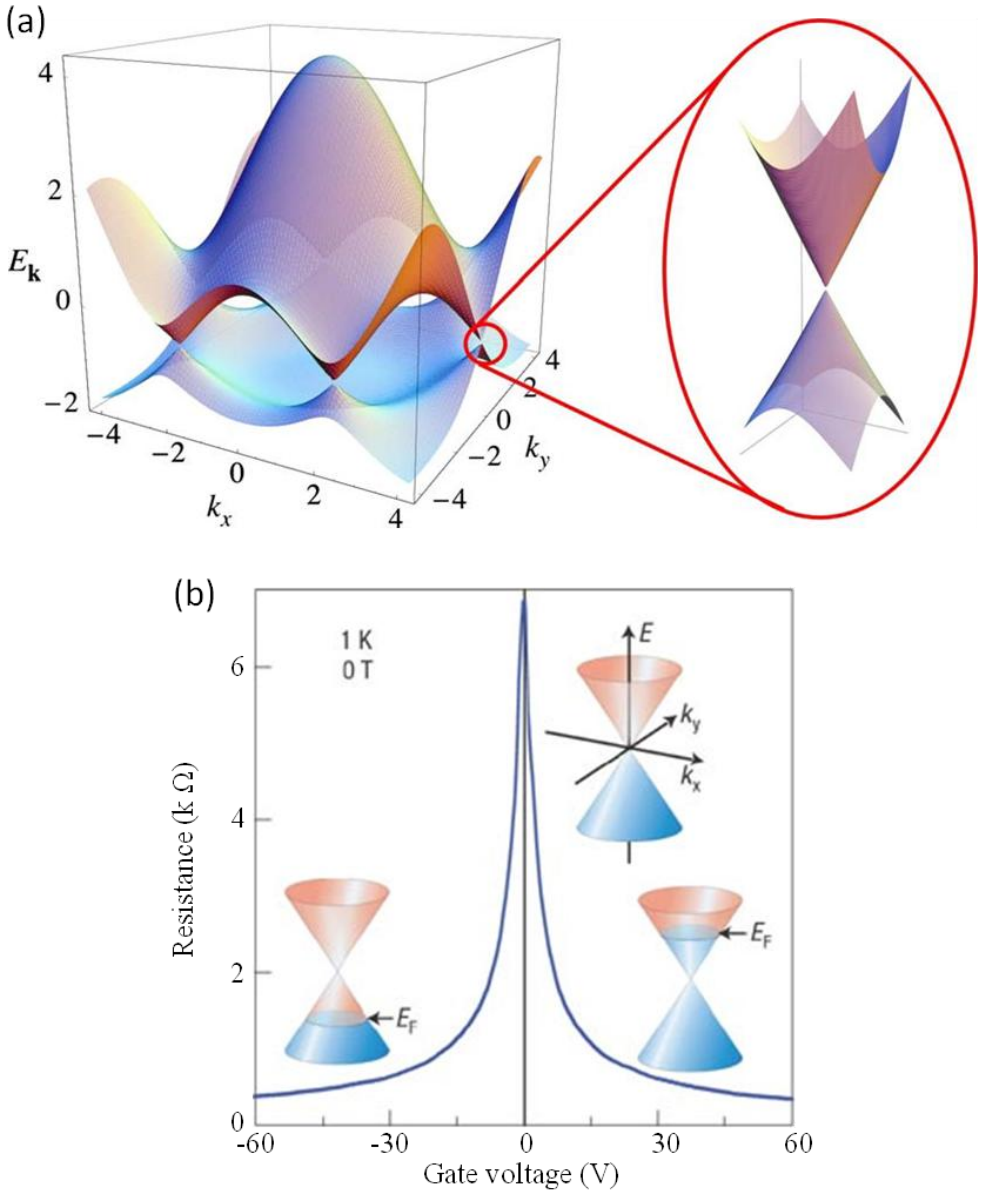

Figure 2.3: (a) Left: Energy bands (in units of γ) of the honeycomb graphene lattice calculated by the tight binding approximation for $\gamma = 2.7$ eV and $\gamma' = -0.2\gamma$. Right: zoom-in of the energy bands around the Dirac points showing the nearly linear dispersion relation. Adapted from Neto *et al.*[99] (b) Dependence of the graphene resistance on the external gate voltage measured at 1K and zero magnetic field. Adapted from Geim and Novoselov.[103]

2.1.3 Optical, Mechanical, and Thermal Properties and Raman Spectroscopy of Graphene

The theoretical values of the optical transmittance and reflectance of monolayer graphene are $(1+\pi\alpha/2)^{-2} \approx 97.7\%$ and $\pi^2\alpha^2(1+\pi\alpha/2)^{-2}/4 \approx 0.01\%$ for normal incident light, respectively, where $\alpha \approx 1/137$ is the fine structure constant.[110,111] The measured transmittance spectrum in Figure 2.4(a) has observed the ~97.7% transmittance for monolayer graphene which is almost constant within the visible

range.[19] An increasing number of the graphene layers decreases the optical transmittance in an almost linear way up to four layers, which is intuitively demonstrated in the inset photo of Figure 2.4(a). The high optical transmittance combined with its electrical conductivity makes graphene promising for use as transparent conductive films.[19–21] Graphene has higher transmittance over a wider wavelength range than other candidate technologies including CNT films,[112–114] metal grids,[115] and metallic nano-wires.[116] Although the electrical conductivity of the intrinsic monolayer graphene is relatively weak (sheet resistance ~6 kΩ),[103] the real samples prepared by the micromechanical cleavage or CVD are generally doped by contact with substrates with the induced charge carrier concentration in the order of 10^{12}-10^{13} cm^{-2}. The sheet resistance of graphene can be further reduced to the order of ~100-200 Ω by rational chemical doping.[117–119] The electrical conductivity of the doped graphene could be comparable to that of other transparent conductive materials.[112,115,120]

The optical transmittance spectrum of graphene reflects the interaction between the electrons in the graphene lattice and the incident photons. The phonons (vibration modes of the carbon atoms) also in-elastically interact with the photons which manifests as the Raman spectroscopy of graphene. Figure 2.4(b) shows that the monolayer graphene has a characteristic Raman *G* peak at ~1580 cm^{-1} and 2*D* peak at ~2700 cm^{-1}.[121] There is also a *D* peak at ~1350 cm^{-1} for defective graphene.[122] The *G* peak is assigned to the in-plane optical vibration mode where each carbon atom vibrates in opposite directions to its three nearest neighbours.[123–125] It is also present in the Raman spectroscopy of other carbon materials containing sp^2 bonding such as CNTs and graphite. The 2*D* peak arises from the inter-valley scattering of the electrons by the Brillouin zone boundary phonons. It is the fingerprint resonance mode of graphene. The electron scattering process associated with the *D* peak involves both a Brillouin zone boundary phonon and a defect state. The corresponding atomic vibration mode can be seen as the breathing motion of a six-member carbon ring, which is restricted by the closely packed neighbouring rings and hence occurs only in the vicinity of the defects.[124] Therefore the *D* peak is absent in defect-free graphene. The origins of these characteristic peaks suggest that the Raman spectroscopy can be used to characterize the crystalline quality of graphene. A weak *D* peak, a high intensity of the 2*D* peak relative to the *G* peak (I_{2D}/I_G), and a small 2*D* peak width are the indicators of high crystalline quality. Meanwhile the Raman spectroscopy can also be used to determine the number of layers up to 5-layer graphene.[123] As shown in Figure 2.4(b), I_{2D}/I_G decreases for an

increasing number of layers and the 2*D* peak itself also broadens, blue-shifts, and becomes asymmetric. The evolution of the 2*D* peak originates from the multiple resonance modes present in the few-layer graphene that could be activated to give rise to the multi components of the 2*D* peak. This is further because the energy bands of the graphene with more than one layer split into several sub-bands due to the inter-layer interaction.[123] The positions of the G and 2*D* peaks are also affected by the level of charge doping through the electron-phonon coupling.[126,127]

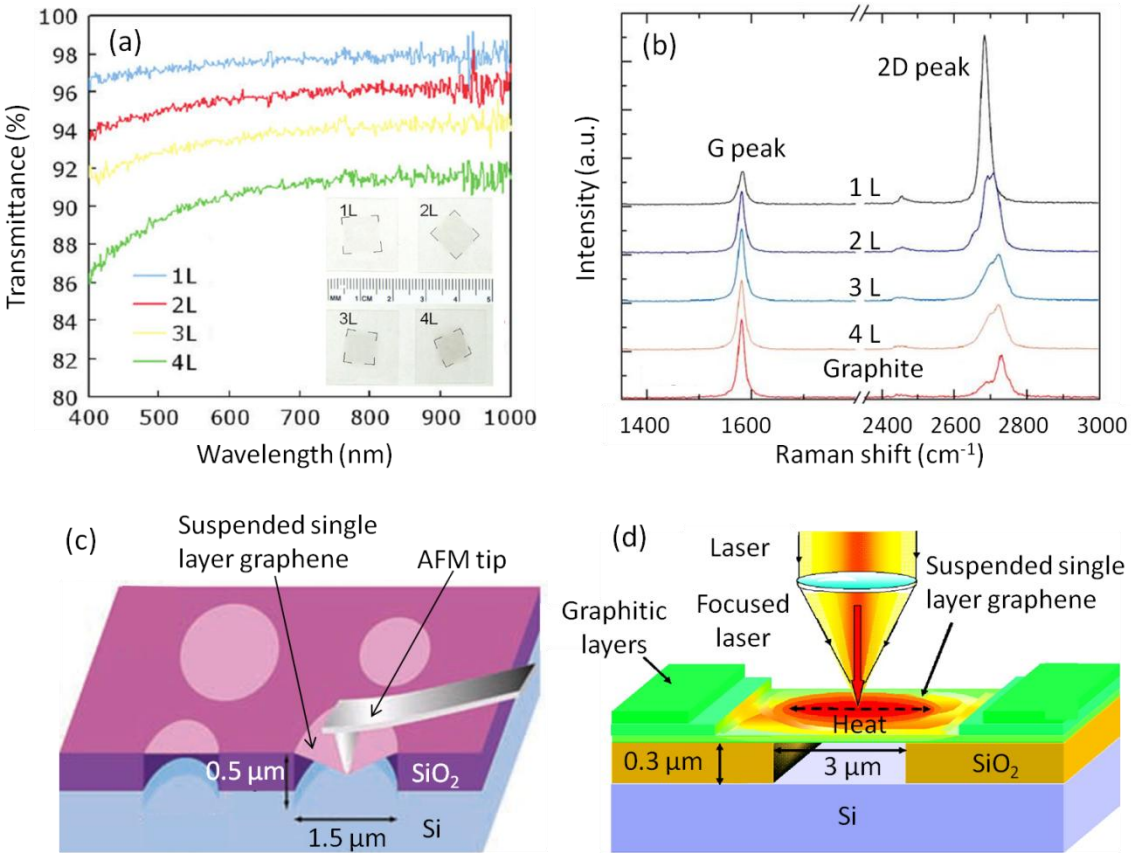

Figure 2.4: (a) Optical transmittance spectrum of graphene with one layer (1L), two layers (2L), three layers (3L), and four layers (4L). Inset shows photograph of the graphene transferred onto quartz. Multi-layer graphene is obtained by repeated transfer and stack. Adapted from Li *et al.*[19] (b) Raman spectroscopy of graphene with 1L, 2L, 3L, and 4L (transferred onto SiO_2/Si) and bulk graphite. Adapted from Cooper *et al.*[121] (c) Schematic for measuring the mechanical properties of the suspended graphene by an AFM tip. Adapted from Lee *et al.*[128] (d) Schematic for measuring the thermal conductivity of the suspended graphene. Adapted from Balandin *et al.*[129]

The mechanical properties of graphene have been studied by both the numerical simulations and the experimental measurements.[128,130–133] One of the typical measurement methods is the nano-indentation set up shown in Figure 2.4(c) where graphene is suspended over a micrometer-sized substrate cavity and an atomic force microscopy (AFM) tip is applied on the trench centre to perform the force-displacement

measurements. The measured Young's modulus of the defect-free monolayer graphene is ~1.0 TPa and the fracture strength is ~130 GPa.[128] These indicate the pristine graphene is a strong material owing to the sp^2 covalent bonding network. In fact it takes 48 000 $kN{\cdot}m{\cdot}kg^{-1}$ of specific strength (force per unit area at failure divided by the mass density) before breaking, much higher than that of steel (~154 $kN{\cdot}m{\cdot}kg^{-1}$).[5] This makes graphene ideal for flexible electronic components.[20,117] Moreover graphene could be added to the lightweight polymers as an enforcer of their mechanical properties.[5]

Graphene is also a good heat conductor. Its thermal conductivity is mainly contributed by the phonon transport while the electronic contribution is negligible due to a low carrier density of the un-doped graphene. The thermal conductivity can be measured using the set up shown in Figure 2.4(d).[129] A laser is focused on the centre of a monolayer graphene flake suspended over a micrometer-sized substrate cavity and the heat radially flows to the graphitic support layers. The temperature rise of the heated graphene induces a red-shift of the Raman *G* peak whose magnitude is linearly dependent on the graphene temperature at low laser power.[134] The thermal conductivity can be extracted as the slope of the measured dependence of the *G* peak shift on the excitation power, which reaches ~5000 $Wm^{-1}K^{-1}$ for defect-free monolayer graphene. Contact with substrates such as SiO_2 is reported to degrade the thermal conductivity to ~600 $Wm^{-1}K^{-1}$, which results from the phonons leaking across the graphene-substrate interface and the interface scattering of flexural modes.[135] Nevertheless the thermal conductivity of graphene is a significantly high value compared to ~385 $Wm^{-1}K^{-1}$of Cu. Thus graphene could have potential use in solving the heat dissipation problems for the nano-electronic architecture.[135]

2.2 Graphene Synthesis Methods

The industrial use of graphene will require inexpensive and large scale synthesis methods that can offer graphene with properties specifically tailored for the target applications. Figure 2.5 summarizes the mainstream synthesis methods. Micromechanical cleavage, also known as micromechanical exfoliation, utilizes sticky tape to peel the multi-layer graphite flakes off the highly-oriented pyrolytic graphite (HOPG). The flakes stuck to the tape surface are then repeatedly peeled off by the fresh sticky tape and hence gradually thinning into few-layer and monolayer graphene flakes. The sticky tape is finally pressed against a target substrate such as SiO_2 leaving the

graphene flakes onto the substrate surface (Figure 2.5(a)). The micromechanically cleaved graphene is of high crystalline quality with charge carrier mobility up to ~10^7 $cm^2V^{-1}s^{-1}$ at 25K for a decoupled monolayer graphene on the surface of bulk graphite,[136] and the room temperature mobility on the SiO_2 surface to ~20000 $cm^2V^{-1}s^{-1}$.[101] However the graphene crystallite size is limited by the single crystal grains in the starting HOPG, generally below the order of millimeters.[2] Therefore the graphene prepared in this manner is generally used for the fundamental research and prototypical device fabrication but impractical for large scale applications.

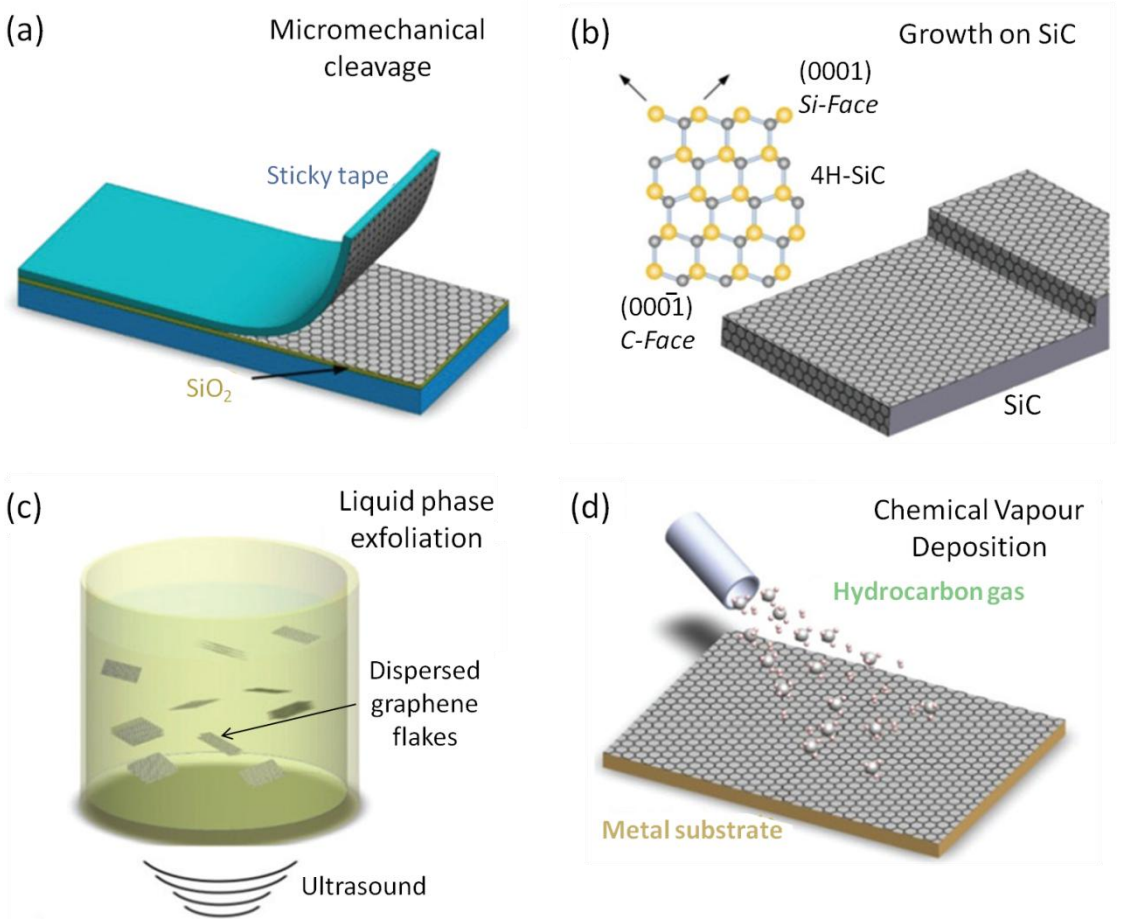

Figure 2.5: Schematic illustration of graphene synthesis methods. (a) Micromechanical cleavage using a sticky tape onto SiO_2. (b) Epitaxial growth of graphene on the surface of the crystalline SiC. Ball-stick model shows the Si-face and C-face of the SiC. (c) Liquid phase exfoliation. Bulk graphite is dispersed into graphene flakes by ultrasonication in solvents. (d) Chemical vapour deposition of graphene from hydrocarbon precursors onto catalytic metal substrates. Adapted from Ferrari *et al.*[5]

Graphene can also form on the crystalline SiC substrate via Si evaporation under high temperature annealing in vacuum (see Figure 2.5(b)).[38,39] The growth on SiC is normally seen as epitaxial although the lattice mismatch between graphene (2.46 Å) and SiC (3.073 Å) is as large as ~25%. Both of the C-terminated ($000\bar{1}$) and Si-terminated

(0001) surfaces can be used as the starting templates.[137,138] But the lateral size of the graphene domains formed on the C-face can reach ~200 nm,[139,140] larger than those on the Si-face (~30-100 nm).[139] The charge carrier mobility of graphene grown on the C-face has been reported up to ~10 000-30000 $cm^2V^{-1}s^{-1}$ in contrast to ~500-2000 $cm^2V^{-1}s^{-1}$ on the Si-face.[140,141] The benefit of the SiC-derived growth is that it is compatible with the established SiC-technology in power electronics. For instance, high frequency transistors have been fabricated from graphene grown on SiC with 100 GHz cut-off frequency which is higher than the Si transistors of the same gate length.[11] Top gated transistors have also been demonstrated.[142] However the SiC-derived graphene generally contains mixture of multi-layer graphene and hence prevents its potential use in applications where control of the layer thickness uniformity is necessary.[38] Another disadvantage of the SiC technology is that the SiC wafers are expensive. The substrate costs need to be reduced while still maintaining the graphene quality if the SiC technology is to be used for large scale production.

Liquid phase exfoliation (LPE) is another approach for large scale production of graphene. A typical LPE process generally undergoes three steps (see Figure 2.5(c)): (1) chemical wet dispersion of the bulk graphitic materials in a solvent; (2) ultrasonication-induced exfoliation of the bulk into thin layer graphene flakes; (3) purification of the graphene flakes through ultracentrifugation.[40–48] Liquids with surface tension ~40 $mN \cdot m^{-1}$ are found to be the ideal solvents for dispersing graphene flakes because they can effectively minimize the liquid-graphene interfacial tension.[44,143] These include N-methyl pyrrolidone (NMP), dimethyl formamide (DMF), benzyl benzoate, γ-butyrolactone (GBL), acetone, chloroform and isopropanol, etc.[44,144] The exfoliated graphene flakes can be separated from the un-exfoliated graphitic materials by ultracentrifugation in a uniform or density gradient medium.[145] The uniform medium-based method can produce graphene flakes with lateral size ranging from a few nanometres to a few micrometres with mass concentration in the order of $mg \cdot ml^{-1}$.[47,146] The number percentage of the monolayer flakes among the total graphitic flakes can reach ~70% by uniform medium separation after sonication in the suitable solvents.[40] The density gradient medium-enabled ultracentrifugation can sort graphene flakes with different thickness with the aid of the suitable surfactants.[145,147] This can produce monolayer flakes with the number percentage up to ~80%.[148] In general the LPE graphene flakes are of micrometer-scale lateral size due to the fracture-induced exfoliation procedure.[40–42,44,47,48,144] Their charge carrier mobility are in the order of tens

of $cm^2V^{-1}s^{-1}$, significantly inferior to the micromechanically cleaved and the SiC-grown graphene.[48] However the LPE technology is scalable and cost-saving. These make the LPE graphene competitive candidates for applications in composite materials,[41] conductive inks,[48] ink-jet printed thin film transistors,[48] etc.

CVD of graphene is the process of producing the graphene film onto the desired substrates by chemically reacting a volatile hydrocarbon compound, such as CH_4 or C_2H_2, with other gases (mostly H_2) (see Figure 2.5(d)). The reaction normally occurs in a sealed chamber offering the required pressure and high temperature. Certain metal substrates suitably placed inside the reactor, such as Cu, Ni, Co, etc, are used as catalysts to assist the graphene formation.[49–53] The desired graphene films are deposited on the catalytic substrates while the gaseous by-products along with the un-reacted precursors are exhausted out of the reactor. Figure 2.6(a) demonstrates the isolated monolayer graphene flakes synthesized on the Cu surfaces.[59] The individual domains are in hexagonal shapes indicating their single crystalline nature.[54] Continuous graphene films with mostly monolayer have been achieved using Cu as catalysts.[53] Figure 2.6 (b) shows such an example which has been transferred onto the SiO_2 substrate from the original Cu catalyst.[57] The Cu-catalyzed CVD technologies can now enable the growth of high quality graphene with single crystalline domains up to inch size, much larger than that obtained by other production methods.[62,73] The room temperature mobility have reached the order of 10^4 $cm^2V^{-1}s^{-1}$,[62,78,149] only below that of the micromechanically cleaved graphene flakes. Yet the CVD approach is particularly advantageous compared to the micromechanical cleavage in that it is easily scalable and hence allows large scale production. For instance, 30-inch graphene films have been grown on the Cu foils cylindrically wrapped inside a thermal furnace (Figure 2.6(c)).[117] They can function as conductive, transparent and flexible electrodes when they are transferred onto the suitable substrates such as the polyethylene terephthalate (PET) (Figure 2.6(d)). Kobayashi *et al*[21] has demonstrated the growth of 100 m graphene films using Cu foils that are rolled in the cassette configuration and enclosed in vacuum chambers. Yet this is not a truly roll-to-roll (R2R) production manner. Recently Zhong *et al*[55] has managed to synthesize monolayer graphene films on Cu foils using an open-ends CVD system. The Cu foils are dynamically loaded from air through an open slit on one end of the furnace into the reaction zone for graphene deposition. The graphene-covered Cu foils are simultaneously unloaded through another open slit on the other end. Such a truly R2R technology can be directly integrated into the production lines

with sequential processes before and after growth. Since the R2R reactor is directly open to air, particular attention should be paid in the R2R CVD growth to the safety issue associated with using the flammable gases at high temperature. At least the concentration of the flammable gases needs to be controlled strictly below the LEL.

Besides from those mentioned here, there are a couple of other graphene production methods such as anodic bonding between graphite and glass substrate,[150,151] photo-exfoliation via laser-induced detachment of an entire graphitic layer,[152,153] molecular beam epitaxy growth on insulating substrates,[154,155] and thermal-driven conversion of the deposited solid carbon sources into graphene,[156–160] etc. Among these methods, the CVD technology, particularly the Cu-catalyzed CVD route, has extraordinary potential for large scale production owing to the achieved balance between the film quality and the process scalability.

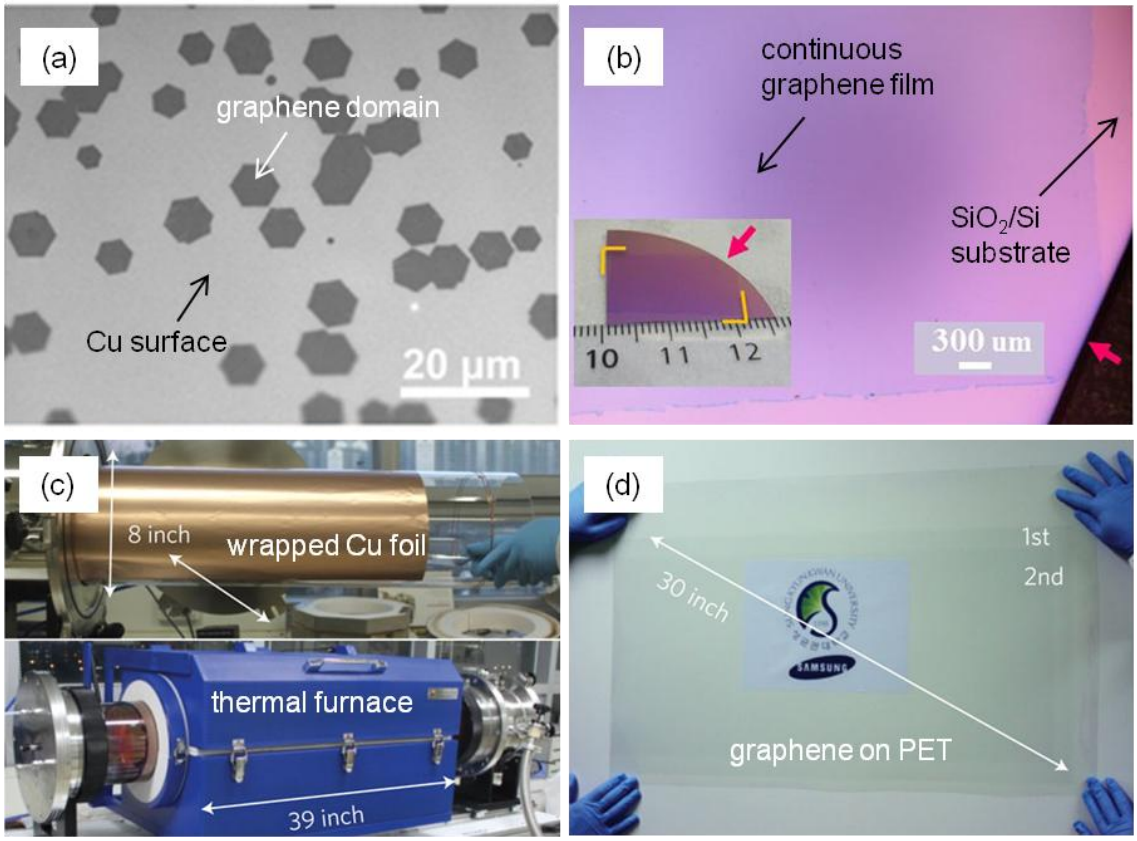

Figure 2.6: Typical CVD-derived graphene. (a) SEM image of isolated, monolayer, hexagonal graphene flakes grown on Cu. Adapted from Zhou *et al.*[59] (b) OM image of the continuous monolayer graphene film transferred onto the SiO_2-coated Si wafer. Adapted from Deokar *et al.*[57] (c) Photograph of the 8-inch wide Cu foils wrapped inside a 39-inch thermal furnace for CVD growth. Adapted from Bae *et al.*[117] (d) 30-inch continuous graphene films transferred from Cu onto the PET substrate. The bi-layer graphene is obtained by repeated transfer. Adapted from Bae *et al.*[117]

2.3 Synthesis of Graphene by Metal-catalyzed Chemical Vapour Deposition

2.3.1 Metal-catalyzed Chemical Vapour Deposition Processes and Reactions

Figure 2.7 sketches the procedures of a typical meta-catalyzed graphene CVD process which includes:[161]

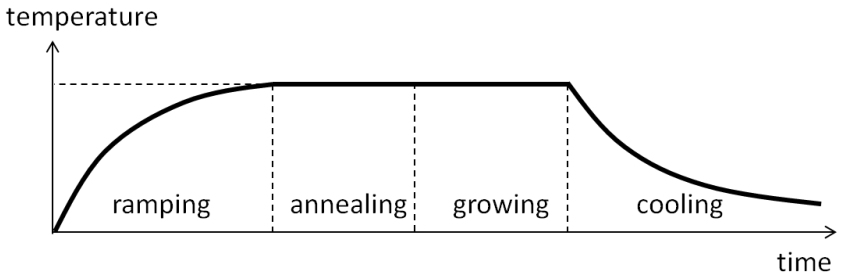

Figure 2.7: Schematic illustration of the general graphene CVD process.

- Ramping: the metallic substrate is heated inside the reactor up to the annealing temperature.[53]
- Annealing: the substrate is annealed at the stablized temperature by the reductive gas such as H_2. An optimal annealing condition (temperature, gas composition, time, etc) can effectively reduce the metal oxides, remove the surface contaminants and promote the metal re-crystallization towards larger metal grain size and lower surface roughness.[78]
- Growing: a gaseous hydrocarbon precursor, mostly CH_4, is introduced into the reactor to initiate the graphene growth on the substrate surface. The H_2 supply is maintained during the growth step. To improve the quality of the synthesized graphene, the CVD parameters affecting the graphene growth need to be optimised including the growth temperature, the partial pressure of both the hydrocarbon and H_2, etc.[162,163]
- Cooling: after a desired growth time, the hydrocarbon supply is terminated and the system is cooled down in a proper gas environment before the graphene/substrate sample is unloaded from the reactor.

For the graphene formation from the most commonly used CH_4/H_2 mixtures, the above-described growth step contains the detailed sequential reactions illustrated in Figure 2.8:[62,95,161,164,165]

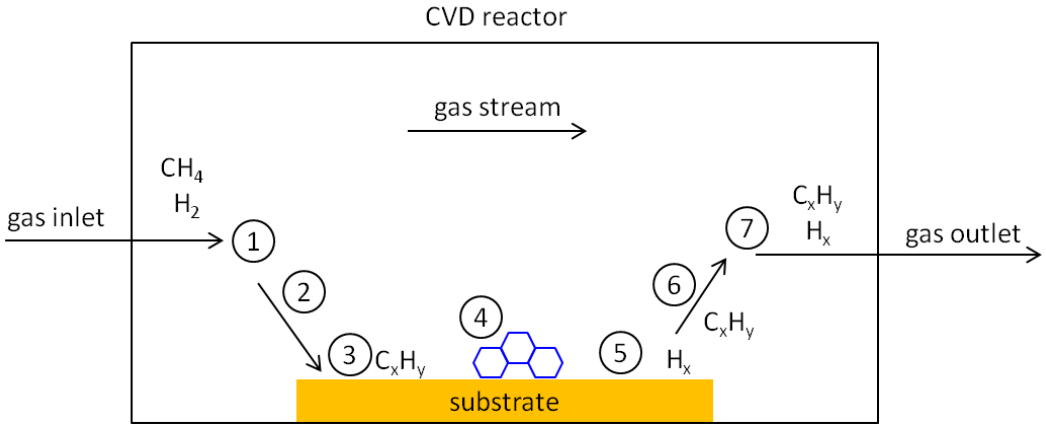

Figure 2.8: Schematic illustration of the graphene growth stage using CH_4 and H_2 as gas reactants.

- Step 1: transport of the gaseous reactants by the forced convection into the reactor.
- Step 2: gas-phase diffusion of the reactants from the main gas stream through the boundary layer to the substrate surface.
- Step 3: dissociative chemisorption of the reactants on the substrate surface sites.
- Step 4: thermally activated surface processes, sequentially including the catalytic dehydrogenation, graphene nucleation on the favourable surface sites, diffusion of the hyodrcarbon species to the edges of an existing domain, lateral growth of the graphene domain via attachment of the carbon species onto the edges, and other heterogeneous surface processes. Bulk diffusion of the carbon species might also occur depending on the carbon solubility of the metal substrates.
- Step 5: desorption of the by-products (C_xH_y, H_x, etc) from the substrate surface.
- Step 6: transport of the by-products by diffusion through the boundary layer and back to the main gas stream.
- Step 7: expelling of the by-products by forced convection away from the deposition region.

2.3.2 Transition Metal Catalysts

Conventionally used hydrocarbon feedstock for CVD of graphene includes CH_4, C_2H_2 and C_2H_4, etc. CH_4 , the most commonly used, has dehydrogenation energy of 440 kJ/mol. Direct decomposition of the C-H bonds in gas phase, i.e., pyrolysis, requires

high temperature (>1200 ℃) which is not easily obtained in typical thermal CVD systems.[166] Transition metals are thereby used as catalysts to reduce the energy barriers for the hydrocarbon decomposition. Their catalytic ability originates from their unfilled *d*-orbitals in the outer shells which enable bonding with the electrons of the carbon atoms. For graphene formation using the hydrocarbon precursors, the catalytically active metals include Ru,[167] Ir,[49] Pt,[168] Co,[169] Pd,[170] Re,[171] Fe,[172] Ni,[173], Cu.[53] Among them Ni and Cu are the most widely used and most intensively studied because they can catalyze the growth of graphene with relative uniform film thickness and high crystalline quality.

2.3.3 Catalyst-dependent Growth Kinetics

Since the transition metal catalysts reduce the dehydrogenation energy barriers, the heterogeneous reactions (in the metal bulk or on the metal surfaces) instead of the homogenous reactions (in the gas phase) dominate the graphene formation process. Therefore the growth kinetics depends on the properties of the catalysts. For instance, the carbon solubility of Ni is ~0.6 weight % at 1326℃, much higher than that of Cu (0.001-0.008 weight % at 1084 ℃).[174] As a result a significant amount of the carbon atoms diffuse into the bulk Ni at high temperature (see Figure 2.9).[161] The carbon isotope labelling technique in conjunction with Raman spectroscopic mapping have demonstrated that the dissolved carbon atoms segregate from the bulk Ni during the cooling step to the surface where they migrate to form the graphene layers on the surface.[173,174] The cooling rate has crucial influences over the formed graphene.[20,51] In the case of Cu-catalyzed growth, only a negligible amount of carbon atoms can be dissolved in the bulk Cu. The carbon species contributing to the graphene growth are mostly supplied by the CH_4 that catalytically decomposes on the Cu surfaces.[174] The surface processes including the diffusion and edge attachment of the carbon species dominate the growth kinetics. The low energy electron microscope (LEEM) study also observes little carbon segregation during the cooling step,[175] further confirming the Cu-catalyzed graphene formation is mostly a surface-mediated process.

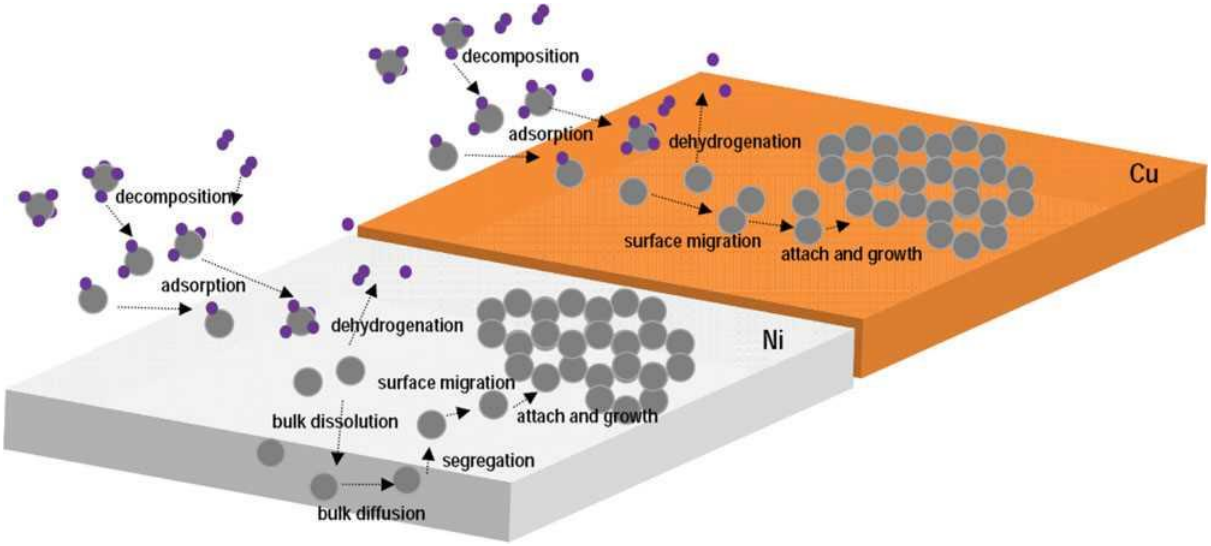

Figure 2.9: Schematic illustration for the catalyst-dependent graphene growth kinetics in the cases of Ni and Cu. Adapted from Muñoz and Aleixandre.[161]

Since the catalytic dehydrogenation of the hydrocarbon precursors only occurs on the surfaces of the transition metals, the surfaces are no longer catalytically active once covered by the formed graphene due to catalyst poisoning. The overall catalytic ability thereby decreases as the areal coverage of graphene increases. The termination of the growth should be no later than the complete coverage. It is also difficult for the ad-layer graphene to grow on top of the first layer.[53] In this sense the transition metal-catalyzed graphene formation is in principle a self-limiting process if the surface reactions dominate the graphene formation. Cu is generally such a instance as the Cu-catalyzed graphene growth is typically surface-mediated. This enables the growth of uniform monolayer graphene on Cu with the areal proportion of the multi-layer patches generally below ~5% as shown in Figure 2.10 (c) and (d).[176] The monolayer uniformity is essential for the performance homogeneity of large area graphene-based applications. The multi-layer proportion can be further reduced to a negligible level by modified Cu-CVD techniques such as CH_4-annealing-induced Cu surface faceting which promotes formation of monolayer graphene.[58] In contrast, the Ni-based CVD processes have poorer control of the monolayer uniformity. Figure 2.10(a) and (b) show that the graphene grown on Ni is typically a mixture of monolayer and multi-layer patches.[176] In this sense Cu is a advantageous catalyst compared to Ni and other transition metals with relatively high carbon solubility. Indeed Cu has nowadays become the most commonly used catalyst for synthesis of monolayer, high quality, continuous and large area graphene for laboratory-level research purposes.[5,177] It is worth of mention, however,

that the self-limiting nature of the Cu-CVD of graphene is conditional to the kinetic factors. For instance, Bhaviripudi *et al*[178] has observed the formation of the multi-layer graphene flakes under a comparatively high total pressure (1 atm) and high CH_4 concentration. The potential reason could be that the rate-limiting step becomes the gas phase mass transport through the boundary layer for the atmospheric pressure CVD (APCVD) contrasting to the surface reactions for the low pressure CVD (LPCVD). Nevertheless the coming discussions on the CVD graphene mechanism will mainly focus on the Cu-CH_4 route.

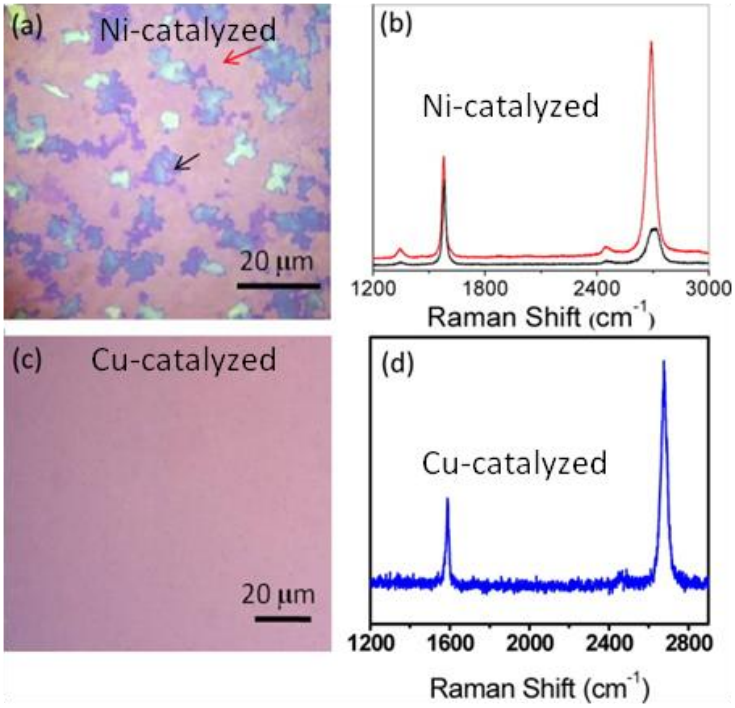

Figure 2.10: Comparison between the Ni- and Cu-catalyzed CVD kinetics. (a) and (c): OM images of the graphene transferred from Ni and Cu onto the SiO_2-coated Si substrates. Red and black arrows mark the monolayer and multi-layer portions. (b) and (d): Raman spectra of the transferred graphene shown in (a) and (c), respectively. The red and black lines in (b) correspond to the monolayer and multi-layer portions marked in (a). Adapted from Zhang *et al*.[176]

2.3.4 Cu-catalyzed Dehydrogenation Energetics

Graphene formation on transition metal surfaces starts from the catalytic dehydrogenation of the absorbed hydrocarbon molecules. The surface metal atoms partially bond with the hydrocarbons in an energetically stable configuration so that the hydrocarbons can lose the hydrogen atoms step by step. Figure 2.11 shows an instance of the dehydrogenating CH_x (x=4, 3, 2, 1) on the Cu (111) surface.[91] The metal-carbon adsorption energy offers the thermodynamic drive for the dehydrogenation. Obviously the dehydrogenation barriers depend on the natures of the underlying metals. For

instance the decomposition of CH_4 is exothermic on active metal surfaces such as Pd and Ru.[179,180] Yet on the Cu surface all of the dehydrogenation steps are endothermic as shown in Figure 2.11.[91] The completely dehydrogenated product is significantly higher in energy than the adsorbed CH_4 molecule. This indicates the atomic carbon cannot stably exist on the Cu surface in its pristine form. Indeed the density functional theory (DFT) investigations suggest the carbon dimers are stable on all Cu surface sites.[89] Therefore the CH_x species tend to combine with each other before losing all the hydrogen atoms. Some researchers have also revealed an energetic preference for the H-terminated graphene edge on Cu compared to the Cu-passivated graphene edge.[62] These evidence suggest that the major building blocks for graphene nucleation and growth on Cu should be the partially dehydrogenated carbon species such as CH instead of the atomic carbon. Furthermore the edges of the formed graphene flakes should keep dehydrogenating so as to leave spaces for the subsequent attachment of the unbound carbon species.[181] The DFT calculations further suggest that the dehydrogenation of the graphene edge limits the rate of the edge attachment step.[62]

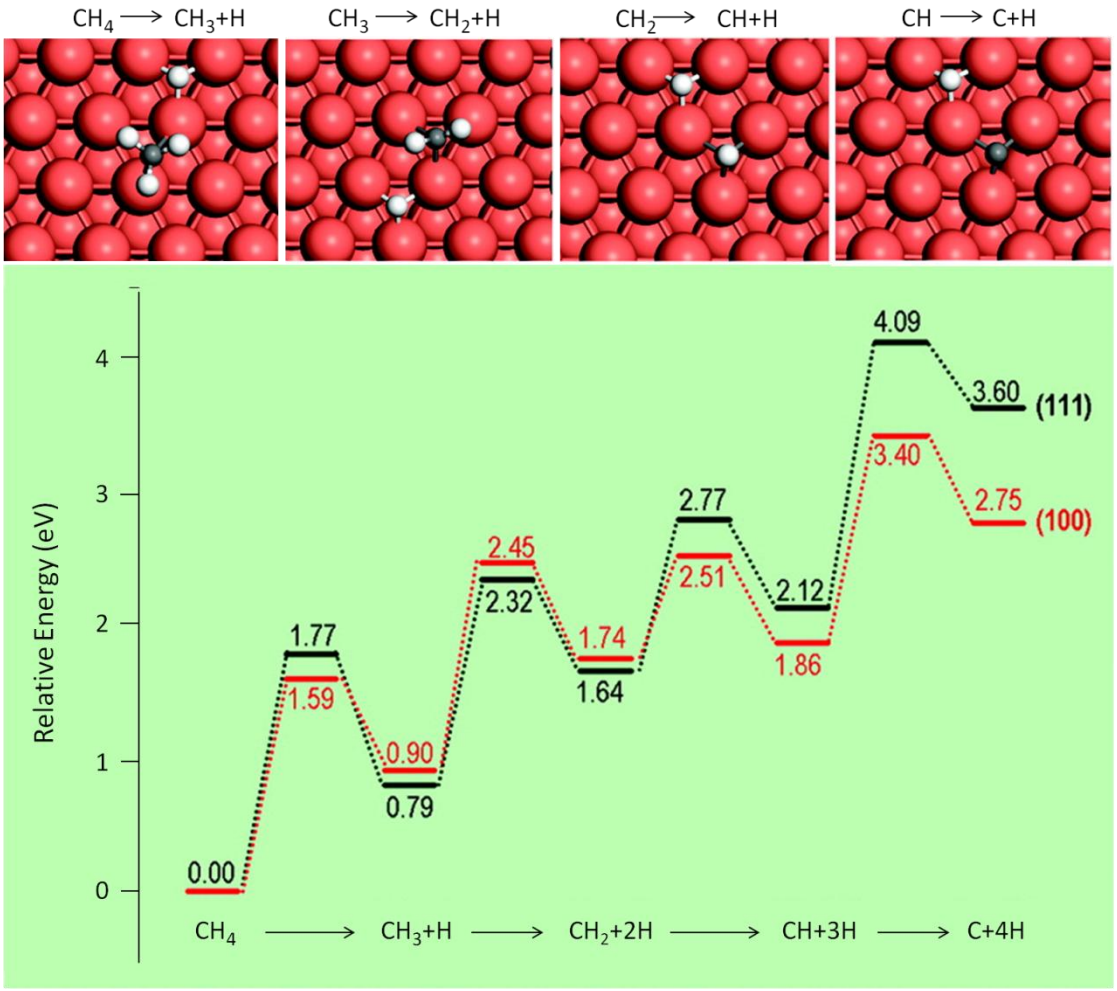

Figure 2.11: DFT investigations of the Cu-catalyzed CH_4 dehydrogenation. Top: Optimized geometric configurations of a dehydrogenating CH_x (x=4, 3, 2, 1) on the Cu (111) surface. Red, black and white balls represent the Cu, C and H atom, respectively. Bottom: DFT-computed energy profiles of the CH_4 dehydrogenation on Cu (111) (black) and Cu (100) (red) surfaces. Adapted from Zhang *et al*.[91]

2.3.5 Graphene Nucleation on Catalyst Surfaces

The nucleation of graphene is the transformation process from the isolated hydrocarbon species to the sp^2-bonded carbon networks with the aid of the catalyst surface. It can be seen as the starting point of graphene growth. The classical crystallization theory offers a thermodynamic understanding of the nucleation process: when the rates of CH_4 adsorption onto and desorption from the catalyst surface are balanced, the concentration of the surface hydrocarbon species reaches its peak value, which is normally named chemical supersaturation. Driven towards an energetically more favourable state, the supersaturated hydrocarbons undergo a transition from the amorphous to the crystalline phase and in this manner a graphene nucleus is formed.[182,183]

In recent years numerical simulation studies have revealed abundant kinetic features of the nucleation process enabling a more delicate understanding. Gao *et al*[90] has found the heterogeneous graphene nucleation near a catalyst surface step edge has a lower energy barrier than on a terrace (~2.0 eV on Ni (111) surface) due to stronger metal-carbon bonding The step-edge-aided nucleation should therefore dominate the overall nucleation events. The similar preference is expected to exist on other transition metal catalysts. For instance, the Cu-CVD experiments of Han *et al*[184] have shown that the nucleation density is larger near the artificial scratches that are intentionally created on the Cu surface compared to on the relative smooth surface regions. These findings suggest that the catalyst surface morphology plays a critical role in providing active sites for graphene nucleation. The catalyst surface roughness should be rationally reduced in a practical CVD recipe targeting at graphene with lower nucleation density and larger domain size.

The graphene nucleates once the hydrocarbon has accumulated on the active sites up to the supersaturation level. Yet the nucleation does not occur by hydrocarbons naively combining into a six-carbon ring structure. Instead the theoretical calculations of Gao *et al* have suggested a counterintuitive nucleation pathway.[90] The small C_N clusters ($N<12$) on the Ni(111) surface tend to stay in the form of the linear chains instead of the closed rings. This is because both end atoms of the carbon chains are tightly bound to the surface hollow sites which helps stabilize the entire structure. For the Cu (111) surface, Wesep *et al*[92] has found a similar energy advantage of the carbon chain structure over the ring structure as shown in Figure 2.12. The inset of Figure 2.12 schematically demonstrates the relaxed configurations of the chain and ring structures with six atoms. Since the formation energy of the carbon chain structure increases with its length, the sp^2-bonded ring structure eventually becomes the ground state configuration for $N \geq 12$. This can be seen as the formation of a well-defined graphene nucleus. However, the infant nucleus does not appear to contain hexagon-only carbon rings. Some research suggests the most stable configurations always contain a few pentagons owing to the reduced formation energy of the edge carbon atoms.[90,185]

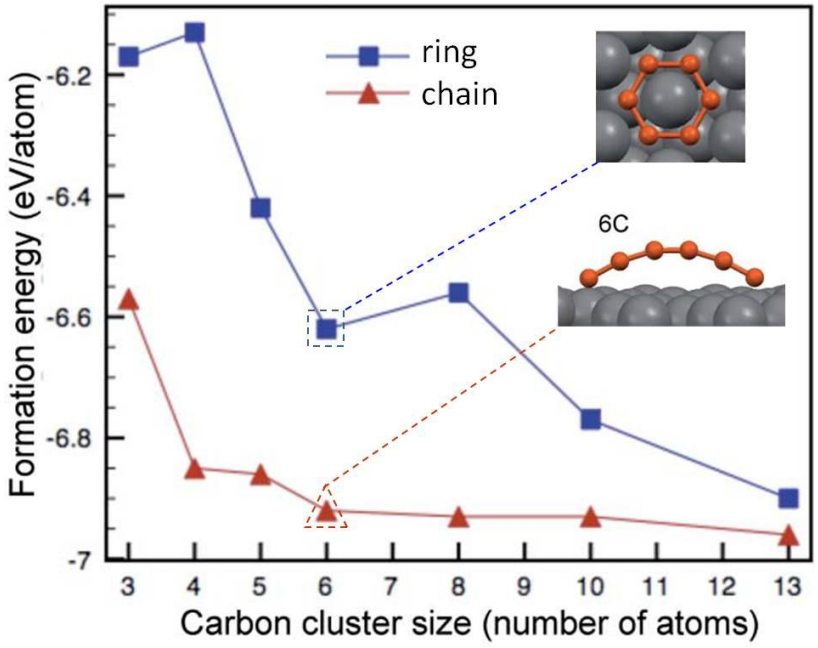

Figure 2.12: The formation energies per carbon atom of the carbon chains and rings with 3~13 atoms on the Cu (111) surface. Inset are the relaxed configurations for C_6 in the ring (top) and chain (bottom) geometry. Gray and orange balls represent the Cu and C atoms, respectively. Adapted from Wesep *et al*.[92]

2.3.6 Graphene Domain Growth via Hydrocarbon Attachment

Following the nucleation is the lateral growth of the graphene domain by incorporating onto its front edge the hydrocarbon species that have migrated from the far field catalyst surface. For the Cu-catalyzed CVD the hydrocarbon species to be attached should be the partially dehydrogenated products such as CH since the atomic carbon is energetically unfavourable on the Cu surface.[62] The attachment rate is generally anisotropic along the domain circumference. This is because the domain edges contain chemically different sites for attachment. Figure 2.13(a) illustrates two fundamental types of edge sites, the zigzag sites along $\varphi = 0^{o}$ (slanted angle) and the armchair sites along $\varphi = 30^{o}$, as well as an arbitrarily-oriented edge, which can be seen as a geometric mixture of the zigzag and armchair sites. The DFT calculations show that the hydrocarbon attachment to the armchair edges on Cu (111) surface is energetically more favourable than to the zigzag and any other arbitrary edges.[93,94] This is attributed to the armchair sites being suitably passivated by the Cu atoms which lowers the barrier for attaching new hydrocarbons from ~2.5 to ~0.8 eV. The preferential occupation of the armchair sites in the row-by-row manner gradually converts all the armchair-containing edges to the zigzag-only edges.[93] The schematic in Figure 2.13(b) demonstrates the transformation of a armchair

segment into the zigzag edges after sequential incorporation of three rows of carbon atoms. The original domain corners of 90° and 150° are consequently turned to 120°. The formed zigzag edges then laterally propagate outward enabling the continuous domain growth without altering the zigzag geometry. It can be readily inferred that the graphene domains with eventually all-zigzag edges are necessarily hexagonal as all the corners should be 120°. This dynamic scenario explains the widely observed hexagonal graphene domains on the Cu surface under suitable CVD conditions,[65,79,93,186,187] also shown in Figure 2.6(a). The spatial Raman spectroscopic mapping as well as the atomic-resolution Scanning Tunnelling Microscope (STM) study of the hexagonal domains confirm the domain edges are in the zigzag geometry.[93,188]

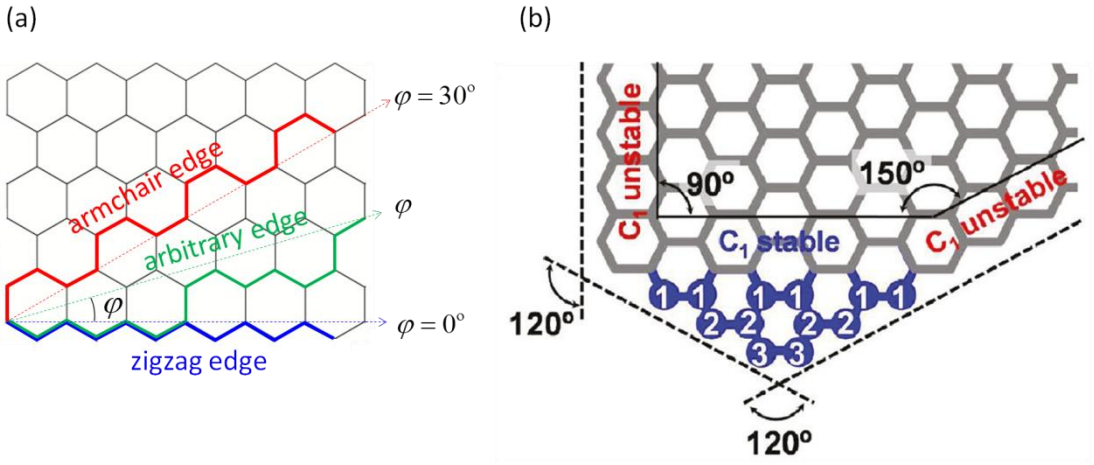

Figure 2.13: (a) Schematic illustration for the zigzag (blue), armchair (red) and arbitrary(green) edges. (b) Schematic illustration of the edge-converting mechanism. Gray lines represent the existing graphene domain. The blue balls labelled 1 are the stable edge sites where the hydrocarbon can attach. After the sites 1(2) are occupied by the newly attached carbon, the sites 2(3) are rendered for follow-up attachment. Each new atomic row completes one fewer hexagon then the previous one until the entire armchair edge disappears. Adapted from Luo *et al.*[93]

The anisotropy of the graphene domain growth rate can be alternatively understood as a consequence of the graphene edge stability being dependent on the aforementioned slanted angle φ. Since any arbitrary edge consists of the mixed armchair and zigzag sites, the formation energy of the arbitrary edge, $E(\varphi)$, can be analytically expressed as a linear combination of that of the armchair and zigzag edges (E_{AC} and E_{ZZ}):[189]

$$E(\varphi) = 2E_{AC}\sin(\varphi) + 2E_{ZZ}\sin(30^\circ - \varphi).$$

The Yakobson's group[95] has evaluated E_{AC} and E_{ZZ} by the first principle atomistic calculations taking into account the influences of the underlying metal surfaces. For the equilibrium state or slow growth, the classic Wulff construction based on the angle-dependent energy plot can yield the thermodynamically optimal domain shape. Figure 2.14 demonstrates that the as-constructed domain shapes are hexagonal on the catalytic Fe (111), Co (111), Ni (111) and Cu (111) surfaces.[69] The edges of the hexagonal domains are all in the zigzag configuration (represented by the blue lines in Figure 2.14) owing to $E_{ZZ} < E_{AC}$ on all the four metal surfaces.[69]

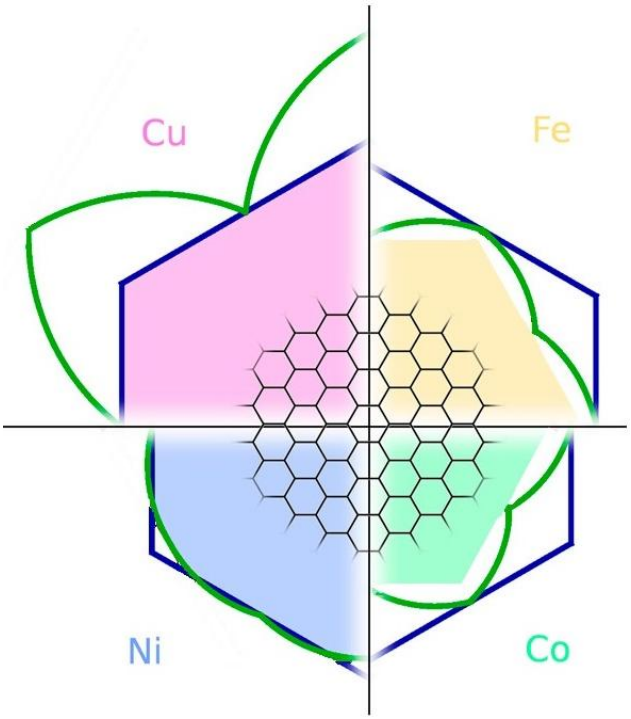

Figure 2.14: Wulff constructions for graphene domains on Fe, Co, Ni, and Cu surfaces. Only one quadrant is shown for each metal and the full shapes can be recovered by the reflection symmetry. The green lines are the polar plots of the edge energy $E(\varphi)$ on each metal. The blue lines represent the inner envelopes of all the perpendiculars to the radius vectors from the origin to the polar plots, i.e., the equilibrium domain shapes. Adapted from Artyukhov *et al*.[69]

It is worth of mention that the graphene domain shapes are not always equilateral hexagonal. As shown in Figure 2.15, the Cu-CVD experiments have observed the formation of triangular (Figure 2.15(a)),[190,191] rectangular (Figure 2.15(b)),[192–194] four-lobed,[53,175,195,196] five-lobed (Figure 2.15(c)),[191] six-lobed,[63,196] irregular hexagonal,[187,197] twelve-pointed graphene domains,[64] etc. Besides from the polygonal shapes with straight edges, the dendritic graphene domains with serrated edges are also reported (Figure 2.15(d)).[62,68,198,199] The formation of the dendritic shapes is generally attributed

to the surface-diffusion-controlled growth mechanism, i.e., the rate of the hydrocarbon diffusion on the Cu surface is significantly lower than the rate of the edge attachment.[66,67] Those shape variants with non-six-fold symmetry could originate from the complicated kinetic factors of the heterogeneous graphene formation process such as the graphene-Cu epitaxy. For instance, the triangular and five-lobed domains are observed on the exotically textured Cu surfaces with specific Cu grain shapes.[190,191] Murdock *et al*[197] has observed from polycrystalline-Cu-foil-catalyzed LPCVD experiments and corroborated with the DFT calculations the existence of the graphene domains with: (1) four-fold symmetry on the Cu (101) facets with edges orientated along Cu [-101], (2) four-fold symmetry on the Cu (001) facets with edges orientated along both Cu [110] and Cu [-110], (3) six-fold symmetry on Cu (111)-close facets with edges oriented along Cu [-110]. These suggest the underlying Cu surface morphology largely controls the graphene domain shapes in a quasi-epitaxial manner.

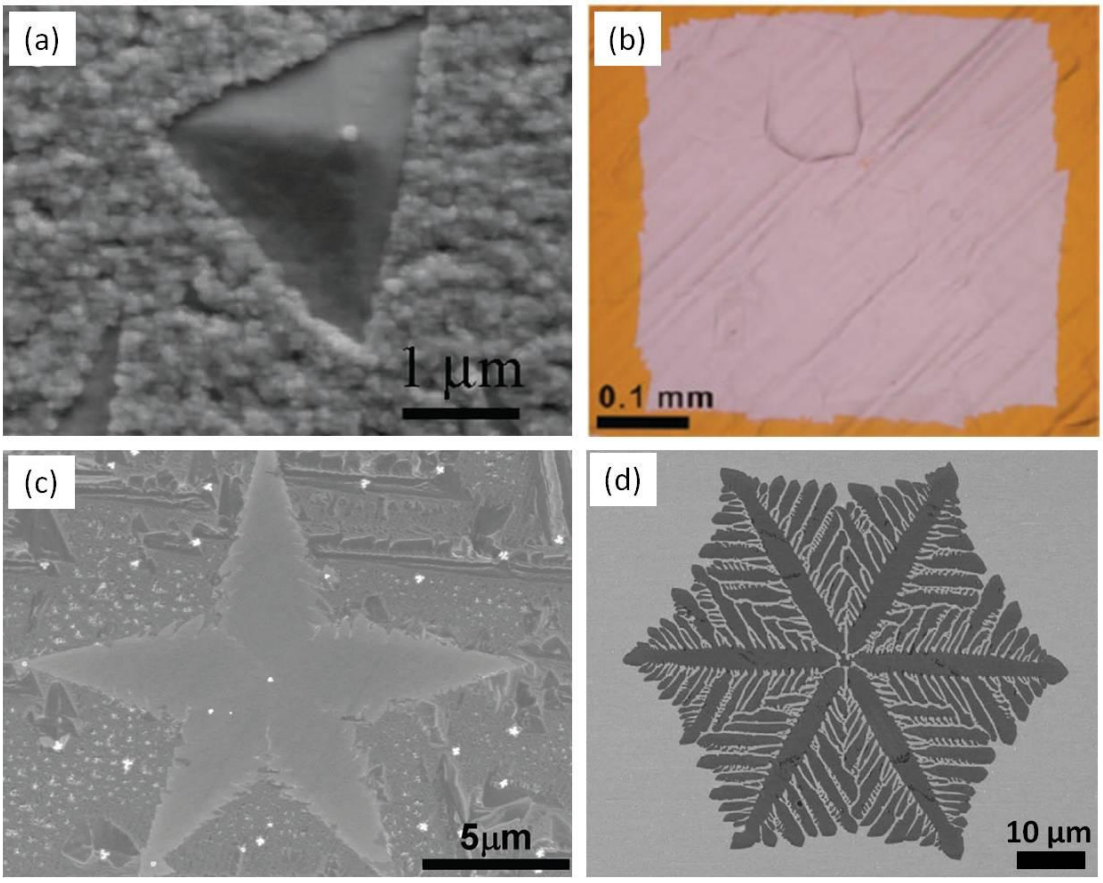

Figure 2.15: Multi types of graphene domain shapes synthesized by the Cu-CVD. (a) Triangle-shaped. Adapted from Liu *et al*.[190] (b) Rectangle-shaped. Adapted from Wang *et al*.[200] (c) Five-lobed. Adapted from Geng *et al*.[191] (d) Dendritic hexagonal. Adapted from Wu *et al*.[68]

2.3.7 Graphene-Cu Interaction

Although the dependence of the graphene domain shapes on the Cu crystallographic orientation indicates the graphene-Cu epitaxial relationship, the epitaxial interaction should be relatively weak. This is intuitively because only the π-electrons of the carbon atoms not on the domain edges are available for bonding with the substrate Cu atoms while their σ-electrons have already been inter-connected with three nearest neighbours. Consequently there could be more than one orientation of the graphene lattice relative to the underlying Cu lattice that are energetically degenerate, as suggested by the DFT studies on both the Cu (100) and Cu (111) surfaces.[201,202] This also agrees with the STM observations of two predominant Moiré patterns from graphene grown on the Cu (111) single crystals (Figure 2.16).[165] In one of the patterns the graphene lattice is well aligned with the underlying Cu (111) lattice while in the other it is rotated by ~7°.

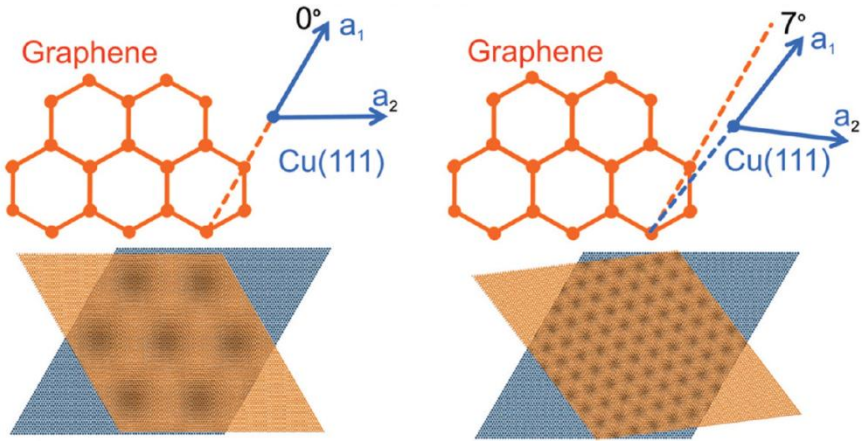

Figure 2.16: Schematic illustration for the STM-observed Moiré patterns of graphene grown on Cu (111). Left: ~0° rotation. Right: ~7° rotation. Adapted from Gao *et al*.[165]

In the real Cu-CVD processes, the thermodynamic graphene-Cu interactions also exist. Most Cu-CVD recipes use high growth temperature of ~1000°C for the purpose high quality.[161] This is already close to the melting temperature T_m of the bulk Cu (1083°C in ambient conditions). Consequently the topmost layers of the Cu surface are pre-melted after ramping and annealing. The pre-melted Cu atoms are evaporated substantially and removed by the flowing gas,[203] which has a higher rate in the graphene-free regions than in the graphene-covered regions.[204,205] Therefore, the Cu surface outside an enlarging graphene domain loses the Cu atoms much faster than that below the domain. In the case of a polygonal graphene domain, the Cu surface below the domain, which is originally flat, will accordingly evolve into a polygonal pyramid

via the lateral evaporation.[206] Therefore the real graphene-Cu interface becomes more or less corrugated after the high temperature CVD processes. It is worth noting that, if the Cu evaporation is overly heavy, the hydrocarbon species accumulated on the Cu surface might be evaporated along with the Cu atoms.[63] This could result in a low graphene nucleation density.

2.3.8 Domain Boundaries of Cu-catalyzed Graphene Film

The existence of the lattice orientation disorders means it is almost unavoidable for the defective stitching of the neighbouring domains that have grown sufficiently large. For instance, the coalescence of two domains with different lattice orientations would give rise to the typical domain boundaries. Even if some domains are strictly parallel aligned, the carbon atoms at the interfaces of the merged domains are generally of translation mismatch. In this sense the domain boundaries are almost inherent to the Cu-CVD-derived graphene as a necessary consequence of the randomly located nucleation and the randomly oriented growth.

The aberration-corrected annular dark-field scanning transmission electron microscopy (ADF-STEM) image in Figure 2.17(a) uncovers the detailed atomic structure of the typical boundary between two merged graphene domains that are relatively rotated by ~27°.[74] The boundary is not straight. It consists of the alternating pentagon-heptagon pairs and a few distorted hexagons. Clearly the atomic configurations along the boundary are not periodic and hence the domain boundaries can be seen as line defects of graphene that break the in-plane periodicity of the honeycomb lattice. The spatial Raman spectroscopic mapping in Figure 2.17(b) shows that the D-band intensity of the domain merging regions is significantly higher than within the domains which confirms the defective nature of the domain boundaries.[188] Many studies have claimed the domain boundaries are responsible for the degradation of the electronic transport properties of graphene.[32,35,74,85,188,207–210] For instance, the graphene mobility measurements of Ogawa *et al*[211] (shown in Figure 2.17(c)) have found that the inter-domain mobility is significantly lower than the intra-domain mobility. The temperature dependences of these two mobility in Figure 2.17(d) further shows that the inter-domain mobility is much less sensitive to the temperature change than the intra-domain mobility.[211] This suggests that the major charge carrier scattering centres limiting the inter-domain mobility should be most likely the domain boundary

instead of the temperature-dependent phonon scattering. Therefore it is of fundamental importance to reduce the graphene domain boundaries in order to preserve the extraordinary electronic properties of graphene. This further calls for improving the CVD towards graphene films with large domains as the number density of the boundaries is inversely proportional to the average domain area.[59,61]

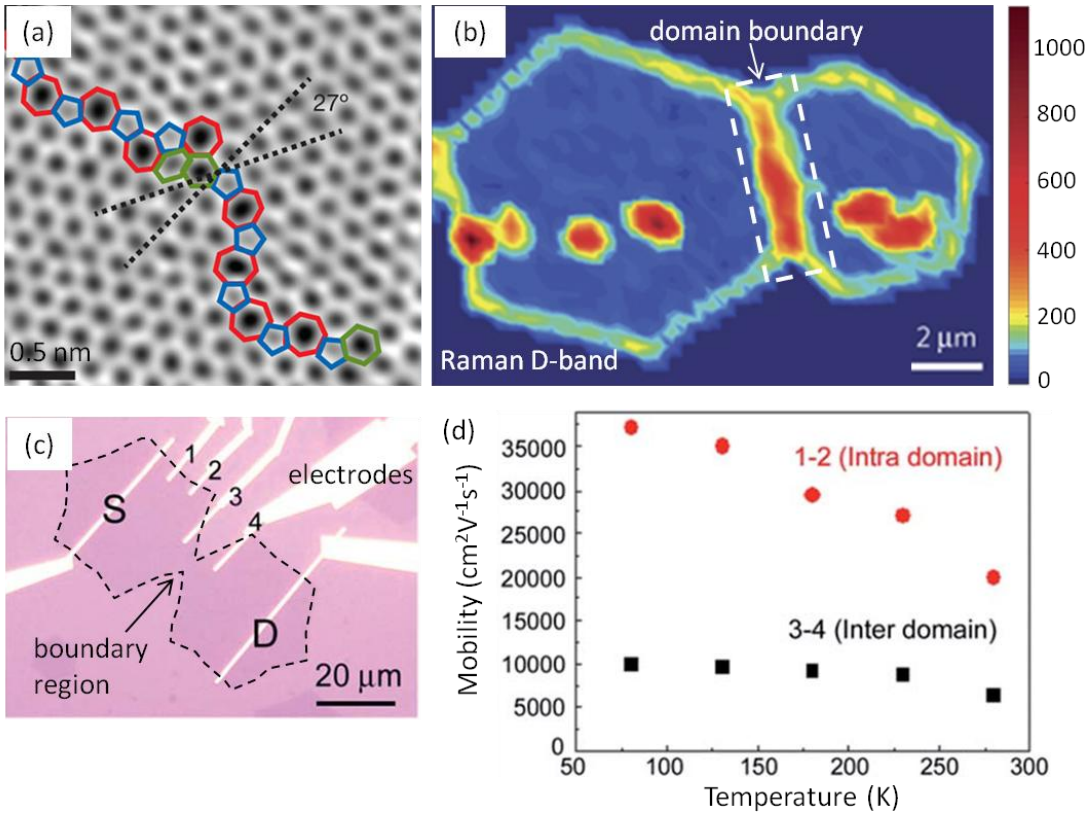

Figure 2.17: Domain boundary of CVD graphene. (a) ADF-STEM image of the graphene transferred onto a TEM grid showing two domains intersecting with a 27° relative rotation. The blue pentagons, red heptagons and the green hexagons (distorted) outline the boundary. Adapted from Huang *et al.*[74] (b) Raman D-band mapping of the spatially merged CVD graphene domains. Adapted from Yu *et al.*[188] (c) Optical microscope (OM) image of the mobility measurement set up for two merged CVD graphene domains that have been transferred onto the SiO_2-coated Si substrate. The electrodes 1-2 and 3-4 measure the intra-domain and inter-domain mobility, respectively. Adapted from Ogawa *et al.*[211] (d) The temperature-dependences of the intra-domain (red circles) and the inter-domain mobility (black squares). Adapted from Ogawa *et al.*[211]

2.3.9 Saturated Coverage of Cu-catalyzed Graphene

For Cu-catalyzed CVD, the coalescence of two graphene domains terminates the local growth because the Cu surface underlying the boundary region is catalytically poisoned, i.e., the result of the self-limiting nature. Yet this is not the only mechanism for the growth termination. Experimental research has found that under certain CVD conditions the graphene growth could saturate at incomplete coverage even the carbon precursors are still kept supplying.[182,212,213] The SEM image in Figure 2.18 demonstrates a typical graphene film with incomplete coverage grown on Cu.[183] The graphene domains are not fully connected thus leaving hole-like uncovered Cu regions that are randomly distributed. They normally appear brighter under SEM than the graphene-covered surface due to stronger electron reflectivity. The mechanism of the coverage saturation deserves research focus since full coverage graphene, i.e., continuous graphene, is indispensable for large scale integration of graphene-based applications with high spatial homogeneity. The CVD experiments have found that the saturated coverage is closely dependent on the partial pressure of the carbon precursor. For instance, Li *et al*[61] has observed a limited final graphene coverage at 1035℃ using the CH_4 partial pressure of 160 mTorr contrasting to a full coverage using > 500 mTorr CH_4 partial pressure. The growth temperature also plays a crucial role. Assuming that the chemisorption and desorption rate of carbon species are balanced once the surface supersaturation is reached, Kim *et al*[183] suggests the graphene growth is chemically driven by the concentration difference between the critical supersaturation level for nucleation and the equilibrium level for grown graphene, $c_{\mathrm{nuc}} - c_{\mathrm{eq}}$. Hence the graphene growth terminates when the supersaturation edge is exhausted and the saturation coverage θ_{sat} equals $\left(c_{\mathrm{nuc}} - c_{\mathrm{eq}}\right)/\rho_G$, where $\rho_{\mathrm{G}} = 0.382$ Å^{-2} is the atomic area density of graphene. The graphene film can therefore reach full coverage provided $\theta_{\mathrm{sat}} > 1$.[182,183]

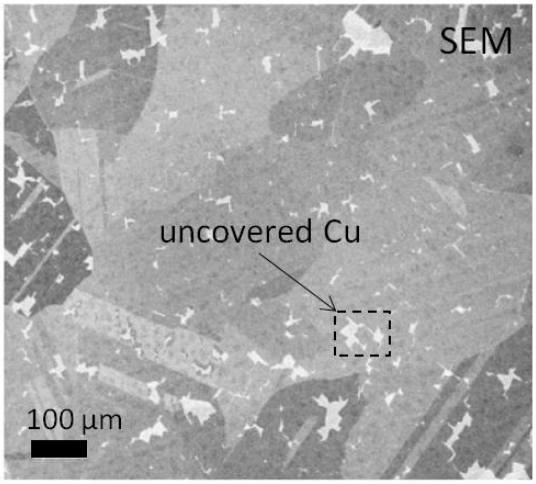

Figure 2.18: SEM image of Cu-supported graphene with incomplete coverage. The dashed box outlines a typical Cu region that is not fully covered by graphene. Adapted from Kim *et al*.[183]

3 METHODOLOGY

This section presents the main experimental methods used in this research, including the graphene synthesis set up, the graphene transfer procedures and the characterization techniques.

3.1 Hot-wall APCVD

Depending on the classification criterion there are different types of CVD systems designed for synthesis of specific materials. In terms of the energy sources, the CVD can be mainly classified into the thermal CVD, for which the precursors are heated under high temperature, and the enhanced CVD where the precursor molecules are activated by plasma, ions or lasers.[214] They can also be classified into the hot-wall or cold-wall CVD. For the hot-wall CVD the entire reactor is heated. This promotes uniform temperature distribution in the reaction zone and consequently the deposition rate and the film quality can be homogenous across the reactor-scale. Yet some contaminating by-products might be deposited on the hot walls as well. For the cold-wall CVD, only the substrate holder is heated while the reactor walls are kept cool. The corresponding synthesis processes are clean but the size of the uniform deposition zone is limited. The total gas pressure of the CVD systems ranges from several mTorr, typically for the low pressure CVD (LPCVD), to 1 atm for the atmospheric pressure CVD (APCVD). The concentration distribution of the gaseous reactants in the LPCVD is spatially more uniform that in the APCVD. The deposition rate is normally higher in APCVD because of a higher partial pressure of the precursors.

This PhD research has mainly explored the thermal hot-wall APCVD for graphene synthesis using Cu as the catalytic substrate. The major reason to choose the thermal heating as the energy source is that the atomic-thick graphene is vulnerable to the energetic interaction with the plasma, ions and lasers. The Cu-catalyzed CVD of graphene normally requires a high processing temperature close to the Cu melting point. A high background pressure is thereby preferred to suppress the thermal evaporation of Cu which would otherwise damage the graphene film atop as well as pollute the reactor walls. APCVD is chosen as such.[54,63] APCVD is also compatible with the continuously fed R2R processing.[54,70]

A split tube furnace is used to implement the hot-wall APCVD of graphene. Figure 3.1 shows its basic structure. The reaction zone consists of a sealed quartz tube of 60 mm diameter. The catalytic Cu foil (Alfa Aesar, 99.8% purity, 25 μm thickness) is loaded into the tube centre. The furnace is then sealed and evacuated to a base pressure of ~0.1 bar by a mechanical pump. The Ar gas is flown into the tube through the gas inlet to raise the pressure to ~ 1 atm which will then be maintained throughout the entire CVD process. Additional gases might be added to adjust the chemical property of the gas environment to a desired state. The tube is then heated under the composite gases by the surrounding coil wires (controlled by a Carbolite controller) to the desired temperature (~1000 ℃ in this research) at a ramping rate of ~20 ℃/min. The catalyst is annealed at the stabilized temperature for certain time. The gaseous reactants (CH_4 and H_2 in this research) in a chosen composition are flown into the tube to initiate the graphene growth on the catalytic Cu. After a specific duration the growth is terminated by switching off the carbon supply and the thermal heater. The system is cooled down to room temperature under the protection of Ar and H_2. The graphene/Cu sample is then unloaded from the tube for further investigations.

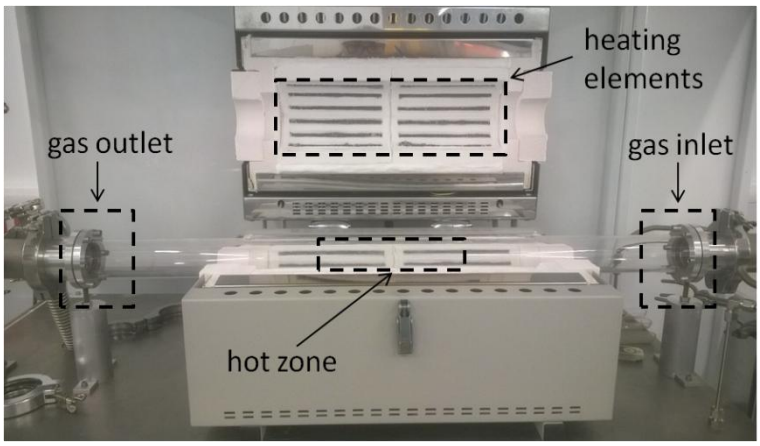

Figure 3.1: Photograph of the tube furnace of a hot-wall APCVD

3.2 Graphene Transfer

After the Cu-catalyzed CVD process, the synthesized graphene needs to be transferred from the original Cu substrate onto the secondary target substrates for quality characterizations or subsequent fabrications. In this research the conventional wet transfer method is used.[53,215] The principle is to release the graphene film by etching the metallic Cu using a wet chemical etchant. The schematic in Figure 3.2 demonstrates the basic procedures. First the post-growth graphene/Cu sample is spin coated with a thin layer of the Poly(methyl methacrylate) (PMMA) A4 950 photo-resistance (~300 nm thickness) at a rotation rate of ~4000 rpm for ~ 40 s. By doing this the graphene film is well protected by the PMMA coating throughout the subsequent transfer steps. The sample is then treated by a mild oxygen plasma in the Reaction Ion Etching (RIE) system. The graphene grown on the backside of the Cu foil is removed by the plasma while the front side graphene is protected by the PMMA against etching. Next the PMMA/graphene/Cu stack is floated on the 0.05 M aqueous ammonia persulfate (APS, $(NH_4)_2S_2O_8$), a conventionally used Cu etchant. The Cu atoms in direct contact with the APS solution will be gradually etched since the backside graphene has been removed by RIE. Empirically it takes ~4h for the 25 μm thick Cu foil to be completely dissolved in the 0.05 M APS solution. The PMMA/graphene stack is then transferred to fresh de-ionized (DI) water for rinse, which is repeated for 3 times. Next the sample is hooped

onto the target substrate which is then left overnight in air to gently dry the residual water. By doing this the graphene film is tightly bound to the substrate. Finally the dried sample is immersed in acetone overnight to remove the PMMA coating. This leaves the original graphene film on the target substrate. After a short rinse in isopropyl alcohol (IPA) it is ready for subsequent studies.

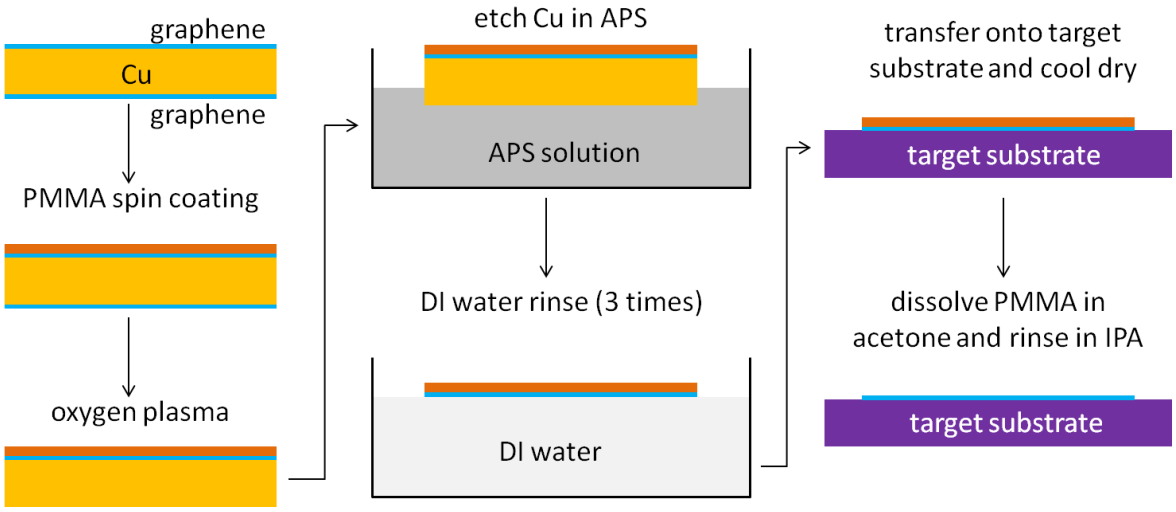

Figure 3.2: Schematic illustration for the wet transfer procedures using APS as the Cu etchant.

3.3 Characterization Techniques

3.3.1 Scanning Electron Microscope

Scanning Electron Microscope (SEM) is a microscope extensively used to study the specimen surface morphologies. It works by scanning a focused beam of high energy electrons across a specimen surface. The interaction between the incident electron beam and the specimen generates the secondary and backscattered electrons that are collected by the electron detectors to create images. It has the advantages of high resolution (~<100 nm), high contrast and high surface sensitivity. It is also a rapid and non-invasive characterization tool. These make it suitable for graphene imaging.[216,217]

Considering the atomic thickness of the graphene film, an effective SEM investigation of the graphene surface necessarily requires the electrons being detected mainly come from the upper layers of the electron-sample interaction volume. Therefore the in-lens detector is preferred which directly collects the secondary electrons generated near the incident beam's impact point. Besides, a relatively low acceleration voltage (~1 kV) should be used because the atomically thin graphene can be easily

penetrated by the high energy electrons, which means the underlying substrate instead of the graphene itself will be imaged. By using the optimized SEM imaging conditions, fine features of the graphene surface can be observed including the wrinkles, folding lines, defects and multi-layer patches.[217] This enables effective characterizations of the continuity, uniformity, and quality of the CVD graphene sample.

This PhD research has mainly used the ΣIMGA™ field emission scanning electron microscope (FESEM). The optimized acceleration voltage is ~1 kV and the working distance is maintained at ~3 mm.

3.3.2 Optical Microscope

The Nikon ECLIPSE LV 150N optical microscope (OM) is used to rapidly investigate a variety of specimen involved in this research including the catalytic Cu foils, the CVD graphene grown on Cu, the graphene transferred onto secondary substrates, etc.

3.3.3 Raman spectroscopy

For study of graphene, Raman spectroscopy is particularly useful in that the fingerprint spectra reveals the crystalline quality and the number of layers of the graphene sample. Careful control of the incident laser power can minimize the burning damage to an acceptable extent. Hence the Raman spectroscopy is rapid and low-invasive. This research has used the Renishaw InVia Raman spectrometer. For the CVD graphene transferred onto the SiO_2 coated Si substrate, 514 nm laser is used at ~500 μW with a 50X objective (spot diameter ~1.5 μm).

3.3.4 Optical Profilometry

Optical profiler is an interference microscope used to measure the height variations of the sample surface. It works by comparing the optical path difference between a test surface and a reference surface. In this research the Wyko NT1100 optical profilometer is used to study the surface roughness of the Cu foils. It can rapidly acquire a morphology map of the Cu surface over ~50 μm×50 μm area.

3.3.5 Charge Carrier Mobility Measurements

The charge carrier mobility measurement provides an reliable assessment of the crystalline quality of the CVD graphene. In this research the mobility is measured using the Hall effect. First the monolayer CVD graphene film is transferred onto a SiO_2(300

nm)-coated Si wafer using the previously described wet transfer method. Then Hall devices with Van der Pauw geometry are fabricated on the wafer with 50×50 μm^2 graphene area patterned by electron-beam lithography. Metal electrodes (45 nm Au /5 nm Ni) are deposited by thermal evaporation on the corners of the graphene squares. The mobility and the areal density of the charge carriers are measured under 1T magnetic field at room temperature using the Hall and Van der Pauw Measurement System of MMR Technologies.[218]

3.3.6 Electron Backscatter Diffraction

Electron Backscatter Diffraction (EBSD) is a micro-crystallographic characterization technique used to discriminate the crystal orientation and phase of the specimen materials. The micro-structural information is obtained from the Bragg diffraction of the electrons by the specimen crystal. In this research the Oxford NordlysMax EBSD detector equipped within the Philips XL30 sFEG SEM is used to identify the crystal orientations of the polycrystalline Cu foils. The effects of the Cu crystallographic orientations on the growth of the Cu-catalyzed graphene are then analyzed based on the EBSD information.[219]

3.3.7 Transmission Electron Microscope

The JEOL 2100 transmission electron microscope (TEM) (80 kV) is used to conduct electron diffraction study on the monolayer CVD graphene. This reveals the crystalline structure of the graphene lattice at the atomic level. For this purpose the synthesized graphene is transferred onto a 3mm-diameter holey carbon copper grid (Agar Scientific No. AGS147).

4 GROWTH OF CONTINUOUS MONOLAYER GRAPHENE WITH MILLIMETRE-SIZED DOMAINS USING INDUSTRIALLY SAFE CONDITIONS

Part of the results in this chapter have been published in:

Growth of Continuous Monolayer Graphene with Millimeter-sized Domains Using Industrially Safe Conditions Xingyi Wu, Guofang Zhong, Lorenzo D'Arsié, Hisashi Sugime, Santiago Esconjauregui, Alex W Robertson, and John Robertson. *Scientific Reports*, **6**, 21152 (2016)

4.1 Introduction

For use in mass production, there are two fundamental criterion that the Cu-CVD synthesized graphene has to simultaneously meet. First, the graphene needs to be in the form of continuous films. This is to improve the yield and performance homogeneity of the functional device arrays that are integrated with graphene (see Figure 4.1(a)). If the underlying graphene is spatially discontinuous, only the device arrays assembled on the graphene regions can properly function (see Figure 4.1(b)), which will cause low yield and performance inhomogeneity. Second, the spatial density of the graphene domain boundaries (at the joint of neighbouring domains) needs to be sufficiently low so as to ensure high electronic conductivity and mobility of the entire graphene film. For this purpose the average domain size has to be improved for fewer domain boundaries.

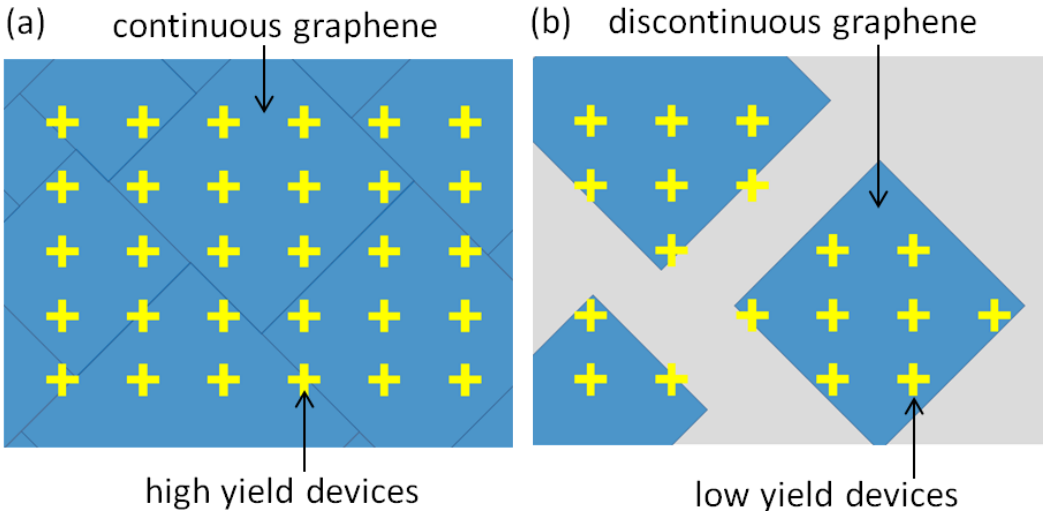

Figure 4.1: Schematic illustration for device integration on (a) continuous and (b) discontinuous graphene film. The blue squares represent the CVD graphene domains while the yellow crosses represent the device arrays integrated in contact with graphene.

The growth of continuous graphene films via the Cu-catalyzed CVD approach has been first achieved in 2009 by Ruoff's group.[53] Since then there have been significant developments in the growth technology of continuous graphene. Nowadays it can be grown under both low and atmospheric pressures,[53,178] up to 100 meter-scale using a roll-to-roll apparatus,[21] at low temperature (<420°C),[220] and with a rapid growth rate.[221] However, a common problem with the current continuous graphene films lies in their high spatial density of the domain boundaries because the typical domain sizes are limited below ~300 μm.[54,61,221,222] A lot of efforts have then been devoted to improving the graphene domain sizes by tailoring the Cu-CVD processes. This leads to the

successful synthesis of millimetre to centimetre-sized graphene single crystals in recent years.[59,62,72,78–82] Most of them are achieved by rationally modifying the pristine Cu-CVD method. This generally includes using a high H_2:CH_4 gas ratio[59,63] and appropriate catalyst pre-treatments, such as Cu electro-chemical polishing (or 'electro-polishing' for short),[54,78,223,224] long time Cu annealing,[78] high temperature re-solidifying of Cu,[79] surface oxygen-induced Cu passivation,[59,62,72,80–82] Cu foil enclosure structures, etc.[203] However, these attempts to grow large domains have been limited to isolated graphene single crystals rather than as part of an industrially useable continuous film. The graphene synthesized by these methods is generally discontinuous with randomly positioned and orientated domains making them unsuitable for large scale device integration, which requires the high yield of continuous graphene.

In addition to the physical properties of graphene itself, the safety issue of the Cu-CVD process also needs to be re-considered before transferring the laboratory recipe into the industry-level manufacture. The current CVD recipe generally use H_2 as one of the forming gases. Yet H_2 is known as an explosive gas (the explosive limit of H_2 is 4-75 vol% at room temperature in air) that needs to be carefully monitored and controlled in its presence. For Cu-CVD of graphene, the H_2 safety issue is particularly serious because the high growth temperature (~1000 ℃) increases the potential risk of H_2 explosion. Meanwhile, the R2R CVD growth further emphasizes the importance of the minimizing the H_2-associated risk because the truly R2R reactors are open to air.[55] Therefore the conventional CVD method has to be improved to ensure the H_2 safety for large scale production. Although there have been several reports on graphene growth using no H_2[221,225,226] or diluted H_2,[81,223,227–232] their charge carrier mobilities are limited below ~4000 $cm^2V^{-1}s^{-1}$, which is not qualified for the 'electronic-grade' applications.[60] Besides, the H_2-free growth removes a useful parameter that could have been used to engineer the product properties such as the graphene quality, coverage, and domain size. In this sense the growth of graphene with high electronic quality still remains a challenge subject to the constraints of using industrially safe conditions.

This chapter demonstrates the systematic optimization of the standard Cu-CVD approach towards the growth of continuous monolayer graphene films with millimetre-sized domains under intrinsically safe, atmospheric pressure growth conditions. The average domain size reaches ~1 mm, which is the largest achieved to date for continuous graphene. The hole mobility measured in air reaches ~5,700 $cm^2V^{-1}s^{-1}$, the

highest value among the reported mobility using similarly low concentrations of H_2. Such a progress is achieved by the comprehensively improved Cu-CVD techniques, including the electro-polishing and non-reductive annealing of the Cu foils as well as optimization of the CH_4 concentration. This work thereby widens the possibility of up-scaling the current Cu-CVD technology for use in large scale production of graphene.

4.2 Optimizations of Cu-CVD of Graphene

4.2.1 Electro-chemical polishing of Cu Foils

The systematic optimization starts with the establishment of a preliminary APCVD recipe, that is, a recipe that can synthesize graphene with the base grade quality. The commercial Cu foils are used as catalysts. The APCVD growth is conducted in the thermal furnace following the general procedures described in Methodology (Chapter 2). More specifically the Cu foil is heated up to 1030 ℃ at the ramping rate of ~20 ℃/min under the flow of 3920 standard cubic centimetre per min (sccm) Ar and 80 sccm H_2. The Cu foil is annealed at this temperature for 0.5 h by the H_2. Graphene growth is initiated by adding 0.4 sccm CH_4 to the Ar-H_2 mixture (CH_4 concentration = 100 ppm). It is worth noting that the volume concentration of the flammable gases (CH_4 and H_2) are diluted by Ar to strictly below the lower explosive limit (LEL) throughout the entire process. The growth time is varied to achieve graphene with various level of coverage. Figure 4.2 schematically summarizes the temperature and gas composition used in each stage.

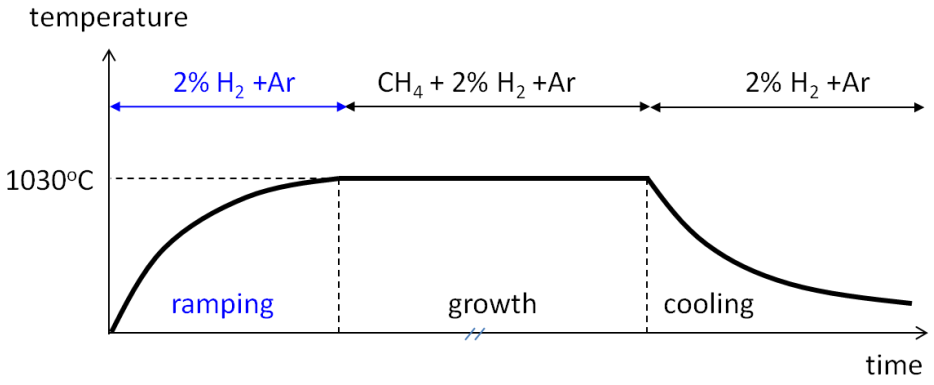

Figure 4.2: Schematic procedure for the preliminary APCVD. The Cu catalyst is heated up in 2% diluted H_2.

The Cu foil after graphene growth appears shinier than that before growth as shown in Figure 4.3(a) and (b). This is most probably because that the thermal annealing of Cu

in the H_2 environment has reduced the surface Cu oxides and promoted the re-crystallization of the Cu grains. Yet the SEM image of the graphene/Cu sample still reveals many imperfections (see Figure 4.3(c)). First, the graphene domains are predominantly distributed along some preferential orientation on the Cu surface. This is normally associated with the sharp protrusions and grooves that are induced on the Cu surface during the foil manufacturing process. The surface defects along the grooves provide more active sites for graphene nucleation than the terrace regions. The entire domain distribution is thereby of poor homogeneity. Second, the lateral domain sizes are merely ~20 μm. Third, there is a significant number of 'dirty' contaminating particulates on the Cu surface. The composition of these contaminants is still unclear. Celebi *et al*[233] has detected Cl, Cu, C and O in these particles using the nano-Auger spectroscopy.

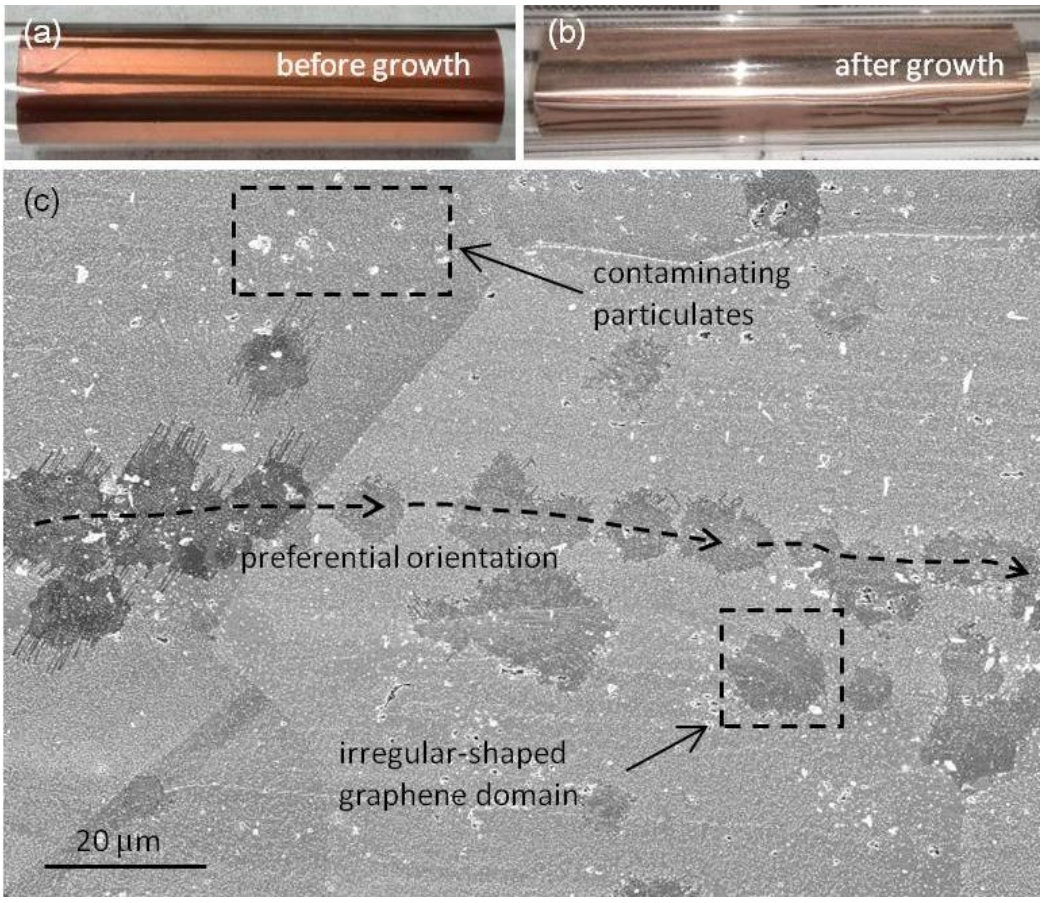

Figure 4.3: Photograph of the Cu foil wrapped inside the quartz tube (a) before growth and (b) after growth. (c) SEM image of the partial coverage graphene grown on Cu.

Since the Cu-catalyzed CVD of graphene is mostly a surface-mediated process, the condition of the Cu surface largely determines the properties of the as-grown graphene. The existence of the preferential orientation and the contaminating particulates further

suggests that the pristine surface of the as-received commercial Cu foil needs to be modified for improving the graphene quality. In particular, the macro-observable Cu surface grooves should be removed. The widely recommended electro-polishing has been used in this research as a first attempt to engineer the Cu surface.[54,78,223,234] For this an electro-chemical cell has been built. The basic components are shown in Figure 4.4(a). 85% H_3PO_4 solution filled in a container is used as the electrolyte. To ensure a high spatial symmetry of the electrical field across the electrolyte, a rectangular container (5 cm × 10 cm × 10 cm) is chosen, which will promote homogenous electro-polishing over large areas of Cu. Two pieces of 10×10 cm^2 Cu foils are placed against the opposite inner walls of the container. In this way the two Cu foils immersed in the electrolyte are uniformly distanced by 5 cm.

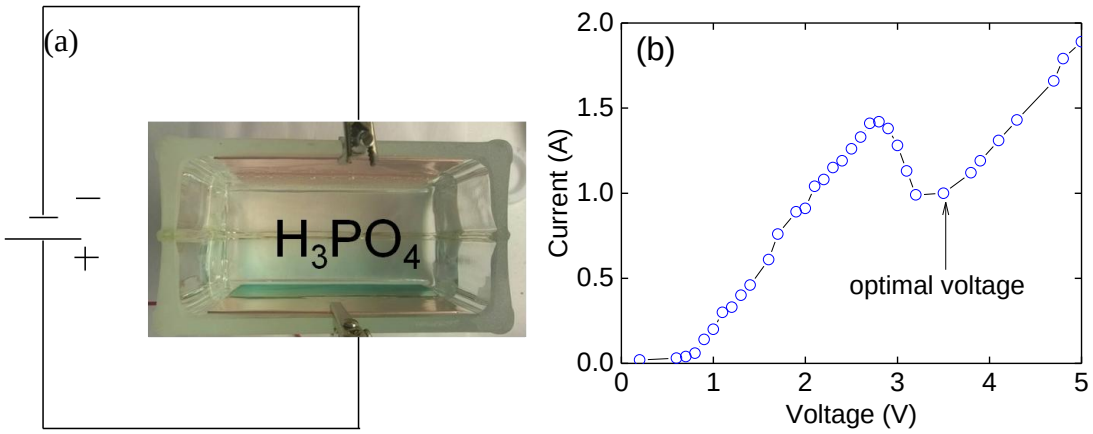

Figure 4.4: (a) Set up of the home-built electro-polishing cell using H_3PO_4 as the electrolyte and Cu as electrodes. (b) Characteristic I-V curve of the H_3PO_4-Cu electro-polishing system.

One of the Cu foils is then connected to the anode of an external direct current (DC) power supply and the other to the cathode. Driven by the voltage differences at the metal-electrolyte interfaces, the Cu atoms of the anode foil surface are gradually dissolved. They transport across the electrolyte directed by the electrical field towards the cathode Cu foil where they deposit on the surface. Following the general principles of electro-polishing, the DC power supply is set to work in the constant voltage mode.[54,78,235] The corresponding current is measured at each voltage level. Figure 4.4(b) shows the characteristic I-V curve. It has a notable negative resistance region followed by a short plateaux, both of which have been intensively addressed in classic study of electro-polishing.[235,236] The optimal voltage for electro-polishing has been claimed to be around the end of the plateaux,[235] which is close to 3.5 V in this set up. Figure 4.5 shows the photographs of the Cu foils treated at the optimal voltage for a couple of

minutes. The anode Cu that is immersed inside the electrolyte gets electro-polished and consequently appears shinier than the pristine Cu surface. The cathode Cu gets electro-plated and consequently coated with reddish layers of Cu atoms.

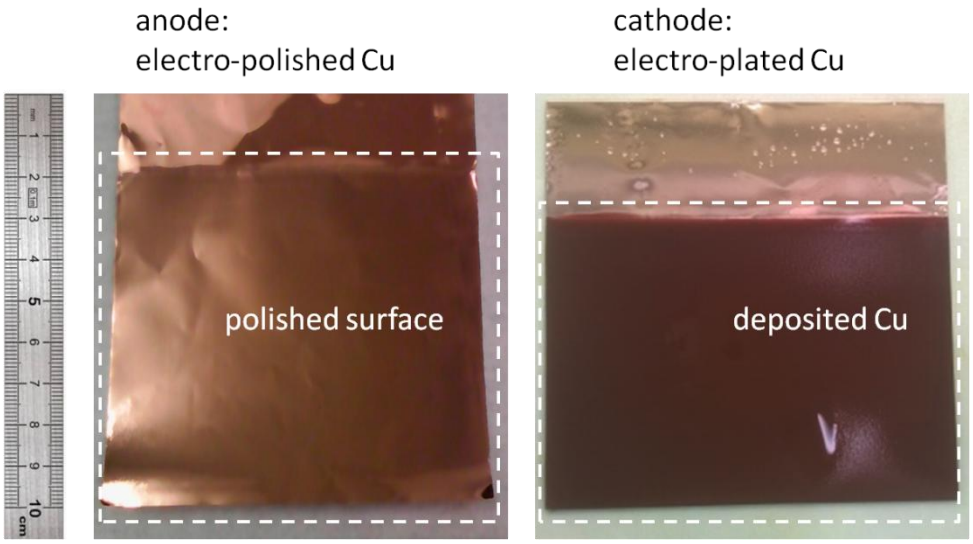

Figure 4.5: Photographs of the Cu foils after the electro-polishing treatments. The anode foil is electro-polished while the cathode foil is electro-plated. Dashed rectangles outline the polished and the plated region.

With the working voltage fixed at the optimal point, the polishing time is then optimized. Figure 4.6 summarizes the effects of polishing time on the Cu foil surface morphology. Figure 4.6(a) and (b) show that shorter than 15 min polishing is obviously insufficient to remove the surface grooves. Yet Figure 4.6(c) and (d) suggest longer polishing time tends to create more surface pits, which is an undesirable consequence of more oxygen bubbles accumulated on the Cu anode. Considering the trade-off between reducing the grooves and suppressing the pits, 20~30 min can be taken as the optimal polishing time given the other conditions of this set up. Therefore throughout this CVD research the commercial Cu foil is always electro-polished at 3.5 V for 20 min. It is finally rinsed by isopropyl alcohol and de-ionized water to remove the residual acid and metal anions.

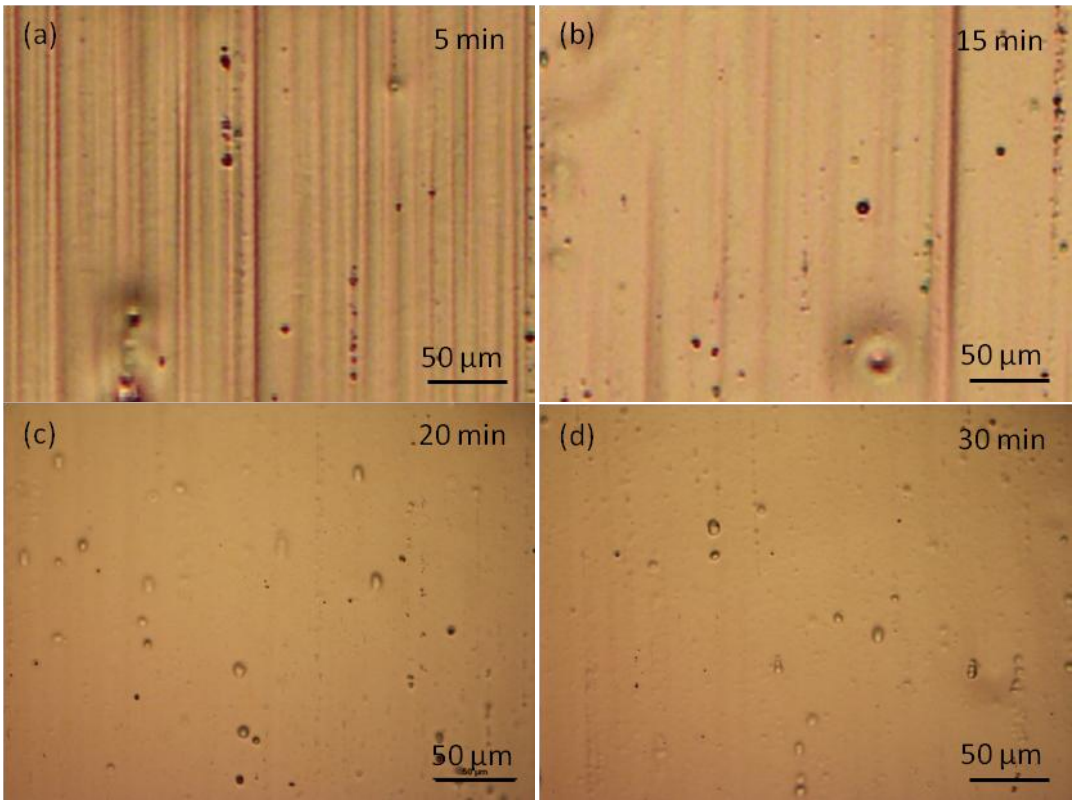

Figure 4.6: Effect of electro-polishing time on the Cu foil surface morphology. OM images of the Cu foils polished in (a) 5 min, (b) 15 min, (c) 20 min, and (d) 30 min, respectively.

The OM image in Figure 4.7(a) clearly shows the parallel groove structures on the pristine Cu, which becomes hardly observable upon the appropriate electro-polishing as shown in Figure 4.7(d). Such a morphological improvement is also confirmed by the optical profilometry mappings shown in Figure 4.7(b) and (e). More specifically, the typical root mean square (RMS) roughness (R_{rms}) drops from 320 to 100 nm over a 50 µm range as shown in Figure 4.7(c) and (f).

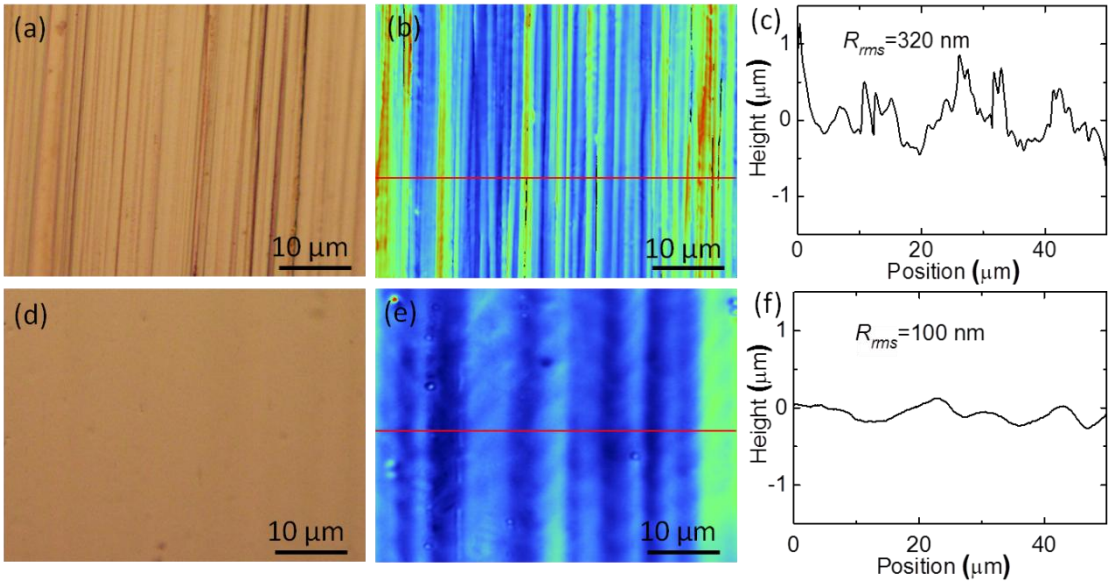

Figure 4.7: Effects of electro-polishing on the Cu surface morphology. OM images of (a) the pristine and (d) the electro-polished Cu foil surfaces. Optical profilometry mappings of (b) the pristine and (e) the electro-polished Cu foil surfaces. Line profiles of the surface roughness of (c) the pristine and (f) the electro-polished Cu foils, corresponding to the red lines marked in (b) and (e), respectively.

4.2.2 Non-reductive Annealing of Cu Foils

The electro-polished Cu foil is then used to catalyze the growth of graphene using the CVD condition described above. Figure 4.8(a) and (b) demonstrates the improved growth on the polished Cu. First, the spatial distribution of the domains is much more homogenous on the polished Cu surface than on the pristine Cu. This is mostly because the electro-polishing has effectively removed the active sites along the rolling grooves which would otherwise catalyze the growth of more domains than the terrace regions. Second, the number of the contaminating particulates is dramatically reduced by electro-polishing and consequently the sample surface appears almost spotless (Figure 4.8(b)). This is reasonable considering that the average thickness of the Cu atoms removed under the optimal polishing condition (3.5 V, 20 min) is estimated from Figure 4.7(c) and (f) to be ~200 nm. The impurities in the topmost layers should have been removed by such a deep polishing. Throughout the subsequent research, the optimally polished Cu foil will be used as the benchmark catalyst for all graphene CVD experiments.

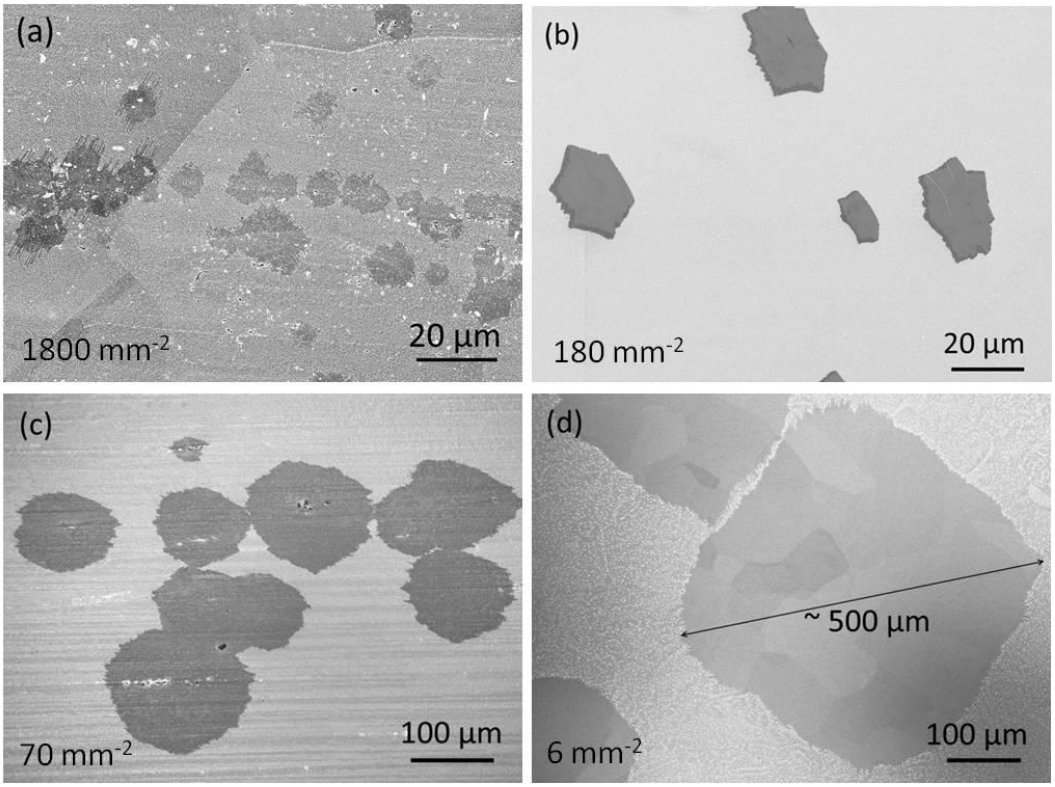

Figure 4.8: Effects of electro-polishing and non-reductive annealing on graphene nucleation. SEM image of the partial coverage graphene grown on (a) ,(c) the pristine Cu foils and (b), (d) the electro-polished Cu foils. The Cu foils are heated up in the diluted H_2 for (a) and (b) while in the pure Ar for (c) and (d). Growth conditions: 1030°C, 2% H_2, 100 ppm CH_4, 20 min for (a) and (b); 1030°C, 2% H_2, 100 ppm CH_4, 40 min for (c) and (d). Nucleation densities are ~1800 mm^{-2}, ~180 mm^{-2}, ~70 mm^{-2}, and ~6 mm^{-2}, respectively.

By reducing the active nucleation sites along the surface grooves, the electro-polishing has also decreased the graphene nucleation density by a factor of ~10 (see Figure 4.8(a) and (b)). However the average domain size is still limited in the order of tens of micrometres. One of the potentially effective strategies for synthesizing even larger domains is to further reduce the areal density of the Cu surface active sites. This can be achieved by the oxygen-aided catalyst passivation. Zhou *et al*[59] has reported the growth of ~5 mm-sized graphene single crystals by maintaining a catalytic inactive Cu oxide layer during the annealing stage. By both CVD experiments and DFT calculations, Hao *et al*[62] has further validated the effect of Cu surface oxygen on drastically suppressing the graphene nucleation density. In their work the controlled supply of the surface oxygen enabled the growth of the centimetre-scale single crystalline graphene domains. The surface oxygen is also shown by Xu *et al* to significantly accelerate the graphene growth.[72] In this CVD set up, the surfaces of the electro-polished Cu foils have been oxidized to a suitable extent simply by heating up

the Cu in the pure Ar atmosphere. The entire CVD procedure is shown in Figure 4.9. H_2 is not introduced into the reactor until CH_4 is flown in. This ensures the native oxide layer on the Cu surface can be maintained under the protection of Ar in the absence of H_2. Since the oxidized Cu are catalytically less active than the metallic Cu, the non-reductive annealing should be able to partly passivate the surface nucleation sites. Figure 4.8 shows the graphene nucleation density has dropped by around 30-fold on both the pristine Cu foils (see Figure 4.8(a) and (c)) and the electro-polished Cu foils (see Figure 4.8(b) and (d)). Therefore the domain sizes that can be potentially achieved at full coverage are dramatically increased. For instance, the non-reductive annealing yields graphene single crystals as large as 100 μm even on the pristine Cu as seen in Figure 4.8(c). A combinational use of the electro-polishing and the non-reductive annealing reduces the nucleation density to the order of several nuclei per mm^2 (Figure 4.8(d)).Therefore the diagonal size of the graphene domain grown in the optimized manner has reached ~500 μm, about ~20 times larger than that on the pristine Cu using the reductive annealing.

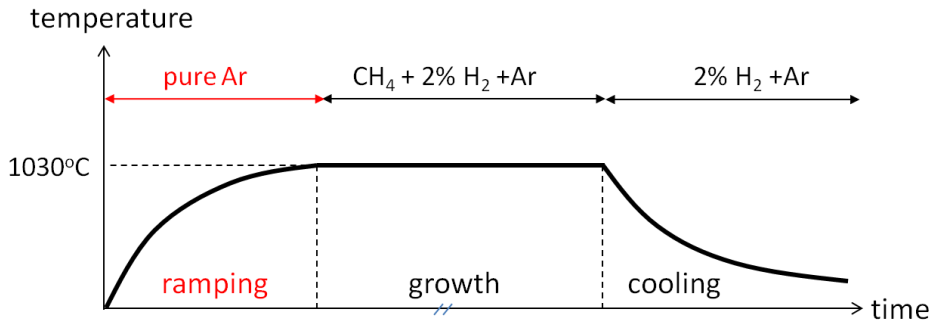

Figure 4.9: Schematic procedure for the improved APCVD. The electro-polished Cu is heated up in the pure Ar.

Besides from modifying the chemical states of the Cu surface, the non-reductive annealing is also found to influence the Cu surface morphology. The original Cu surface, which is relatively smooth as shown in Figure 4.10(a), turns to be partly embedded with the micrometre-sized protrusions after thermal annealing in the pure Ar (see Figure 4.10(b)). These should be the thermally formed CuO_x micro-crystals. This is only a mild oxidation since a short exposure to the diluted H_2 quickly reduces the CuO_x grains as shown in Figure 4.10(c). The Cu surface shown in Figure 4.10(c), which is first heated in Ar and subsequently reduced in H_2, appears more smooth than the pristine surface (Figure 4.10(a)). However, it is worth noting that the post-oxidation H_2

exposure can not completely remove the surface oxygen species. Hao *et al*[62] has confirmed this by investigating the ^{18}O concentration after H_2 reduction using the Time-of-Flight Secondary Ion Mass Spectrometry (TOF-SIMS). This can well explain the seeming paradox that the non-reductive annealing can still suppress the graphene nucleation density even if the Cu surface is exposed to H_2 during the subsequent growth stage.

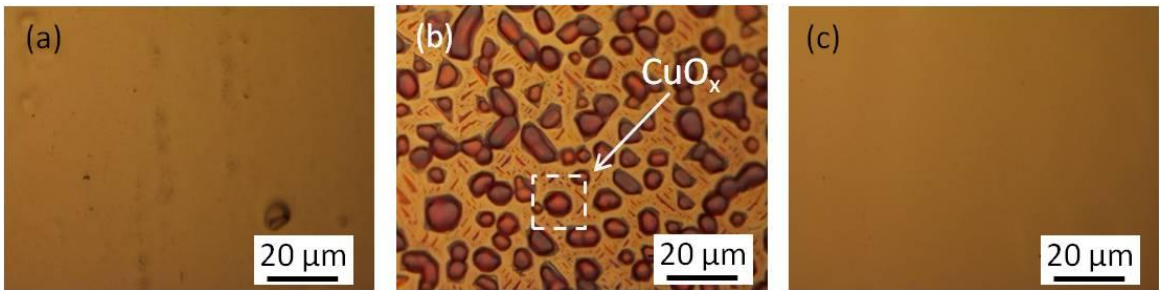

Figure 4.10: OM images of the surface of the electro-polished Cu foil (a) before thermal annealing, (b) after heating up in Ar and immediately cooling down in Ar, (c) after heating up in Ar and short exposure to H_2 + Ar followed by cooling down in H_2 + Ar.

4.2.3 Optimization of CVD Gas Composition

In addition to the electro-polishing and non-reductive annealing of the Cu catalyst, the CVD gas composition, particularly the concentration of H_2 and CH_4, also needs to be optimized towards even larger domains. Figure 4.11(a) shows the correlation between the graphene nucleation density and the H_2 concentration. The nucleation density increases slowly with the decrease of the H_2 concentration from 4% to 2%. However, the density increases about 2 orders of magnitude when decreasing H_2 from 2% to 1%. Since more concentrated H_2 causes larger risk of H_2 explosion, there is a trade-off between the large domain size and the H_2 safety. A H_2 concentration of 2% is finally chosen as the optimal point for the purposes of both suppressing the nucleation density and ensuring the process safety. As the LEL of H_2 is 4%, the use of 2% H_2 can also avoid the marginal safety uncertainties. With the H_2 concentration fixed at 2%, decreasing the CH_4 concentration is found able to tune the nucleation density as shown in Figure 4.11(b). The dependence is roughly linear, suggesting the efficiency of the CH_4 concentration as a control parameter. 75 ppm CH_4 is then chosen as the optimal concentration. It can yield continuous graphene film with millimetre-sized domains in 80 min growth time. Although even lower CH_4 concentrations can potentially achieve larger domains, it takes much longer time to reach full coverage, which is economically undesirable for the mass production.

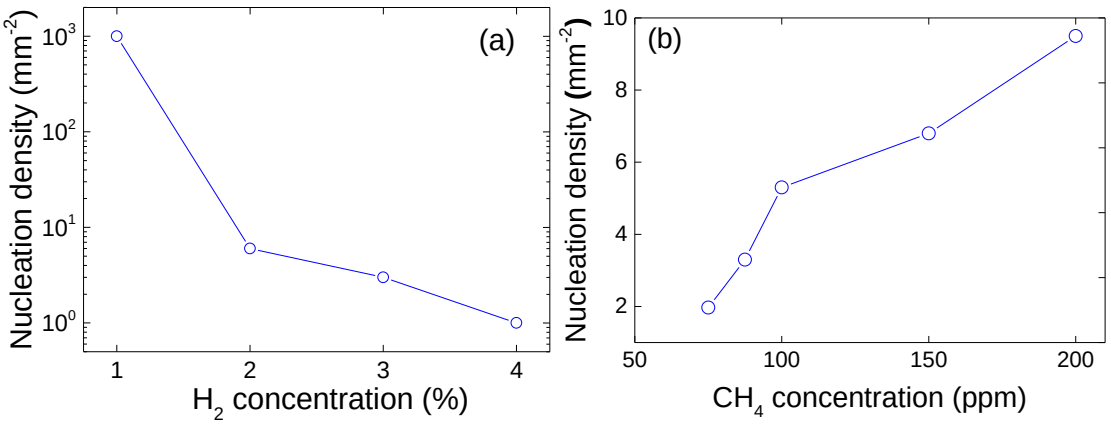

Figure 4.11: Dependence of the graphene nucleation density on the concentration of (a) H_2 with CH_4 fixed 100 ppm and (b) CH_4 with H_2 fixed at 2%. Growth temperature is 1030 ℃ for both series. Graphene is grown on the electro-polished Cu foils following the Ar annealing.

4.3 Characterizations of the Cu-CVD Graphene

Figure 4.12(a) and (b) show the OM images of the graphene grown on Cu, using the previously established optimal conditions, for 60 and 80 min, respectively. The post-growth graphene/Cu samples are baked at 200°C for 1 min in air on a hot plate to oxidize the Cu areas that are not covered by graphene. The resulted colour contrast between the graphene-covered area and the graphene-free area can visualize the individual domains.[237] The graphene grown for 60 min partly covers the Cu substrate with ~70% coverage. The diagonals of some isolated domains, measured from the OM images of the baked samples, reach as large as ~1.5 mm (Figure 4.12(a)). For 80 min growth, the baked sample shows no colour change and hence there is no observable colour contrast (Figure 4.12(b)), suggesting that the Cu surface has been fully covered and protected by graphene from oxidation. To maintain homogenous performance in large scale, the industry-level production should be more concerned with the average domain size than with the maximum size of a few domains. Therefore the entire size distributions have been investigated and the results are summarized in the histogram of Figure 4.12(c). Clearly the majority of the domain sizes are within the neighbourhood of some peak values. Both the centre and the width of the domain size distribution increase with the growth time; the average sizes are 0.4 and 0.8 mm for 50 and 60 min, respectively. Figure 4.12(d) shows the time evolution of the average domain size and coverage. It is worth noting that the average domain size at full coverage (80 min) has reached ~1.0 mm. The coverage follows a typical S-shaped growth curve, featuring an

incubation period during 0-40 min, a linear growth period during 50-60 min, and a slowing down period during 70-80 min.

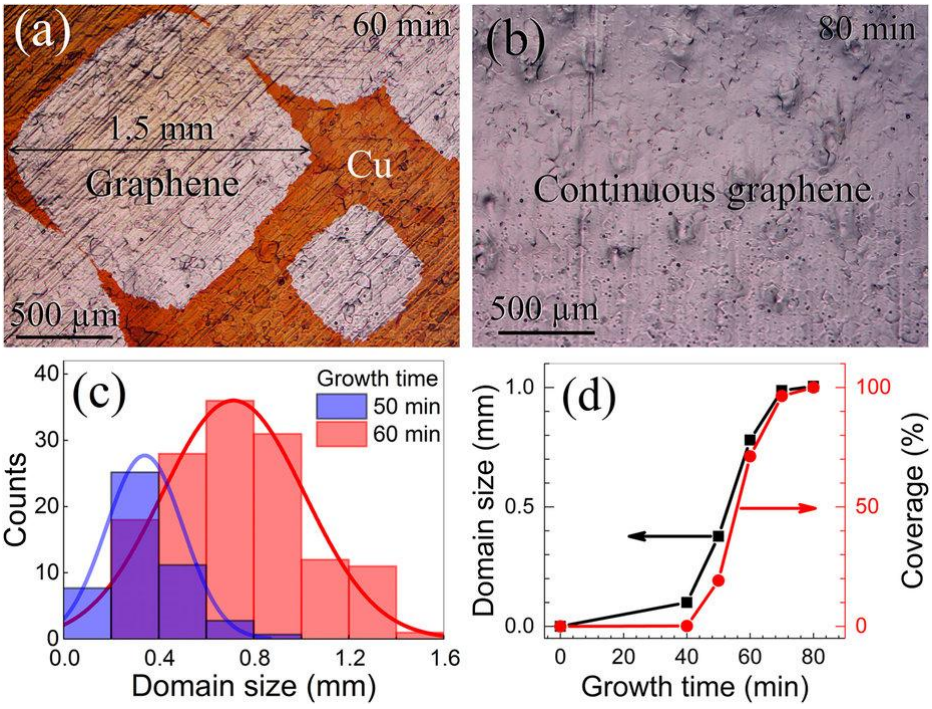

Figure 4.12: Characterization of graphene coverage and domain size. (a) and (b) OM images of the graphene grown on Cu for 60 min and 80 min, respectively. Growth conditions: 1030°C, 3,920 sccm Ar, 80 sccm H_2 (2%), 0.30 sccm CH_4 (75 ppm). (c) Histograms of the domain size for 50 min and 60 min growth. (d) The time evolutions of the graphene coverage and the average domain size.

Compared to the published results on the continuous graphene (indicated by the square markers in Figure 4.13),[54,61,221,222] the average domain size (~1 mm) in this work is at least three times larger than the previously achieved. As the areal density of the domain boundaries is inversely proportional to the average domain area, this suggests the domain boundary density of the graphene films is at least an order of magnitude lower than the previously obtained. Although the domain size in this work is not as large as those centimetre-scale single crystals (indicated by the circles in Figure 4.13), the full coverage of our graphene makes it much more attractive for large scale production. In addition, the concentration of H_2 is controlled not to exceed 2% throughout the whole process, which is much lower than those used in the growth of large single crystals.[62,80]

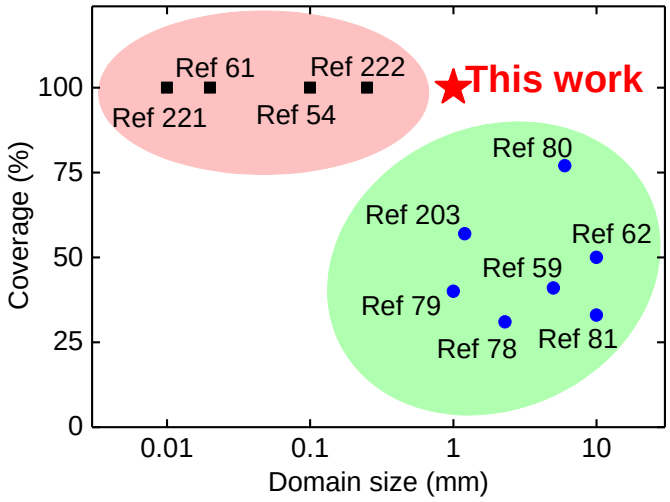

Figure 4.13: A summary of graphene coverage versus domain size. Squares: full coverage with limited domain sizes (≤300 μm). Circles: large domain sizes (1-10 mm) with limited coverage. Star: results obtained from this work.

The quality of the optimally synthesized graphene has been characterized by SEM, OM, Raman spectroscopy, TEM, and charge carrier mobility measurements. The SEM image in Figure 4.14(a) shows the graphene film grown on Cu is continuous and homogenously monolayer over as large as ~1 mm scale. The magnified SEM image in Figure 4.14(b) shows the sample surface is clean and almost free of the contaminating particulates that are frequently seen on the graphene grown on the non-polished Cu surface. The OM image of the graphene transferred onto a 300 nm SiO_2-coated Si substrate in Figure 4.15(a) confirms the film uniformity is preserved after transfer. Figure 4.15(b) shows the typical Raman spectrum measured from the transferred graphene. It has an intense 2*D* peak at 2682 cm^{-1}, a *G* peak at 1592 cm^{-1} and no detectable *D* peak. The intensity ratio of the 2*D* peak to the *G* peak (I_{2D}/I_G) is ~2. The 2*D* peak is of Lorentzian shape with one single component and the full width at half maximum (FWHM) is ~26 cm^{-1}. These spectroscopic characteristics are the fingerprints of high quality monolayer graphene.[123]

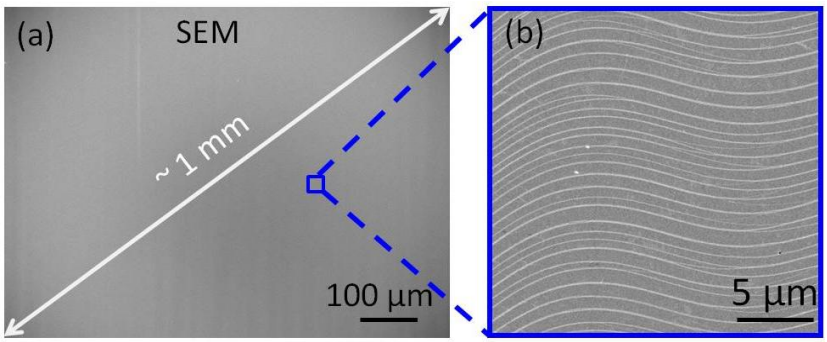

Figure 4.14: (a) Low magnification SEM image of the graphene/Cu sample over a millimetre-scale range. (b) Zoomed in SEM image of the area outlined in the blue box from (a).

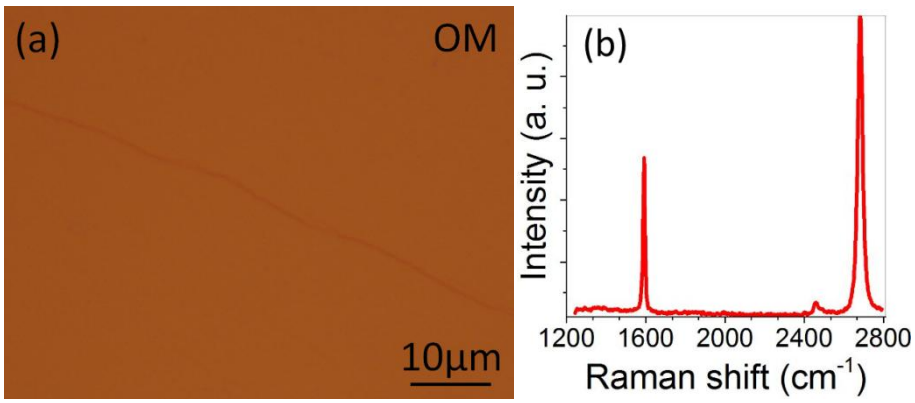

Figure 4.15: (a) OM image of the monolayer graphene transferred onto the SiO_2/Si substrate. (b) Typical Raman spectrum of the transferred graphene. Characterization with the Raman spectroscopy was conducted by Dr. Lorenzo D'Arsiè.

To further confirm the homogeneity of the continuous graphene film, the micro-Raman mapping has been conducted on the transferred graphene over a ~40×40 µm^2 area.[188] The spatially averaged I_{2D}/I_G, I_D/I_G, and FWHM of the 2*D* peak is 2.3±0.2 (mean ± standard deviation, Figure 4.16(a)), 0.04±0.02 (Figure 4.16(b)), and 25±2 cm^{-1} (Figure 4.16(c)), respectively. The mapping results evidence the spatial uniformity, high quality, and monolayer nature of the graphene.

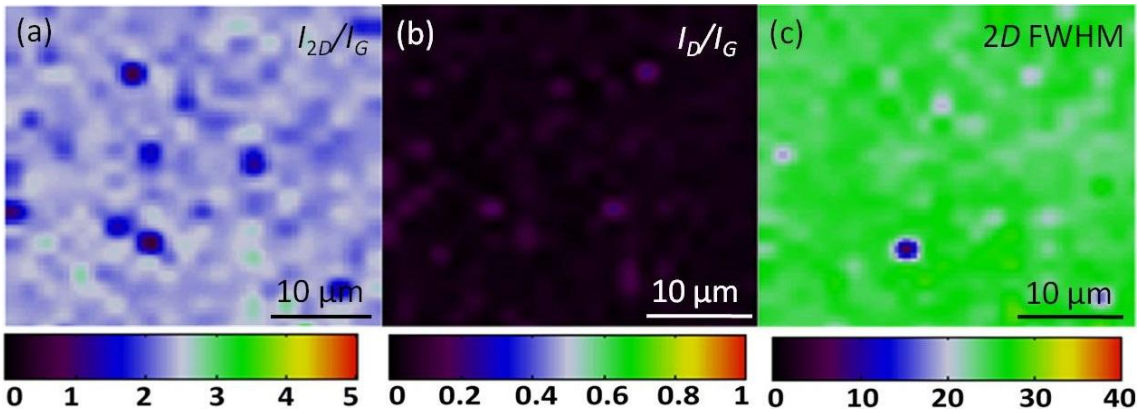

Figure 4.16. Raman mapping of (a) the 2*D* to *G* peak intensity ratio, (b) the *D* to *G* peak intensity ratio and (c) the 2*D* FWHM over a 40×40 μm^2 area. The unit for the colour bar in (c) is cm^{-1}. The Raman mapping experiment was conducted by Dr. Lorenzo D'Arsiè.

The crystalline structure of the CVD graphene is characterized by the selective area electron diffraction (SAED) study with the TEM.[186] Figure 4.17(a) shows a typical SEM image of the graphene transferred onto a micro-Cu TEM grid. As the graphene is largely suspended on the fragile grid, the film deformation during transfer could induce a few small cracks (see Figure 4.17(a)). Twenty positions are then selected for the SAED study. Figure 4.17(b) shows one of the typical electron diffraction patterns, featuring a six-fold symmetry that is characteristic of graphene. Figure 4.17(c) shows the intensity ratio of the outer diffraction spots (labelled as 1 and 4) over the inner spots (labelled as 2 and 3) is close to 0.5, confirming the monolayer nature. The diffraction patterns obtained in other positions show similar features, strongly confirming the spatial homogeneity of the graphene.

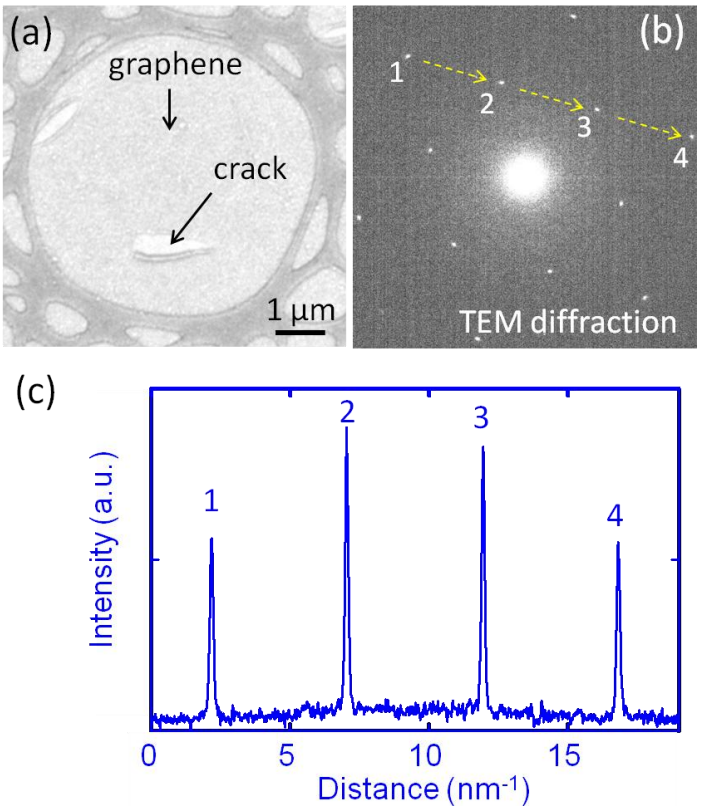

Figure 4.17: SAED study of the CVD graphene. (a) SEM image of the graphene transferred onto the TEM grid. (b) Typical TEM diffraction pattern. The yellow dashed arrows mark four diffraction spots also labelled as 1, 2, 3, and 4. (c) Profile plots of the diffraction spot intensities along the yellow dashed arrows in (b). The TEM characterization was conducted by Dr. Alex W Robertson.

The charge carrier mobility of the continuous graphene film is measured using the Hall effect (see Figure 4.18(a)).[238] The hole mobility derived out of the Drude model reaches 5,500±200 $cm^2V^{-1}s^{-1}$ (mean ± standard deviation) in ambient conditions and the carrier concentration is ~1.6×10^{12} cm^{-2}.[238] As a reference we have also measured a graphene sample grown by the typical LPCVD using H_2 annealing as well as a commercial graphene sample (purchased from Graphenea). The mobility and concentration of the charge carriers of the reference samples are (4,100 $cm^2V^{-1}s^{-1}$, 1.6×10^{12} cm^{-2}) and (3,400 $cm^2V^{-1}s^{-1}$, 9.0×10^{11} cm^{-2}), respectively. Compared to the reference samples as well as the reported values for continuous monolayer graphene summarized in Figure 4.18(b), the mobility of our graphene is notably higher than all the other results using similarly low concentrations of H_2 (0-6%).[81,221,223,225–232] The high mobility combined with the intrinsically safe CVD conditions makes our method particularly suitable for the large scale production of the 'electronic-grade' graphene films. In addition, the sample size in our mobility measurement (50×50 μm^2) is significantly larger than the typical device sizes reported(~10×10 μm^2).[238] The high

mobility over such a large area further demonstrates the high quality and the spatial uniformity of the graphene synthesized using the optimized Cu-CVD method.

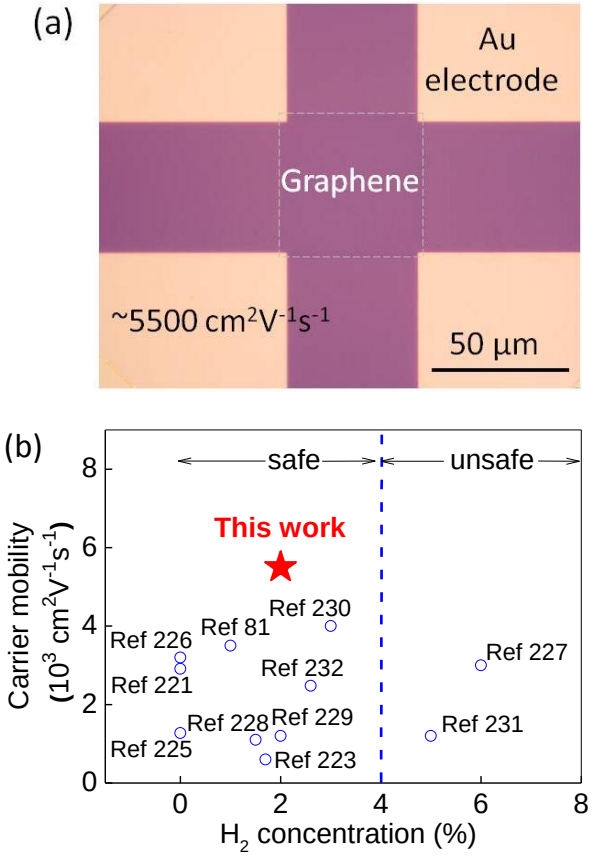

Figure 4.18:. (a) Schematic for the Hall device of the Van der Pauw geometry used for mobility measurement in this work. It primarily consists of the Au electrodes and the square-shaped monolayer graphene. Typical hole mobility reaches ~5,500 $cm^2V^{-1}s^{-1}$. (b) A summary of the charge carrier mobility versus the highest H_2 concentration used during the synthesis processes. Circles: literature work. Star: this work. Dashed line marks the LEL of H_2 (4%). The mobility measurement was conducted by Dr. Lorenzo D'Arsiè.

4.4 Conclusion

With both appropriate pre-treatment of the Cu catalyst and optimization of the CH_4 supply, this research shows that it is possible to grow continuous films of monolayer graphene with millimetre-scale domains by CVD. The low concentration of the flammable gases as well as the relatively short growth time paves a competitive pathway towards safe and economic production of graphene in large scale. For the first time the average domain size of the continuous graphene films has reached millimetre scale. This is achieved mostly by the combinational use of the optimized electro-

polishing, non-reductive annealing and dedicated gas composition tuning. The high quality, spatial uniformity, and low density of domain boundaries are demonstrated by the SEM, Raman mapping, electron diffraction study, and charge carrier mobility measurements. This work helps prepare the current Cu-CVD technology for use in industry level production of graphene.

5 NON-DESTRUCTIVE OPTICAL VISUALISATION OF GRAPHENE DOMAINS AND BOUNDARIES

Part of the results of this chapter have been published in:

Nondestructive Optical Visualization of Graphene Domains and Boundaries Xingyi Wu, Guofang Zhong, and John Robertson. *Nanoscale*, 8, 16427 (2016)

5.1 Introduction

Large area, high quality, continuous monolayer graphene films are indispensable matrix for industrial manufacture of graphene-based high-end devices.[1,2,239] Cu-CVD is particularly promising for mass production of graphene.[60] However, continuous graphene films grown by Cu-CVD are always polycrystalline.[74,75] The boundaries unavoidably emerge from the coalescence of nearby graphene domains.[53] (Hereafter, "grain" and "domain" are used for polycrystalline Cu metal and graphene films, respectively.) The boundaries influence the transporting properties of graphene and consequently alter the performances of graphene-based devices,[35,76,77] which further causes detrimental inhomogeneity to the entire manufactured device arrays. Recently, progresses have been made to drastically reduce the density of boundaries by increasing the domain sizes via modified Cu-CVD technologies.[59,62,78,79] The largest domains at present have reached centimetre scale.[62] On the other hand, the boundary-associated adverse effects can be efficiently controlled by spatial visualisation of the domains and boundaries. A potential visualisation procedure can mark the boundary-infected devices under the navigation of the mapped domains and boundaries of the post-growth graphene films. The boundary-limited products yield can then be evaluated and the quality reliability determined. In this sense, an effective visualisation method is extraordinarily valuable for manufacture management of CVD graphene-based devices.

The graphene domain boundaries can be detected by atomic resolution microscopes such as TEM[74,75]or STM[165,240] and spectroscopic mappings such as Raman.[188,241] These methods are non-invasive with high accuracy but limited to much smaller scale than industry demanded. In recent years, scalable visualisation approaches have been developed, many of which can be approximately classified into two major types. The first type is to selectively decorate the graphene domain boundaries using specific chemical species, which is feasible due to the relatively high chemical reactivity of the boundaries. The decorated boundaries can be readily distinguished from the rest graphene surfaces by microscopes. Conventionally used decorating groups include oxidants such as radicalized oxygen[83] or permanganate[84] and metals such as gold nanoparticles.[86] The other is to visualise the graphene domains by mapping the graphene orientation-dependent alignment of the 'quasi-epitaxial' coatings. For instance, nematic liquid crystals coated on graphene surfaces assemble along specific directions corresponding to the underlying graphene domain orientations.[85,87] Similar direction correspondence also exists between the graphene-supported MoS_2 flakes grown by

CVD and the underlying graphene.[88] However, these methods are destructive to graphene since they have to either partially damage carbon bonds or induce contaminating coatings or transfer graphene onto secondary substrates. Therefore, a non-destructive and scalable visualisation technique is urgently desired but currently lacking.

In principle, if an ideal visualisation method is to non-destructively map the graphene domains and boundaries, it should preferably detect certain intrinsic characteristics of graphene rather than any derivative physical or chemical effects induced by external interferences. Moreover, the potential 'intrinsic characteristics' should also be spatially specific to individual graphene domains so as to distinguish the geometric locations of the inter-connected domains. Based on this analysis and the latest experimental findings, this work has rationally designed a novel optical method, which, for the first time, can non-destructively visualise the domains and boundaries of large area continuous graphene films grown on the polycrystalline Cu foils (Gr/Cu) by CVD.

5.2 Design of Enhanced Dark Field Optical Microscope

The novel design is inspired by the recent discoveries of the dynamic formation of Cu surface pyramids during the Cu-catalyzed CVD graphene growth as discussed in Section 2.3.7.[175,206,242] The schematic drawing in Figure 5.1(a) further illustrates this process in the case of a hexagonal graphene domain. The graphene-covered Cu surface has evolved into a hexagonal pyramid via the lateral evaporation (Figure 5.1(a)).[206] It is worth noting that, if viewed from the perpendicular direction, the hexagonal pyramid will appear as a star-like ridge set. If the fingerprint ridge sets can be visualised in some way, the spatial distribution of the graphene domains and boundaries can be straightforward determined. Since the ridges are the intrinsic features of the graphene-Cu interfacial morphology, the potential visualisation process could be non-destructive.

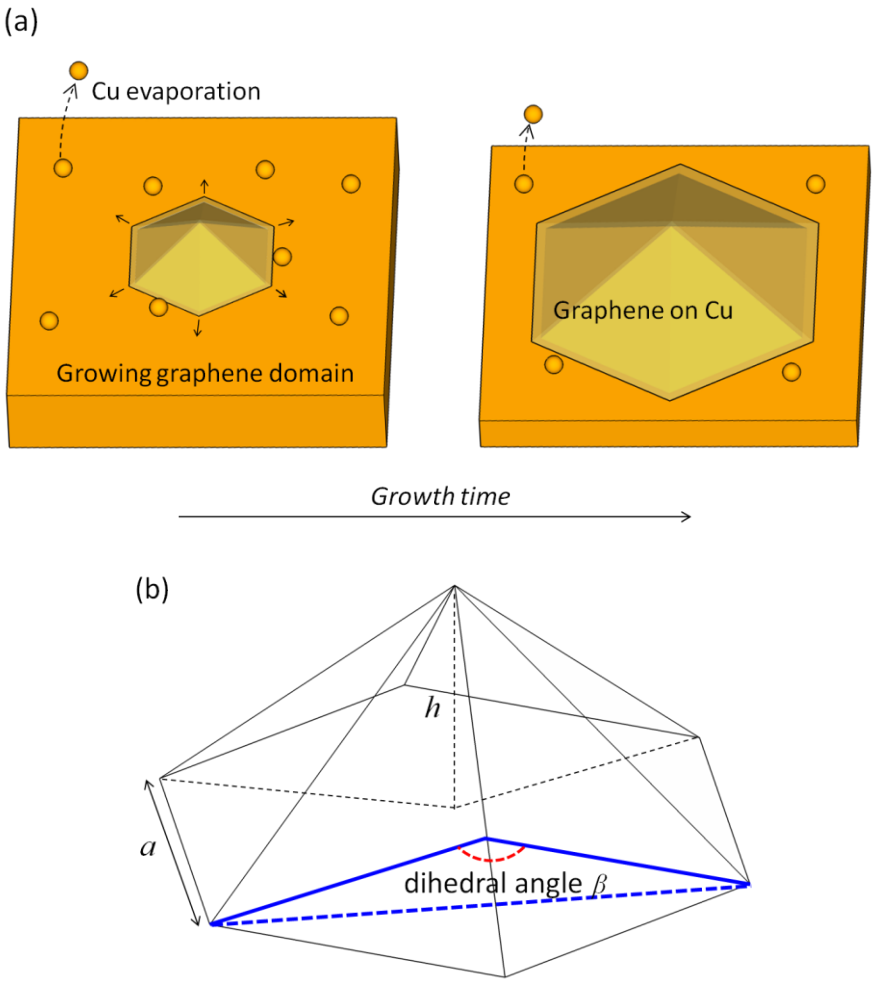

Figure 5.1: (a) Schematic illustration of the formation of a Cu surface pyramid under the template effect of an enlarging graphene domain due to the different evaporation rates of the graphene-covered Cu and graphene-free Cu. (b) Sketch of the hexagonal pyramid for calculation of the dihedral angle, where *h* is the height of the pyramid and *a* is the lateral length.

This research demonstrates that the star-like ridge sets of Gr/Cu can be clearly imaged by a modified optical microscope (OM) under an enhanced dark field mode (EDF). Figure 2(a) shows the setup of the EDF-OM which is modified from an upright OM. An external illumination light source is used, such as an annular tube or a desk lamp, instead of its original internal light source, as respectively shown in Figure 2(a) and Figure 2(b).

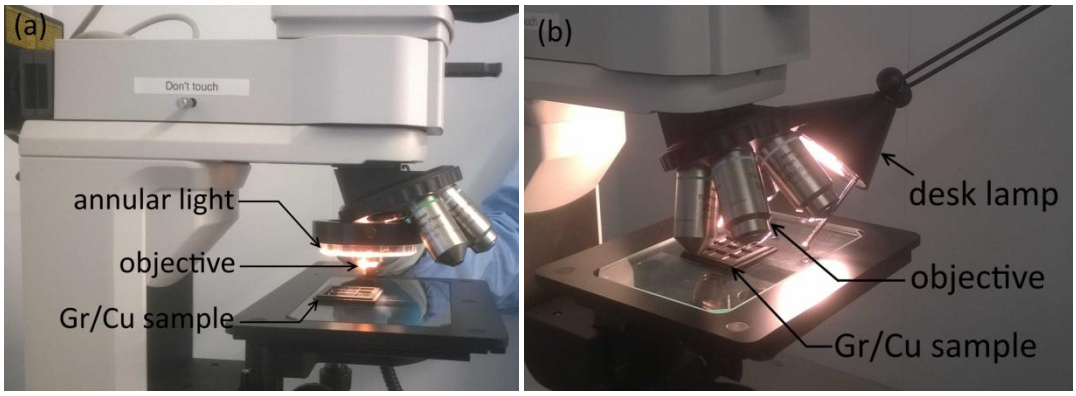

Figure 5.2: Setup of the EDF-OM using (a) an external annular light source or alternatively (b) a desk lamp instead of its original internal light source.

The EDF-OM is then used to image the discontinuous graphene samples which have been grown on commercial polycrystalline Cu foils via CH_4 decomposition using an APCVD recipe established in the previous chapters. Figure 5.3 (a) shows one of the EDF-OM images of the isolated hexagonal graphene domains. A star-like ridge set is clearly revealed which radially diverges from the domain centre to the domain vertices. The entire structure is morphologically identical to the schematic in Figure 5.1(a), i.e., each set of ridges exactly follows the diagonals of each graphene domain since the Cu surface pyramid inherits the geometric symmetry of the domain. Such one to one correspondence, as will be shown, thereby enables non-destructive visualisation of the domains and boundaries of continuous graphene. In addition, feather-like features along some of the ridges are also observed, which make the entire domain much brighter than the surrounding Cu background.

Since the as-grown Gr/Cu sample is invisible under the bright-field OM (BF-OM), the sample is mildly oxidized in air to enable the BF-OM observation of the isolated domain.[237] Figure 5.3(b) displays a BF-OM image of the same domain obtained after mild oxidation. It only shows homogenous optical contrast inside the domain, providing no clues for any star-like ridges. The enormous difference between the EDF-OM and BF-OM observations originates from their different optical configurations. The external light source of the EDF-OM provides large-angle oblique incident light (~50° relative to the sample plane, see Figure 5.4(a)), while the internal BF light source gives almost vertical incident light with a much smaller incident angle (Figure 5.4(b)). Under the EDF-OM, most of the oblique incident light from the external source will be specularly reflected away from the objective by any smooth surfaces. However, as the star-like ridges experience significant curvature changes between adjacent pyramid faces, they

are much rougher than the faces and thereby could scatter much more light into the objective (see Figure 5.4(a)). Therefore, the ridges are visualised as star-like bright line sets. In contrast, under the BF-OM, most of the vertical internal incident light will be reflected back into the objective, which causes no visible contrast between the ridges and the faces (see Figure 5.4(b)). We find that a pristine DF-OM using the hollow cone-shaped internal light can also visualise the star-like ridges, but the resulted contrast is too low and the brightness too weak, which might account for its neglect in previous research.[243] This is probably because of the small incident angle and the weak intensity of the internal DF light. Indeed the novel setup in this research is named as the EDF-OM because of the external source-enhanced incident angle and light intensity.

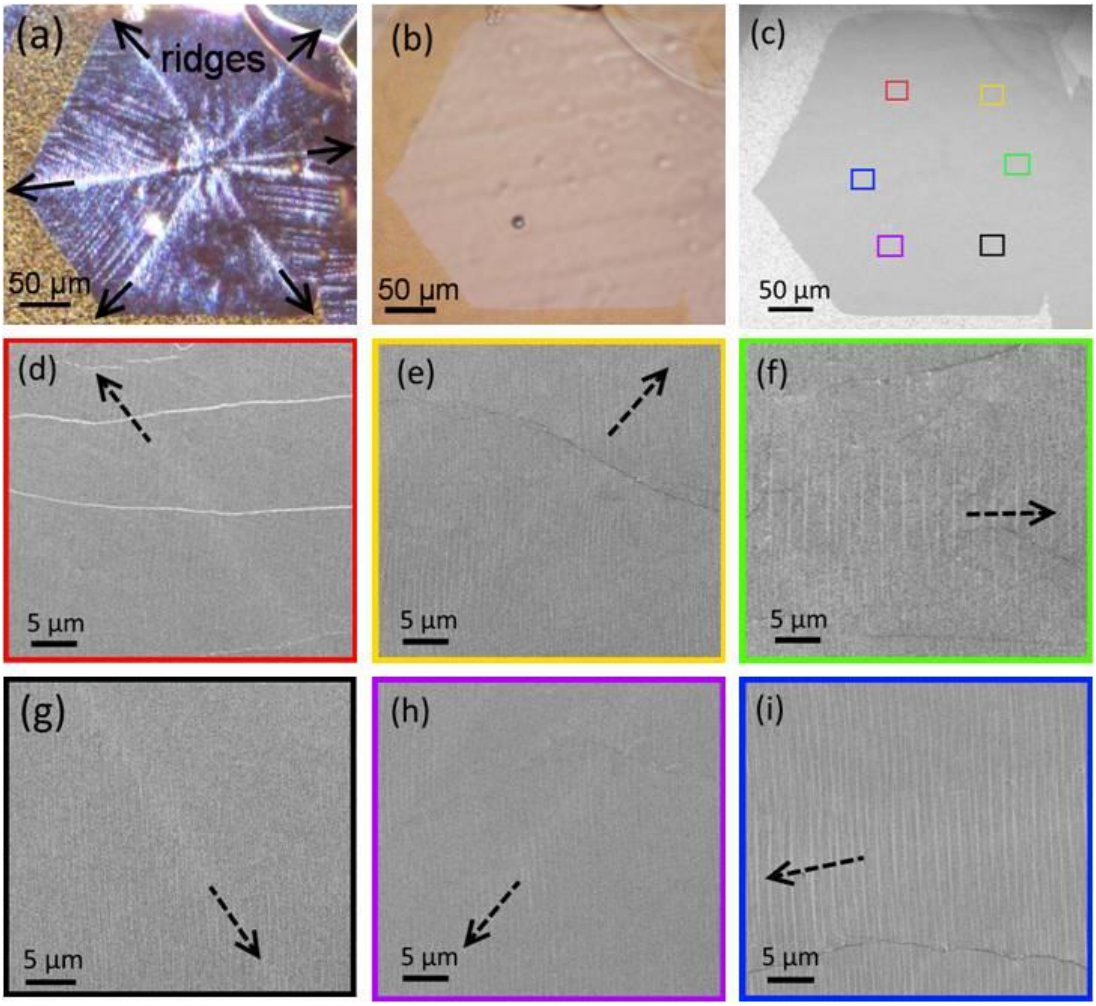

Figure 5.3: (a) EDF-OM, (b) BF-OM and (c) SEM images of the same isolated hexagonal graphene domain grown on Cu. The Gr/Cu sample has been mildly oxidized for BF-OM observation. The star-like ridge set is observable only by the EDF-OM. (d)-(i) High magnification SEM images of the midpoints of the domain diagonals clearly demonstrating the existence of six ridges. Their outline colours are set corresponding to the coloured boxes marked inside (c). The black dashed arrows mark the locations and orientations of the ridges.

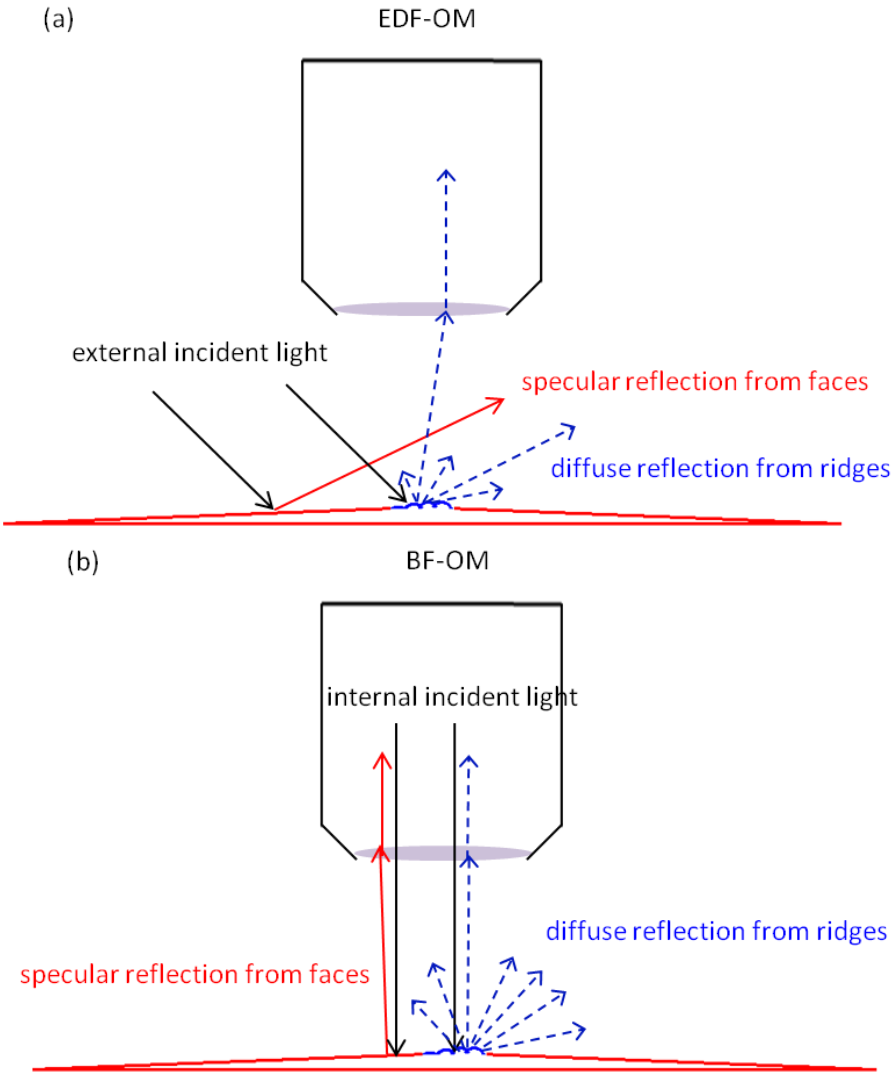

Figure 5.4: Schematic of the optical configurations of the (a) EDF-OM and (b) BF-OM.

Similar to the BF-OM, the low magnification SEM image of the same domain (Figure 5.3(c)) barely shows any ridge-like features. This agrees with previous SEM investigations reporting homogeneous optical contrast inside the Cu-CVD graphene domains.[53] However, close observations under high magnifications along the domain diagonals indicate the existence of the star-like ridges, as shown in Figure 5.3(d)-(i), which appear slightly brighter than the surrounding domain background. This thereby supports the EDF-OM discovery of the star-like ridge set. It should be noted that this is the first time that such a ridge structure is formally manifested by SEM. However, although SEM can capture an intrinsically identical ridge structure as the EDF-OM, it only generates much lower contrast than the EDF-OM. Thereby the EDF-OM is much

more advantageous than the high magnification SEM in imaging the graphene ridge structures for visualisation of large scale graphene domains and boundaries.

5.3 Enhanced Dark Field Optical Microscope Images of Graphene-Cu Interfacial Ridge Structures

In addition to the well-defined star-like six-ridge structure shown above, this research has further discovered, for the first time, a plethora of novel star-like ridge sets which do not always exhibit six ridges, as summarized in Figure 5.5(a)-(l). These structures differ from each other. Most remarkably, the structures in Figure 5.5(a)-(j) have visible ridges while those in Figure 5.5(k) and (l) have no observable ridges at all.

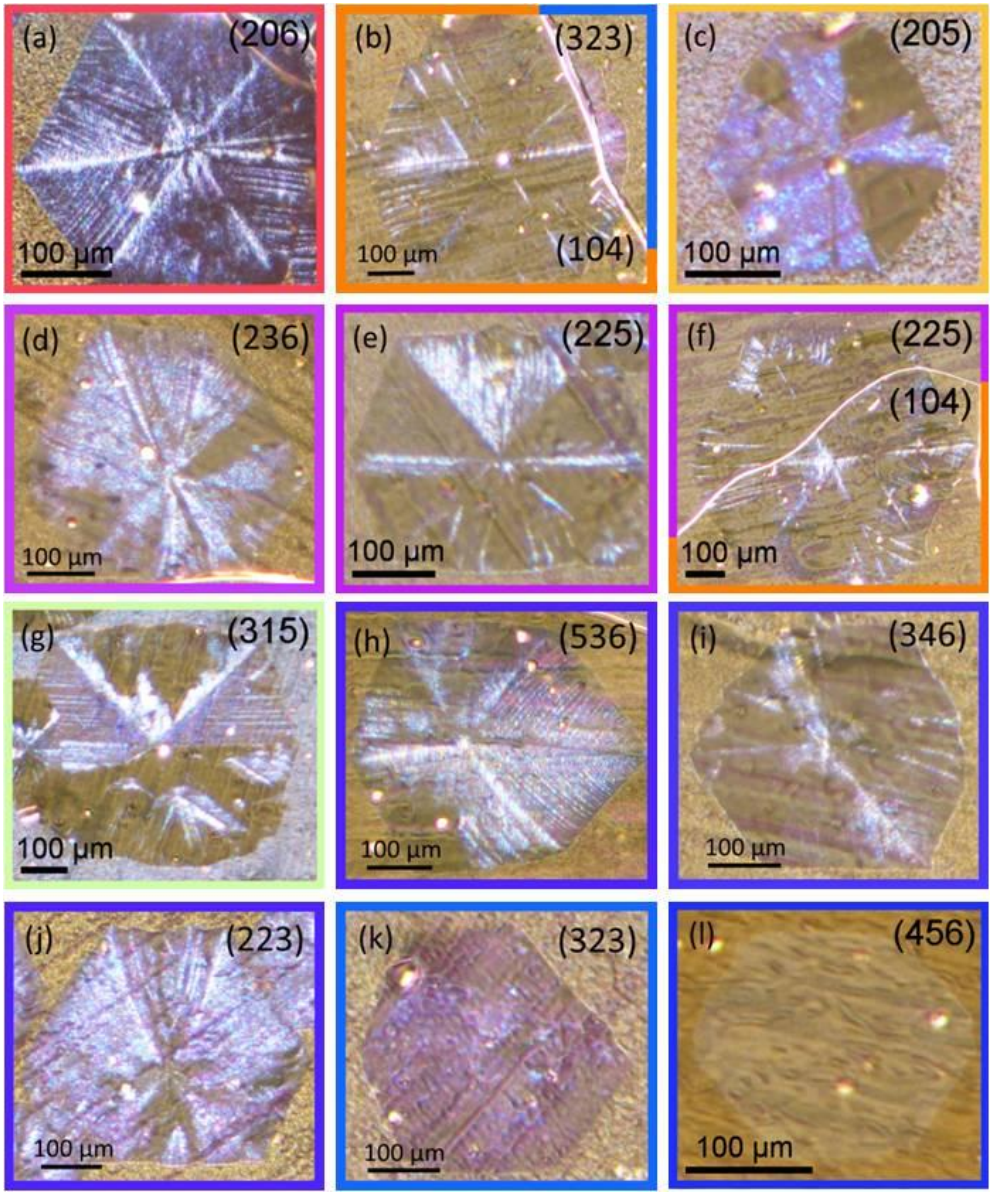

Figure 5.5: (a)-(l) EDF-OM images of multi-types of star-like ridges with the EBSD-determined Miller indexes of the underlying Cu grains marked inside each panel. The outline colours are set equal to the corresponding EBSD mapping colours of the respective Cu surfaces. The mix-coloured outlines of (b) and (f) indicate the presence of two different Cu grains below the same graphene domain.

Further investigations find that the morphologies of the various star-like ridge sets are governed by the underlying Cu crystallographic orientations. Figure 5.6(a) shows an EDF-OM image of multiple types of star-like ridge sets formed on a polycrystalline Cu region. Figure 5.6(b) shows the crystallographic orientation map of the underlying Cu grains identified by EBSD. The Miller indexes of the Cu grains are marked inside Figure 5.5(a)-(l) and also illustrated by their outline colours with reference to the colour key inset in Figure 5.6(b). Obviously different types of star-like ridge sets are formed on different Cu grains while those on the same Cu grain are of exactly the same type. In

particular, one graphene domain grown over multiple Cu grains, as seen in Figure 5.5(b) and 5(f), has mixed types of ridges in accordance with the crystallographic orientations of the respective Cu grains. It should be noted that this is the first time that such diverse Cu crystallographic orientation-dependent star-like ridge sets are discovered, although there has been extensive research on the polycrystalline Cu-catalyzed graphene growth and its characterisation.[244] This is most likely because their morphological differences can be hardly observed under the commonly used BF-OM and SEM. Although the three dimensional laser microscope has found a ridge structure similar to in Figure 5.5(a),[242] no other types of the star-like ridge sets have been reported. The various star-like ridge structures thereby raise new phenomenon for fundamental graphene research beyond the current scope.

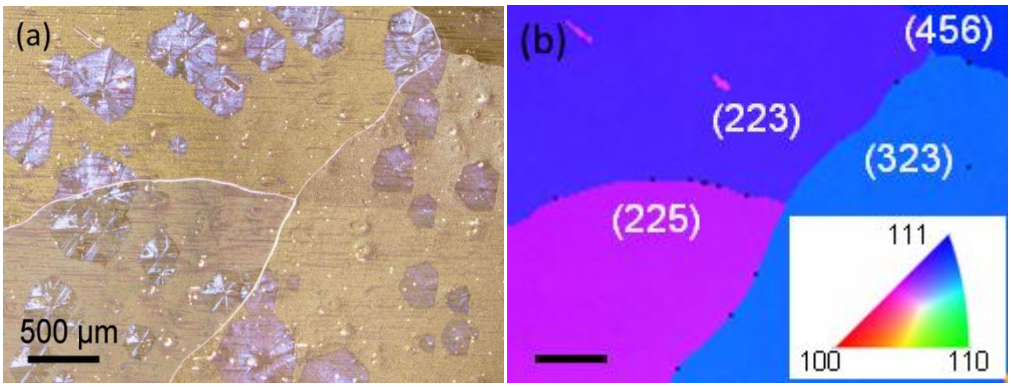

Figure 5.6: (a) EDF-OM image of the graphene domains with multi-types of star-like ridges grown over a polycrystalline Cu region. (b) Surface normal-projected inverse pole figure EBSD map of the same region as in (a) with the colour key inset. The sample is tilted at 70° for EBSD scanning and the determined Miller indexes are marked inside each Cu grain. The EBSD measurement was conducted by Dr. Guofang Zhong.

As the visibility of the ridge structure is determined by the curvature change between the adjacent pyramid faces, smaller dihedral angle β (Figure 5.1(b)) should enhance the ridge visibility. For simplicity, considering the case of a hexagonal Cu pyramid as illustrated in Figure 5.1(b), β can be calculated as:

$$\sin\frac{\beta}{2}=\sqrt{\frac{1+\left(\frac{h}{a}\right)^2}{1+\frac{4}{3}\cdot\left(\frac{h}{a}\right)^2}}\approx 1-\frac{1}{6}\cdot\left(\frac{h}{a}\right)^2,(h<<a) \qquad (5.1)$$

where h is the height of the pyramid and a is the lateral length of the hexagonal graphene domain. Assuming the lateral growth rate of graphene, γ_{gr}, and the

evaporation rate of the graphene-free Cu, γ_{Cu}, are both constant, equation (1) can be approximated by:

$$\sin\frac{\beta}{2} \approx 1-\frac{1}{6}\cdot\left(\frac{\gamma_{Cu}}{\gamma_{gr}}\right)^2. \qquad (5.2)$$

Here, γ_{Cu} depends on the CVD processing temperature T, the standard vapour pressure of Cu P_{Cu} and total ambient pressure P,[245] while γ_{gr} can be taken proportional to the partial pressure of hydrocarbon gas P_{C} in a first-order reaction:

$$\gamma_{Cu} = \frac{P_{Cu}-P}{\sqrt{2\pi MRT}}, \qquad (5.3)$$

$$\gamma_{gr} = k\cdot P_C, \qquad (5.4)$$

where M is the molecular weight of Cu, R is the universal gas constant, and k is the first-order graphene growth rate constant. Equations 5.2, 5.3, and 5.4 relate the ridge visibility to the CVD process parameters. The conditions using high processing temperature (~1000 °C) and low hydrocarbon concentration for synthesis of high quality graphene favour the formation of observable ridge structures.[161,163] Considering that atmospheric pressure is used for CVD of graphene in this research, graphene grown by the more widely used LPCVD (~1Torr) should have more pronounced ridges due to faster Cu evaporation.[161]

In addition, it should be noted that the visibility of the ridge structures is also influenced by the crystallographic orientations of the Cu grains as previously shown in Figure 5.5. During the CVD process, the high temperature annealing promotes formation of large Cu grains with low-energy crystallographic facets, mostly (110), (100) and (111) (The absence of these exact low-index facets from our EBSD results is probably due to the deformation of the Cu foils during sample handling). It has been well established that the thermal stability of the low-index fcc metal surfaces follows their in-plane packing density. Generally the relatively open (110) and (100) surfaces start to disorder and pre-melt at temperature below T_{m} while the most densely packed (111) surface keeps in a crystalline state up to T_{m} and shows weak superheating effects.[246,247] This can qualitatively explain our observations in Figure 5.5. Since a lower stability results in a higher evaporation rate of Cu, the visibility of the ridge structures under EDF-OM varies on different Cu crystallographic surfaces. As the (111) surface is of the highest stability, the ridge structures can hardly form on (111)-vicinal Cu surfaces

under our CVD conditions, therefore the graphene domains on (111)-vicinal Cu surfaces are barely visible under EDF-OM (see Figure 5.5(k) and (l)). However, most of the graphene domains grown on other Cu grains are more or less visible because of their relatively lower surface stability (see Figure 5.5(a)-(j)).

As for the additional features making parts of the graphene domains brighter, particularly noticeable in Figure 5.5(e) and Figure 5.5(g), their formation probably originates from the reconstruction of the Cu surfaces under the template effect of the graphene domains during both the isothermal growth and cooling processes.[206,248] This is essential since the graphene-covered Cu pyramid faces are usually in higher energy states compared to the low-energy surfaces of the graphene-free Cu grains formed during annealing. The reconstruction will transform the atomic flat pre-melted Cu surfaces into 'step-wise rough' facets,[206] some of which might be rough enough to be visualised by the EDF-OM. The reconstruction also varies depending on the crystallographic properties of the Cu grains.[206,248] It should also be noted that if the graphene growth rate is so high as to rapidly form continuous graphene, or the growth temperature is too low which suppresses the evaporation of Cu, the ridge structures can hardly form on Cu and thereby the graphene domains might be barely visible under the EDF-OM.

5.4 Optical Visualisation of Domain Boundaries of Cu-catalyzed Continuous Graphene

At this point we have confirmed that the star-like ridge structures arise from the intrinsic morphologies of graphene-Cu interfacing and can be clearly imaged by the EDF-OM. We now demonstrate the non-destructive visualisation of the star-like ridge structures of continuous Gr/Cu and its application in outlining the domain boundaries and estimating the domain density. Figure 5.7(a)-(c) show three typical images, taken by EDF-OM, BF-OM and SEM, respectively, of the same continuous Gr/Cu sample. The EDF-OM image in Figure 5.7(a) clearly exhibits multiple sets of star-like ridges. In contrast, the BF-OM and SEM images in Figure 5.7(b) and (c) merely show the Cu surface morphology with a uniform colour contrast. As each set of star-like ridges spatially tags one graphene domain, we can use the ridge intersection to mark the nucleation centre of each domain and the ridge endpoints to delineate the neighbouring domains. Figure 5.7(d) shows the same EDF-OM image as Figure 5.7(a) with individual domains approximately outlined by the yellow polygons based on their corresponding

star-like ridges. The graphene nucleation centres (ridge intersections) are generally deviated away from the geometrical centres of the domains as a consequence of the competitive growth of the neighbouring domains.[206] The domain density in Figure 5.7(d) is counted to be ~5.5 mm^{-2} and thus the average domain size is ~0.18 mm^{-2}. Figure 5.7(e) and (f) further illustrate the EDF-OM images of continuous graphene grown on other Cu grains under the same CVD conditions with their domains outlined by the yellow polygons. It should be noted that the novel optical visualisation approach works only under the EDF-OM mode.

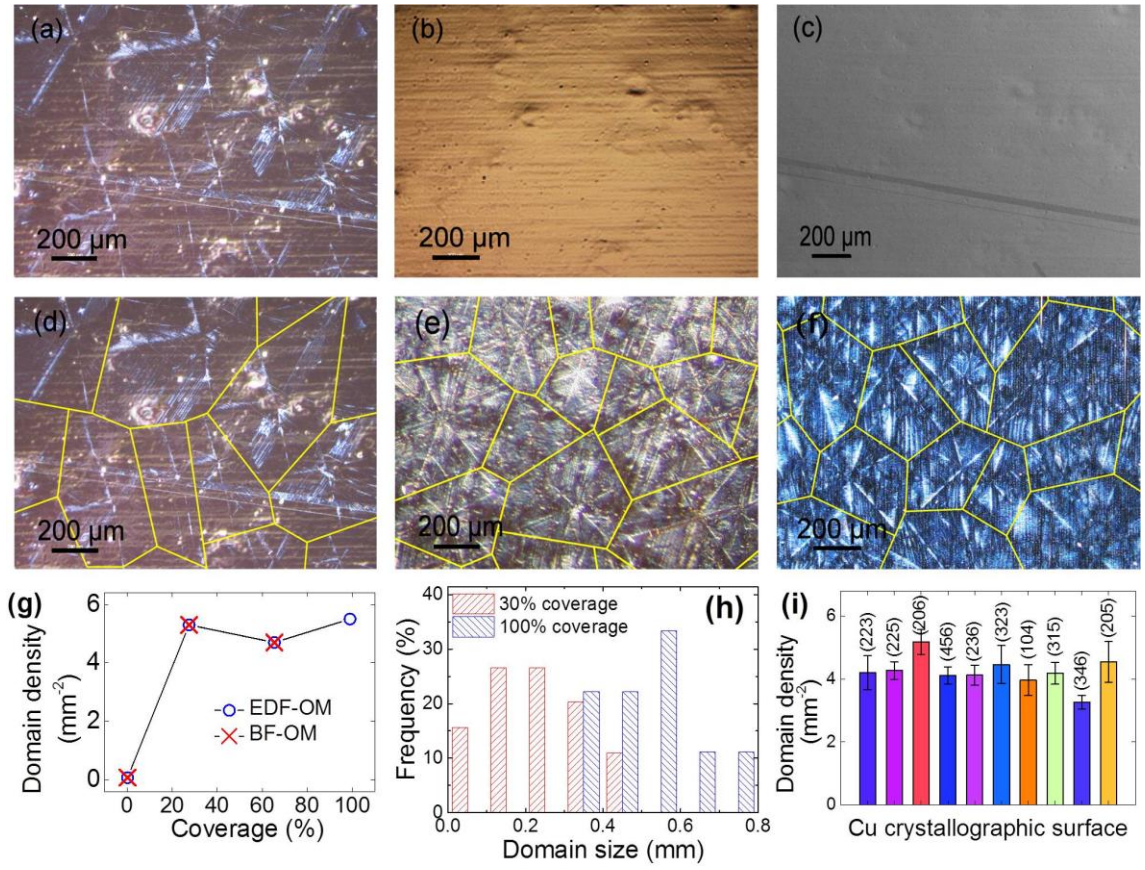

Figure 5.7: (a) EDF-OM, (b) BF-OM and (c) SEM images of a typical continuous Gr/Cu. Only the EDF-OM can visualise the star-like ridge structures that are spatially corresponding to the graphene domains. (d-f) Outlining the inter-connected domains of continuous graphene films by the solid yellow polygons according to the fingerprint star-like ridge structures visualised by the EDF-OM. The solid polygons represent the approximate domain boundaries. The graphene films in (d-f) are obtained from the crystallographically different Cu grains under the same CVD conditions. (g) Graphene domain density against coverage. CVD graphene with different coverage is grown by varying the carbon supply time. (h) Distributions of graphene domain sizes at ~100% coverage (determined by the EDF-OM) and ~30% coverage (determined by both the BF-OM and the EDF-OM). (i) Graphene domain density against Cu crystallographic orientations, which is counted from discontinuous Gr/Cu. The column colours are set equal to the EBSD mapping colours of the respective Cu surfaces (see Figure 5.6)

Since the graphene domain density gradually saturates with increasing coverage during Cu-CVD growth,[71] the reliability of the novel visualisation method can be substantiated by comparing the domain density and size distribution visualised at full coverage to those counted at partial coverage. Figure 5.7(g) plots the graphene domain density against the corresponding coverage. The coverage is measured from both the EDF-OM and BF-OM images, but the Gr/Cu sample is mildly oxidized for the BF-OM observations. The domain density up to ~30% coverage can be counted with high accuracy from the BF-OM image since most domains are spatially isolated. However, the BF-OM method begins to cause noticeable errors after ~60% coverage and completely fails at >80% coverage as an increasing number of domains are becoming inter-connected. In contrast, the EDF-OM approach can figure out the domain density from zero up to full coverage. We can see from Figure 5.7(g) that the domain density at full coverage, which can be visualized only by the EDF-OM, has limited discrepancy (~14%) with the domain density at lower coverage (~30% and ~60%), which can be counted by both the EDF-OM and the BF-OM. Figure 5.7(h) shows that the domain size distribution at full coverage (determined by EDF-OM) is also consistent with that at partial coverage (determined by both EDF-OM and BF-OM). Figure 5.7(i) shows that there is no significant discrimination for the domain densities of the discontinuous graphene counted from the crystallographically different Cu grains. This agrees with the previous results at similar growth temperature.[63] These observations justify that the EDF-OM visualisation method is effective and reliable for continuous graphene films although the ridge structure of the domains grown on (111)-vicinal Cu grains are less visible than the rest.

It is worth noting that the EDF-OM visualisation method has significant advantages over the up-to-date methods. First of all, it is non-destructive since the Gr/Cu samples are observed by an optical microscope with no need for oxidation, assistive coatings or transfer. Moreover, it is scalable, cost-saving, and rapid because an optical microscope can work in ambient conditions by frame-to-frame scan.

5.5 Conclusions

In summary, this work has developed a novel EDF-OM method for spatially visualising the domains and boundaries of large are continuous Gr/Cu. It is based on a variety of novel star-like ridge sets which are formed during CVD growth as inherent morphologies of the graphene-Cu interfaces The ridge structure-enabled visualisation

approach is purely optical and thereby, for the first time, not only completely non-destructive to graphene but also applicable to large area samples. Therefore, this research opens a new route towards non-destructively monitoring and controlling the boundary-associated adverse effects on the graphene-based devices that are manufactured in the industry scale. Furthermore, we find that the morphologies of the various types of ridge sets vary depending on the underlying Cu crystallographic orientations. This is a new phenomenon beyond current knowledge of polycrystalline metal-catalyzed graphene growth. It strongly indicates the complexity of graphene-Cu thermodynamic interactions for which a comprehensive understanding should take into account the thermal stability of the Cu facets.

6 MODELLING OF THE KINETICS OF GRAPHENE NUCLEATION AND GROWTH BY COPPER-CATALYZED CHEMICAL VAPOUR DEPOSITION

6.1 Introduction

Synthesis of graphene by the Cu-CVD method makes it possible to exploit in large scale the extraordinary properties of graphene.[1,2,60,239] Comprehensive knowledge of the Cu-CVD reaction kinetics is fundamentally essential for engineering the synthesis processes and tailoring the product properties. In principle a potential kinetic model should quantify the time-evolutions of the fundamental observables, including the graphene domain area $A(t)$, the nucleation density $N(t)$, and the graphene areal coverage $\Theta(t)$. The model should also be able to explain the experimentally observed graphene CVD phenomenon such as the dependence of graphene formation on temperature and the partial pressure of the forming gas.

Figure 6.1 has illustrated the primary Cu-CVD kinetic steps. Graphene formation starts from the dissociative adsorption of the gaseous carbon precursor (mostly CH_4) on Cu which is then further catalytically dehydrogenated into the reactive hydrocarbon species.[178,182] The adsorbed CH_4 can desorb from the Cu surface depending on the sticking coefficient.[183] Next the hydrocarbons transport to the active surface sites where their local concentration accumulates to a supersaturation level that is sufficient to initiate a nucleation (represented by #1 in Figure 6.1). Some other hydrocarbons diffuse to the edge of an existing nucleus where they are attached to enable the domain growth (represented by #2 in Figure 6.1). The carbon attachment process can be seen as a transformation of the carbon species from the amorphous phase to the crystalline phase. The domain edge atoms could also be etched by the surface H atom and transform back to the unbound hydrocarbon species. So the domains can enlarge only if the attachment rate exceeds the etching (detachment) rate: $k_{att}>k_{growth\_etch}$. The hydrocarbon species can directly desorb from the Cu surface to the gas phase (represented by #3 in Figure 6.1). Since the real graphene formation occurs at high temperature (~1000 ℃), the surface Cu atoms can evaporate (represented by k_{Cu_evap} in Figure 6.1) and hence the atop hydrocarbons might desorb along with the evaporated Cu (#4).

There could be multiple domains on the Cu surfaces surrounding the hydrocarbon species which can join only one of the domains. Since the Cu-catalyzed graphene formation is self-limiting, the neighbouring domains are essentially competing for the limited surface hydrocarbons. This will be referred to as the inter-domain competitions in this thesis. The Cu-CVD of graphene has been confirmed to be mostly surface-mediated.[174] Hence the rate-limiting should be a surface process, which can be either the edge attachment of hydrocarbons, if its characteristic rate (k_{att}) is significantly larger than the characteristic surface diffusion rate (k_{diff}), or the surface diffusion of the hydrocarbons vice versa.[62,72]

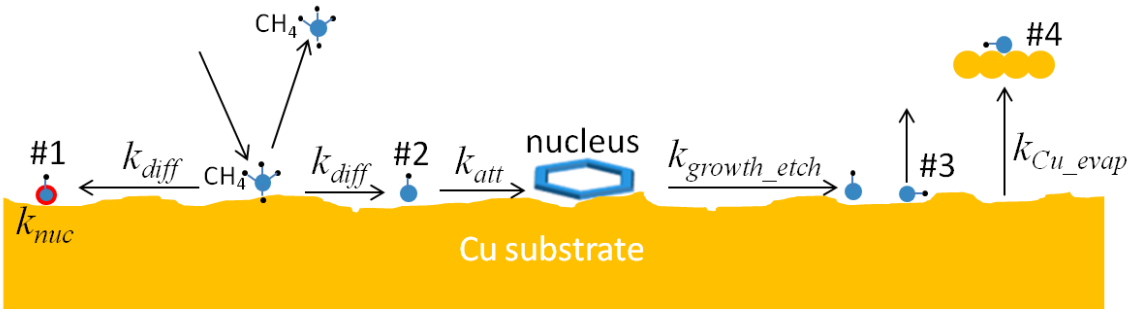

Figure 6.1: Schematic illustration of the Cu-CVD surface processes. The solid blue, black, and orange circles represent the C, H and Cu atom, respectively. k_{nuc}, k_{diff}, k_{att}, k_{growth_etch}, and k_{Cu_evap} represents the nucleation rate, the diffusion rate, the edge-attachment rate, the edge-etching rate, and the Cu evaporation rate, respectively. The hydrocarbon labelled as #1 forms a nucleus by itself. #2 diffuses to join an existing graphene nucleus. #3 desorbs from the Cu surface to the gas phase. #4 is forced to desorb due to the thermal evaporation of the underlying Cu atom clusters. The Cu substrate surface is rough under real thermal CVD conditions partly because of the Cu evaporation.

For a more insightful understanding of the kinetics, a couple of mathematical models have been established to describe the dependence of the graphene domain area $A(t)$ and the areal coverage $\Theta(t)$ on the CVD growth time t. Most of them concentrate on the edge-attachment-controlled regime. For instance, Kim *et al*[182] has derived a hyperbolic tangent time-dependence of the domain radius assuming that the domain area growth rate is proportional to the domain perimeter. Under the framework of Langmuir competitive adsorption, they have further proposed that a reaction equilibrium between adsorption and desorption of carbon has been established before the onset of graphene nucleation and growth.[262, 263] Celebi *et al*[233] has obtained a modified Gomerptz function for $A(t)$ based on the observations of what they claimed to be dispersive growth kinetics. But the exotic dispersive kinetics has not been observed in other research. Xing *et al*[212] has suggested an exponential decay model (increasing form) assuming the graphene coverage growth rate is proportional to the area of the graphene-free Cu. This assumption is qualitatively reasonable considering the self-limiting nature, i.e., the area of the catalytic active Cu surface is decreasing as the graphene coverage increases. Eres *et al*[250] has constructed a modified logistic time-dependence for $\Theta(t)$ by considering the coverage-dependent sticking coefficients of the reactive hydrocarbons. Chuang and Woon[251] find that their $\Theta(t)$ data associated with the increasing nucleation density can be well fitted by the classic 2D Johnson-Mehl-Avrami-Kolmogorov (JMAK) model. Despite agreements with each respective experimental data, the current models come in a variety of mathematical forms while the subject process is largely identical. It is

therefore sensible to expect a unified model that can rationalize the general edge-attachment Cu-CVD results by capturing the most essential kinetic features.

Another problem is that the current kinetic models for the edge-attachment-controlled growth are based on the simplistic assumption of the instantaneous nucleation. The graphene nucleation density is assumed to instantly increase upon supersaturation to its saturated level and remain constant during the subsequent growth. $\Theta(t)$ is hence claimed to be trivially proportional to $A(t)$. However, the continuous nucleation kinetics, also called the continuous nucleation, does exist in a broad range of CVD experiments For instance, Terasawa *et al*[71] has observed the increasing nucleation density accompanying the domain enlargement through the real time radiation-mode optical microscopy. The ex situ CVD experiments have frequently noticed the non-uniform distribution of the graphene domain sizes. It strongly indicates that not all nuclei are formed within the initial instants because those emerging later are generally of smaller sizes than those earlier. For instance, Geng *et al*[252] has shown a SEM image of the partially covered graphene domains on Cu, which evidences the existence of the smaller domains located within the gaps among the much larger domains. By mapping the crystalline orientations of the well-connected graphene domains, Ago *et al*[88] also shows the co-existence of domains with largely differing sizes. The post-growth statistical investigations of Wu *et al*[219] directly show the flat distribution of graphene domain sizes at both partial and full coverage. By means of the Raman 2*D* intensity mapping of the graphene domains sequentially labelled by the carbon isotopes, Hao *et al*[62] has discovered not only the non-uniform size distribution but also that some nuclei emerge even after ~40 min carbon exposure (corresponding to ~65% coverage). On the one hand, the continuous nucleation means increasing nucleation density $N(t)$, which also needs to be quantitatively described but not yet in the reported work. On the other hand, the coverage $\Theta(t)$ is no longer naively proportional to the domain area $A(t)$ due to the changing nucleation density. The inter-domain competitions for the surface hydrocarbons also become time-dependent in contrast to the time-independent inter-domain competitions in the instantaneous nucleation systems. Hence the quantitative behaviours of $\Theta(t)$ and $A(t)$ for the edge-attachment-controlled growth have to be modelled by a more elaborate kinetic theory that incorporates the non-trivial influence of the continuous nucleation and the associated complex inter-domain competitions.

Also remaining for a deep study is the kinetics of the surface-diffusion-controlled graphene growth. The Cu-CVD experiments have frequently observed the diffusion-

controlled growth which is generally associated with the formation of dendritic graphene domains.[62,66,195,198,253] Obviously the time-evolutions in this regime should be different from those in the edge-attachment-controlled regime. Meanwhile, in the real 2D CVD systems, the surface hydrocarbons will simultaneously diffuse towards all the surrounding domains. Hence the potential models should also incorporate the effects of the inter-domain competitions. Although the recently established phase-field models can simulate the evolutions of the domain sizes and the hydrocarbon concentration field, they only address the growth of single isolated domain without considering the inter-domain competition.[62,72] Consequently these models fail to explicate the time-converging behaviour of the graphene domain areas which have been confirmed by the in situ CVD experiments.[254] Another drawback is that the simulation framework is generally unable to derive closed-form solutions which are actually necessary for insightful understanding. This is mostly because they take the approach of the order parameter field instead of explicit treatments of the boundary conditions at the phase interface. In this sense, a new model for the diffusion-controlled growth is desirable, which, on the one hand, should elucidate how the inter-domain competitions affect the diffusion-controlled growth, and on the other hand, should be mathematically tractable.

This work has constructed a quantitative model for the self-limiting kinetics of both the edge-attachment-controlled and the surface-diffusion-controlled CVD of graphene. The analysis focuses on the Cu-catalyzed growth using CH_4 and H_2 as the forming gas. The model is built on the assumptions of the simple first-order nucleation and first-order growth. The applicability of the derived conclusions in the real CVD processes justify the first-order assumptions. Different from the previous studies, this model formally takes into account the critical influences of the inter-domain competitions, which will be treated as time-dependent in the edge-attachment-controlled regime, also called the nucleation-growth convolution, and time-independent in the diffusion-controlled regime. Recognizing the inter-domain competitions enables correct fitting of a broad range of literature CVD data, whose time-dependences otherwise appear too diverse to be modelled by single kinetics. The measured nucleation density $N(t)$ is also fitted to high accuracy. This model can derive certain analytical solutions which promote more insightful understanding than the phase-field simulations. For instance, the initial time-dependence of the domain radius is proven to be linear and square-root for the edge-attachment-controlled and surface-diffusion-controlled growth, respectively. The model is then used to derive the dependences of the graphene growth on the growth

temperature and the CH_4 partial pressure. The derived conclusions can provide theoretical foundation for the widely used two-step synthesis technique, i.e., increasing the CH_4 partial pressure for higher coverage without sacrificing the domain size. The internal correlations among the activation energies are predicted. The critical ratio controlling the rate-limiting step is identified. This model also provides an accessible illustration for the formation of the compact and dendritic domain outlines driven by the edge-attachment-controlled and diffusion-controlled kinetics, respectively.

6.2 Modelling the Edge-Attachment-Controlled Growth Kinetics

6.2.1 First-order Rate equations for Nucleation and Growth

Figure 6.2 compares the scenarios of the instantaneous nucleation to the continuous nucleation. For the instantaneous nucleation case (Figure 6.2(a)), the nucleation density instantly increases to its saturated level once the nucleation initiates. The domains then enlarge while their areal density remains constant and hence the increase of the coverage is solely contributed by the domain growth. All of the surface hydrocarbons are to be consumed only by the domain growth while none of them by nucleation. Therefore the competitions for the hydrocarbons exist only among the growth of the spatially neighbouring domains, i.e., the time-independent inter-domain competitions. In contrast, for the continuous nucleation case, new nuclei keep emerging while the existing domains are enlarging (see Figure 6.2(b)). The increase of the nucleation density and the increase of the domain sizes both contribute to the increase of the coverage. The surface hydrocarbons can now be consumed by two competitive pathways: they can either form a new nucleus or get attached to the edges of the existing domains. Consequently there are now three types of time-dependent competitions for the surface hydrocarbons: those among the neighbouring nucleation events, those among the neighbouring domain growth and those between the neighbouring nucleation and domain growth. They will also be collectively called the nucleation-growth convolution.

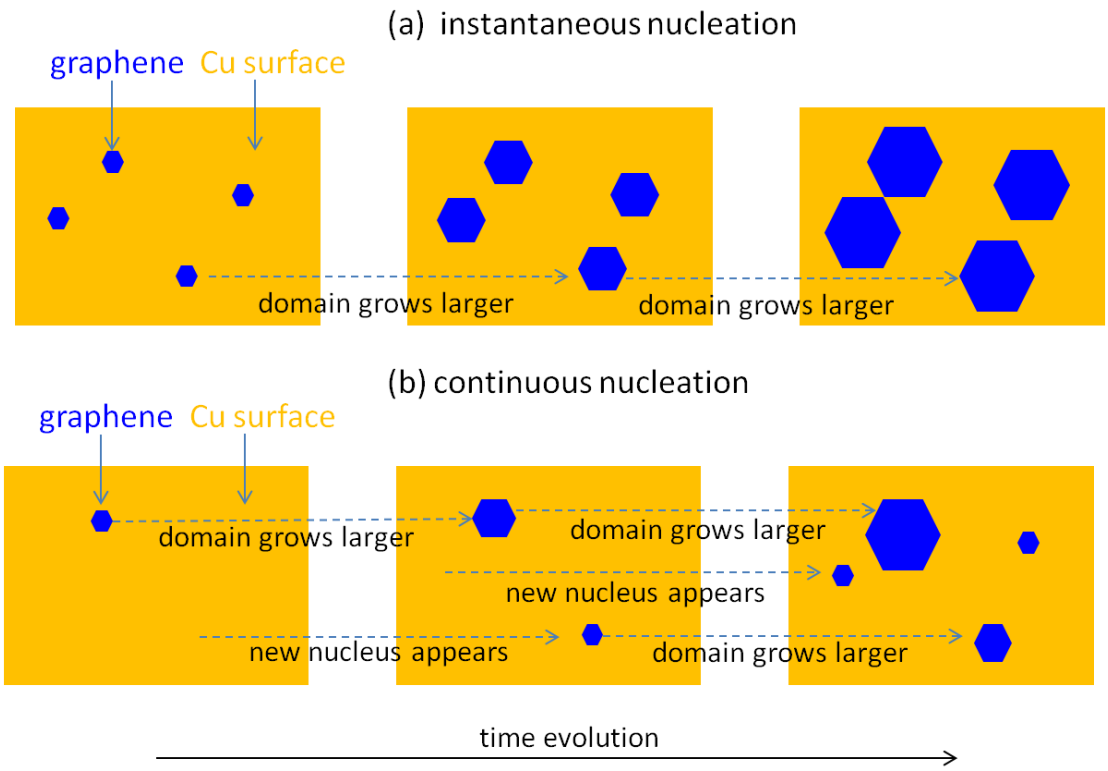

Figure 6.2. Schematic illustrations of the evolutionary graphene nucleation density, domain size and coverage for (a) instantaneous nucleation and (b) continuous nucleation.

The carbon isotope labelling experiments of Hao *et al* have offered direct evidence for the nucleation-growth competition.[62] Figure 6.3(a) shows the evolutionary outline of an enlarging irregular hexagonal domain (marked as A) enclosed by the dashed line. Located to its upper-right side is domain B which emerged almost simultaneously with domain A. In contrast, to its lower-left side is domain C which emerged about 3 min later than domain A. The growth of domain A toward the C side is therefore damped relative to that toward the B side. Figure 6.3(b) plots the time-dependences of the domain radius along the pristine and damped sides, denoted by $L(t)_{pristine}$ and $L(t)_{damped}$, respectively. The $L(t)_{damped}$ overlaps with the $L(t)_{pristine}$ within the initial 10 min growth, but afterwards it is significantly suppressed compared to $L(t)_{pristine}$. It is reasonable to assert that $L(t)_{damped}$ has to be described by new rate equations different from the normal equations that $L(t)_{pristine}$ satisfies. This clearly substantiates that the growth of one individual domain is affected not only by the growth of its surrounding domains but also a single nucleation event within its neighbourhood.

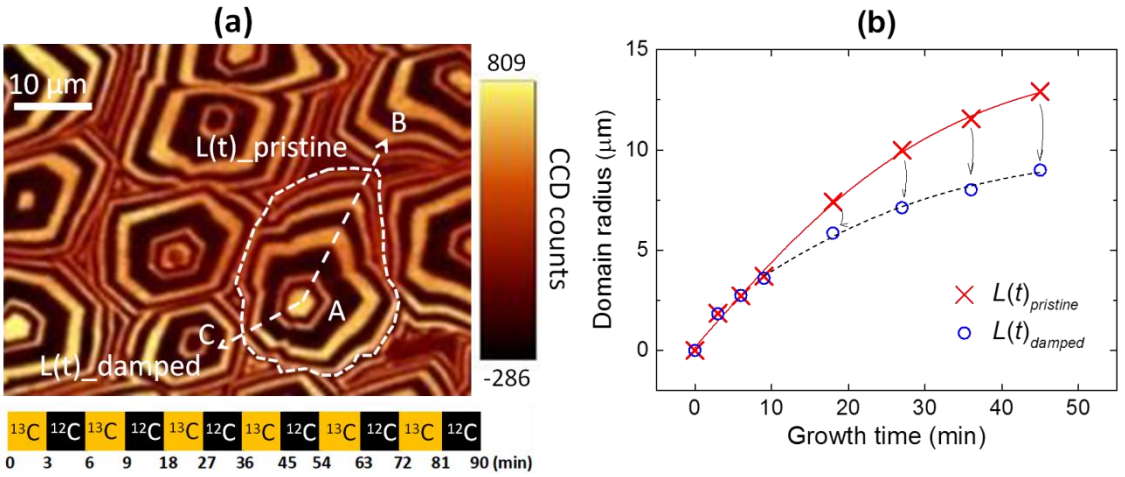

Figure 6.3: (a) Raman 2*D* peak intensity maps of the evolutionary outline of the graphene domains sequentially labelled by carbon isotopes. Adapted from Hao *et al.*[62] (b) Extracted time-dependence of the domain radius along the pristine and the damped sides.

To incorporate the continuous nucleation in modelling the edge-attachment-controlled kinetics, we start with establishing the growth equation for the domain sizes. As shown in schematic of Figure 6.1, the Cu-catalyzed growth of an individual domain is a consequence of the competition between the attachment and detachment (etching) of the hydrocarbon species at the domain edges. The attachment rate can be assumed linearly proportional to the concentration of the hydrocarbon monomers CH_x (x=0, 1, 2, or 3) on the Cu surface. This is equivalent to the widely acknowledged first-order reaction. For instance, Safron and Arnold have found a linear dependence of the domain growth rate on the partial pressure of CH_4 (P_{CH_4}).[70] Some other investigations have based their theory on the assumption of the first-order reaction, such as Kim *et al*,[182] Meca *et al*,[66] Eres *et al*,[250] etc. The reasonableness of their theory justifies the assumption of the first-order reaction. The detachment rate can be represented by a etching term since a large number of CVD experiments have reported graphene edge etching or domain shrinkage under sufficient H_2 partial pressure (P_{H_2}).[164,255–260] Combining the attachment and detachment terms yield the equation for the domain area growth rate:

$$\frac{dA(t)}{dt} = \sqrt{A(t)} \cdot \left[k_{att} \cdot C_{Cu}(t) - r_{growth\_etch} \right]$$

or equivalently the equation for the domain radial growth rate:

$$\frac{dL(t)}{dt} = \frac{1}{2}\left[k_{att} \cdot C_{Cu}(t) - r_{growth\_etch}\right] \qquad (6.2.1)$$

where $A(t)$ is the average domain area at time t, $L(t) = \sqrt{A(t)}$ is the equivalent average domain radius, $C_{Cu}(t)$ is the concentration of the hydrocarbons on the Cu surface, k_{att} denotes the rate coefficient of edge-attachment, respectively. r_{growth_etch} is the rate of domain edge etching. In principle it could be proportional to P_{H_2} but we temporarily approximate it as constant. The growth rate of the domain area is set proportional to the domain radius in the edge-attachment-controlled regime because the concentration of the available attachment sites is proportional to the domain perimeter.

The terms appearing in the growth rate equation are closely related to the CVD process conditions. The surface hydrocarbons are supplied from the catalytically dehydrogenated CH_4 so $C_{Cu}(t)$ should be dependent on P_{CH_4} and P_{H_2}. Since the edge attachment is a thermally activated process, $k_{att} \sim K' \cdot \exp\left(-E_{att}/k_B T\right)$ where E_{att} is the activation energy for the Cu-catalyzed edge attachment, K' presents the other factors affecting the growth rate, k_B is the Boltzmann constant and T is the temperature. The etching rate r_{growth_etch} should also depend on the growth temperature in an Arrhenius type, i.e., $r_{growth\_etch} \propto \exp\left(-E_{growth\_etch}/k_B T\right)$, where E_{growth_etch} is the activation energy for removal of a carbon atom from the domain edge. The growth equation indicates the existence of a critical value for the surface hydrocarbon concentration, $C_{growth\_critical} = r_{growth\_etch}/k_{att}$. If the initial concentration (i.e., the supersaturation level) $C_{Cu}(0)$ exceeds the critical level, $C_{Cu}(0) > r_{growth\_etch}/k_{att}$, the graphene growth can proceed until the concentration drops to the critical level. In this sense $C_{growth\_critical}$ can be interpreted as the equilibrium concentration C_{eq} at which the edge attachment is balanced with the detachment and the domain size reaches its saturation.[182] Yet there will be no graphene growth from the beginning if $C_{Cu}(0) < r_{growth\_etch}/k_{att}$. This can explain the critical methane concentration (CMC) discovered by the CVD experiments of Safron and Arnold as well as other investigations.[70,71,73] The temperature dependence of k_{att} and r_{growth_etch} suggests that the critical concentration should be exponentially dependent on the inverse temperature, $C_{growth\_critical} \propto \exp\left(\left(E_{att} - E_{growth\_etch}\right)/k_B T\right)$. This can rationalize the experimental finding of Safron and Arnold:

$\mathrm{CMC} \propto \exp\left(0.51\mathrm{eV}/k_B T\right)$.[70] The measured positive activation energy difference in turn suggests $E_{att} > E_{growth\_etch}$.

Next we build the nucleation rate equation assuming the nucleation rate is first-order dependent on the concentration of the hydrocarbon monomers on the Cu surface and hindered by a constant etching term. The former is equivalent to the assumption of atomic size critical nucleus, i.e., a nucleus is formed from a single hydrocarbon monomer suitably accommodated on the Cu surface sites. Both assumptions are favoured by a number of experimental reports. For instance, the measurements of Safron and Arnold[70] show that the average nucleation rate scales linearly with $P_{\mathrm{CH_4}}$. Recalculation from the data provided by Zhou *et al*,[59] Zhang *et al*,[261] and Seifert *et al*[262] also suggests the linear dependence. Meanwhile Safron and Arnold[70] and Terasawa *et al*[71]have found that the sufficient post-growth H_2 exposure can effectively etch and erase the existing nucleus. Other studies have also substantiated that increasing $P_{\mathrm{H_2}}$ can effectively decrease the graphene nucleation density.[59,199,263] Therefore the nucleation rate is modelled as:

$$\frac{dN(t)}{dt} = k_{nuc} \cdot C_{Cu}(t) - r_{nucleus\_etch} \qquad (6.2.2)$$

where $N(t)$ is the graphene nucleation density at time t and k_{nuc} is the nucleation rate coefficient. $r_{nucleus\_etch}$ is the nucleus etching rate which should also depend on $P_{\mathrm{H_2}}$ but will be approximately treated as constant. k_{nuc} and $r_{nucleus\_etch}$ should be Arrhenius dependent on the growth temperature, with an activation energy of E_{nuc} and $E_{nucleus\_etch}$. k_{nuc} could also contain other kinetic factors affecting the nucleation rate such as the Cu surface vacancies, atomic steps, or impurity centres since these regions are well known as the active nucleation sites.[184,223,264] Therefore k_{nuc} can be expressed as $k_{nuc} \sim K'' \cdot \exp\left(-E_{nuc}/k_B T\right)$ where K'' collectively represents the kinetic factors. There should also be a critical hydrocarbon concentration for nucleation equal to $r_{nucleus\_etch}/k_{nuc}$. However there is no such a underlying mechanism that guarantees $r_{growth\_etch}/k_{att} = r_{nucleus\_etch}/k_{nuc}$ under general growth conditions.

Regarding the concentration of the Cu surface hydrocarbons, this model will adopt Kim's proposal that the dynamic equilibrium between the adsorption and desorption of the hydrocarbon species is reached much faster than the nucleation and growth of

graphene.[183] This equivalently claims that the total surface concentration conserves after the chemical supersaturation is reached:

$$C_{Cu}(t)+C_G(t)=C_0\ , \qquad (6.2.3)$$

where $C_{Cu}(t)$ and $C_G(t)$ is the surface concentration of the unbound hydrocarbons and crystallized carbon atoms at time t, respectively, and C_0 is the supersaturation concentration as well as the constant total concentration. $C_G(t)$ is proportional to the graphene coverage $\Theta(t)$:

$$C_G(t)=\rho_G\cdot\Theta(t)=\rho_G\cdot N(t)\cdot A(t)=\rho_G\cdot N(t)\cdot L(t)^2 \qquad (6.2.4)$$

where ρ_G is the constant areal density of the carbon atoms in the graphene lattice (= 3.82×10^{-15} cm^{-2}) and $\Theta(t)$ is expressed as the product of $N(t)$ and $A(t)$. Since the Cu surface hydrocarbons are mostly supplied from the catalytically dehydrogenated CH_4, the entire chemical reaction can be written as $CH_{4(g)} \rightleftarrows CH_x+\frac{4-x}{2}H_{2(g)}$.Therefore the equilibrium surface concentration of CH_x, i.e., the supersaturation concentration C_0, is controlled by the CVD gas conditions:

$$C_0=K\cdot P_{CH_4}\cdot\left(P_{H_2}\right)^{(x-4)/2},$$

where K is the corresponding equilibrium constant. The value of x reflects the atomic structure of the hydrocarbon monomer to be attached onto the graphene domain edge, which is currently in controversy. Kim *et al*[183] and many other authors[265] take $x = 0$ in their theoretical investigations while the CVD measurements of Safron and Arnold favour $x = 1$.[70] Atomic level simulations are needed to clarify the dominant attachment species so we will keep the undefined form CH_x in this research.

Combining Equations 6.2.1, 6.2.2, 6.2.3, and 6.2.4 yields the time-evolution equations for $L(t)$, $N(t)$, and $\Theta(t)$ that are mathematically complete (see Equation A1.1 in Appendix 1). It is worth noting that the product term $N(t)\cdot L(t)^2$ reflects the noted nucleation-growth convolution (time-dependent inter-domain competition). It makes the equations for $N(t)$ and $L(t)$ non-linear, convoluted and un-separable. Therefore it represents the non-trivial influence of the nucleation-growth convolution on the graphene formation kinetics which has not been incorporated in the prior models assuming instantaneous nucleation.

6.2.2 Two-stage Graphene Formation Kinetics

By defining $k_1 = k_{att} \cdot \rho_G$, $k_2 = k_{nuc} \cdot \rho_G$, $\Theta_{s1} = \left(C_0 - r_{growth\_etch}/k_{att}\right)/\rho_G$ and $\Theta_{s2} = \left(C_0 - r_{nucleus\_etch}/k_{nuc}\right)/\rho_G$ (see Equation A1.2 in Appendix 1), Equation A1.1 are re-arranged into Equation A1.3 which now manifests clearer physical meanings. Since $N(t)\cdot L(t)^2 = \Theta(t)$ is the graphene coverage, $L(t)$ and $N(t)$ keep increasing with time at a decreasing rate until the coverage hits Θ_{s1} and Θ_{s2} when the increase rate of $L(t)$ and $N(t)$ decrease to zero, respectively. In this sense, Θ_{s1} and Θ_{s2} can be interpreted as the coverage when the time-evolution of $L(t)$ and $N(t)$ reaches saturation, respectively. Θ_{s1} and Θ_{s2} are determined as the levels of the hydrocarbon supersaturation for growth and nucleation, respectively. Their values depend on C_0, k_{att}/k_{growth_etch} and $k_{nuc}/k_{nucleus\_etch}$ which are further decided by P_{CH_4}, P_{H_2}, and T. As stated above Θ_{s1} is not necessarily equal to Θ_{s2}. Indeed most CVD studies have observed $\Theta_{s2} \leq \Theta_{s1}$, i.e., the nucleation is completed no later than the domain growth.[62,266,267] The inequality relation $\Theta_{s2} \leq \Theta_{s1}$ indicates the entire graphene formation undergoes two successive stages.

Stage 1: The first stage, named as Stage 1, corresponds to $0 \leq \Theta(t) < \Theta_{s2}$ during which both of the $L(t)$ and $N(t)$ are increasing with time at decreasing rates and hence cooperatively contribute to the increase of the coverage $\Theta(t)$. Meanwhile, the nucleation and growth are competing for the surface hydrocarbons. The increase of $L(t)$ and $N(t)$ not only causes each owns increase rate to drop but also mutually damps each other's increase rate. In another word, the evolutions of $L(t)$ and $N(t)$ are convoluted.

Stage 2: The second stage, named as Stage 2, corresponds to $\Theta_{s2} \leq \Theta(t) < \Theta_{s1}$ during which $N(t)$ remains at its saturated level after the nucleation rate decreases to zero while $L(t)$ keeps increasing until the coverage $\Theta(t)$ reaches Θ_{s1}. Therefore the increase of coverage is solely contributed by the increase of $L(t)$. There is no longer competition between nucleation and growth as all of the surface hydrocarbons are consumed solely by the domain enlargement. The growth rate of $L(t)$ is dropping as the coverage is increasing and finally decreases to zero when the coverage reaches Θ_{s1}. This is also the moment at which the rate of the edge attachment is balanced with the rate of edge etching. The domain size, the nucleation density and the coverage remain at their saturated level afterwards.

We will show in the coming discussions that recognizing the intrinsic existence of the two-stage graphene formation, which has been ignored in previous modelling work,

is the key to understand a broad range of observed CVD phenomenon. Its influence on the edge-attachment-controlled graphene formation kinetics can be quantified by a new parameter *p*, defined as $p = (\Theta_{s2}/\ \Theta_{s1})^{1/3}$. Since $\Theta_{s2} \leq \Theta_{s1}$, the value of *p* falls within the range of [0, 1]. *p* reflects the magnitude difference between Θ_{s2} and Θ_{s1}. Small values of *p* indicate that the nucleation density reaches its saturated level much earlier than the domain size and vice versa. It is also a quantitative gauge of the intensity of the nucleation-growth convolution. More specifically, $p = 0$ corresponds to the trivial zero-convolution kinetics, i.e., the instantaneous nucleation, in which case Stage 2 fully dominates the growth process while the duration of Stage 1 is zero. $p = 1$ corresponds to the most intense convolution, i.e., both nucleation and growth continue in the convoluted manner throughout the entire process, in which case Stage 1 fully dominates the growth process while the duration of stage 2 is zero. $0 < p < 1$ corresponds to the intermediate level of convolution, i.e., the typical two-stage kinetics. Because of these the parameter *p* will be called the nucleation-growth convolution intensity. Obviously the value of *p* is process dependent:

$$p = \left(\frac{\Theta_{s2}}{\Theta_{s1}}\right)^{1/3} = \left(\frac{K \cdot \dfrac{P_{CH_4}}{\left(P_{H_2}\right)^{(4-x)/2}} - \dfrac{1}{K''} \cdot \exp\left(\dfrac{E_{nuc} - E_{nucleus\_etch}}{k_B T}\right)}{K \cdot \dfrac{P_{CH_4}}{\left(P_{H_2}\right)^{(4-x)/2}} - \dfrac{1}{K'} \cdot \exp\left(\dfrac{E_{att} - E_{growth\_etch}}{k_B T}\right)}\right)^{1/3} \qquad (6.2.5)$$

where *K*, *K*' and *K*'' represent the factors associated with each respective reaction equilibrium constant as defined in previous discussions.

6.2.3 Solutions to the First-order Rate Equations

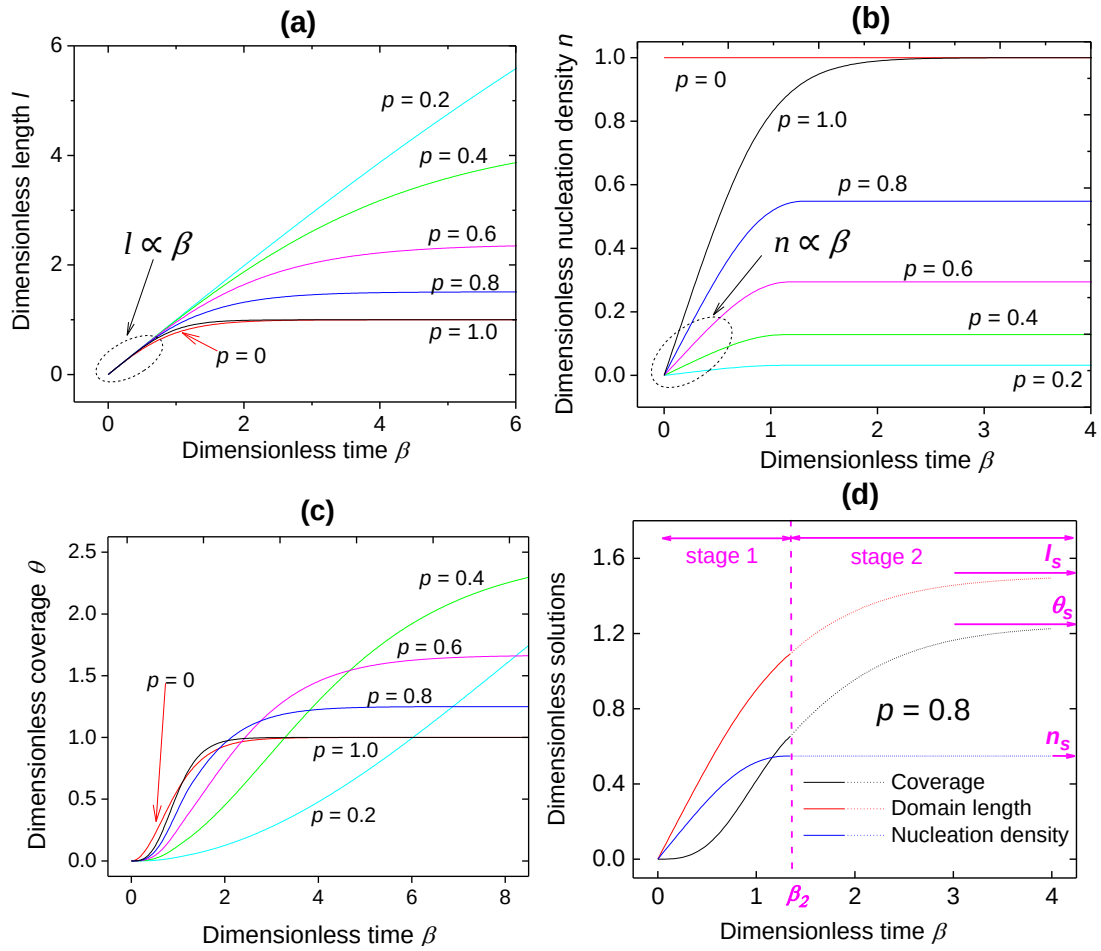

Figure 6.4: Solution plots of the edge-attachment-controlled kinetic equations for (a) $l(\beta)$, (b) $n(\beta)$, and (c) $\theta(\beta)$ under p = 0, 0.2, 0.4, 0.6, 0.8, 1.0. (d) Two-stage growth of $l(\beta)$, $n(\beta)$, and $\theta(\beta)$ under p = 0.8. Solid and dashed lines correspond to Stage 1 and Stage 2, respectively. β_2 is the ending time of Stage 1 as well as the beginning time of Stage 2.

The role of the nucleation-growth convolution intensity in controlling the graphene formation kinetics is further elucidated in the dimensionless forms (Equations A1.6 in Appendix 1) of the original equations for $L(t)$, $N(t)$, and $\Theta(t)$. In Appendix 1 are also defined the characteristic domain radius L_c, the characteristic nucleation density N_c, the characteristic coverage Θ_c, the characteristic time t_c, the dimensionless domain radius l, the dimensionless nucleation density n, the dimensionless coverage θ, and the dimensionless time β (see Equations A1.4 and A1.5). Since p is the only parameter, the unique solutions to the time-evolution equations can be determined for each given value of p. For p = 1, the equations for $n(\beta)$ and $l(\beta)$ become identical and hence $n(\beta) = l(\beta)$, $\theta(\beta) = l(\beta)^3$. Now the nucleation density and the domain radius increase with time in a completely synchronized and coherent pace throughout the entire growth process, i.e.,

they are fully convoluted. In another word, Stage 1 fully dominates the growth process while the time span of Stage 2 is zero. On the one hand, the competitions between nucleation and domain growth for the Cu surface hydrocarbons last from the onset to the final equilibrium. On the other hand, the increase of both the nucleation density and the domain radius contribute to the increase of coverage, which is the origin of the remarkable cubic relation $\theta(\beta) = l(\beta)^3$. For $p = 0$, the nucleation density keeps constant, $n(\beta) \equiv 1$, and the coverage is related to the domain radius by $\theta(\beta) = l(\beta)^2$. Now Θ_{s2} is zero implying that the graphene nucleation saturates immediately upon exposure to the hydrocarbon precursors. Towards this limit our model virtually recedes to the previously established model assuming instantaneous nucleation,[182] where Stage 2 now fully dominates the growth process while the time span of Stage 1 is zero. The equations can be analytically solved for both $p = 1$ and $p = 0$ but have to be numerically solved for $0 < p < 1$.

Figure 6.4 plots the solutions for $l(\beta)$, $n(\beta)$ and $\theta(\beta)$ as the p-family curves (see Equations A1.4-A1.11 in Appendix 1 for detailed derivations of the solutions). Figure 6.4 (a) shows that, for all values of p, $l(\beta)$ features an initial linear increase with time. The similar initial linear dependence is also observed for $n(\beta)$ except for $p = 0$ where the nucleation density remains constant (see Figure 6.4 (b)). These linear behaviours can be rationalized by the asymptotic solutions under the limit of $\beta \to 0$:

$$p = 0 \xrightarrow{\beta \to 0} \begin{cases} l \approx \beta \\ n \equiv 1 \\ \theta \approx \beta^2 \end{cases} \qquad 0 < p \leq 1 \xrightarrow{\beta \to 0} \begin{cases} l \approx \beta \\ n \approx p^2 \cdot \beta \\ \theta \approx p^2 \cdot \beta^3 \end{cases} .$$

The physical cause for the initial linearity of $l(\beta)$ is the edge-attachment-controlled kinetics, i.e., the growth rate of the domain area is proportional to the domain perimeter. The asymptotic properties of the $l(\beta)$ and $n(\beta)$ solutions provide a straightforward explanation for the initial linearity of the domain radius-time dependence that has been widely observed in a large number of both in situ and ex situ CVD experiments,[62,71–73,78,82,267–271] and that of the nucleation density-time dependence observed by Chuang and Woon,[251] Terasawa *et al*,[71] etc. The initial coverage growth dynamics consequently follows quadratic time-dependence for $p = 0$, i.e., $\theta(\beta) \propto \beta^2$ and cubic time-dependence for $0 < p \leq 1$, i.e., $\theta(\beta) \propto \beta^3$. Thereby, regardless of the nucleation-growth convolution intensity, the theoretical $\theta(\beta)$ plots behave convex as $\beta \to 0$ (see Figure 6.4(c)). This can well explain the widely observed initial upward curvature of the experimental coverage-

time dependences, such as that of Eres *et al*,[250] Celebi *et al*,[233] Hao *et al*,[62] and other studies.[205,251,272] As the nucleation and growth proceed, the area of the catalytic Cu surfaces decreases and the inter-domain competitions intensify so that the increase rates of $l(\beta)$ and $n(\beta)$ monotonically decrease towards zero (see Figure 6.4 (a) and (b)). Consequently the increase rate of the coverage fades with time for all values of p and the $\theta(\beta)$ curves gradually turn concave as shown in Figure 6.4 (c). This, together with the convex parts, can elucidate the S-shaped $\theta(\beta)$ curves that have been extensively observed in the CVD experiments.[62,218,250,262,272]

The saturation values of $l(\beta)$, $n(\beta)$ and $\theta(\beta)$ are affected by the nucleation-growth convolution intensity. Figure 6.4(a) and Figure 6.4(b) show that larger p generally allows lower saturated value l_s for $l(\beta)$ in contrast to higher saturated value n_s for $n(\beta)$. Such an opposite influence can be intuitively understood by noticing that p is defined as $(\Theta_{s2}/\Theta_{s1})^{1/3}$ where Θs_2 and Θs_1 are the saturation coverage for nucleation and growth, respectively. In the case of $p << 1$, these dependences can be approximately quantified by $n_s \approx p^2$ and $l_s \approx p^{-3/2}$ (see Equations A1.12-A1.14 in Appendix 1). Figure 6.4(c) further shows that the higher saturated coverage can be achieved under smaller p for $0 < p \leq 1$. This can be understood from the mathematical expression of the saturated coverage: $\theta_s = 1/p$ (see Equation A1.12 in Appendix 1). The underlying physical interpretation of this relation is that the saturated coverage with dimensions (experimentally observable), Θ_s, is determined as the level of the hydrocarbon supersaturation:

$$\theta_s = 1/p \quad \rightarrow \quad \Theta_s = \Theta_{s1} = \left(C_0 - k_{growth\_etch}/k_{att}\right)/\rho_G \propto P_{CH_4}. \qquad (6.2.6)$$

Kim *et al*[182] has reached a similar conclusion but that is only applicable to the special case of the instantaneous nucleation ($p = 0$, also discussed in Section 2.3.9). The analysis in this research validates the relation for general CVD processes with the continuous nucleation ($0 < p \leq 1$). Figure 6.4(d) demonstrates the typical two-stage kinetics for $p = 0.8$ where $l(\beta)$, $n(\beta)$ and $\theta(\beta)$ are plotted together. $n(\beta)$ reaches its saturated level n_s at time β_2, the milestone between Stage 1 and Stage 2, and no longer changes afterwards while both $l(\beta)$ and $\theta(\beta)$ keep increasing until they reach their saturated levels l_s and θ_s, respectively.

The theoretical dependence of n_s and θ_s on the convolution intensity p can be applied to provide useful insight regarding the design of graphene CVD recipes. Since $n_s \approx p^2$ for $p << 1$, the saturation density with dimensions N_s (experimentally observable) varies

with the CH_4 partial pressure in the following manner (see Equation A1.15 in Appendix 1 for detailed derivation):

$$N_s \sim P_{CH_4}^{1/3}. \qquad (6.2.7)$$

The cubic-root dependence is also validated for $p = 1$ (see Equation A1.16 in Appendix 1). For general values of p, there are no closed form relation for the dependence of N_s on P_{CH_4}. But it is reasonable to assert the similar cubic-root dependence judging from the results under $p = 1$ and $p << 1$. Kim *et al* has come to a consistent cubic-root relation in the edge-attachment-controlled regime under the theoretical framework of Robinson and Robins.[182] This certainly indicates that low P_{CH_4} should be used to suppress the nucleation density. As stated in Chapter 4, the industrially useable graphene needs to be both full coverage and of large domain sizes. For this some researchers have proposed a two-step synthesis technique, which initially uses low P_{CH_4} to obtain low nucleation density and then increases P_{CH_4} to promote formation of full coverage.[54,61] Yet there is currently no clear explanation for why increasing P_{CH_4} can increase the coverage more than the nucleation density. According to our model, this is fundamentally because $\Theta_s \sim P_{CH_4}$ and $N_s \sim P_{CH_4}^{1/3}$, i.e., the saturated coverage increases with P_{CH_4} faster than the saturated nucleation density (schematically shown in Figure 6.5).

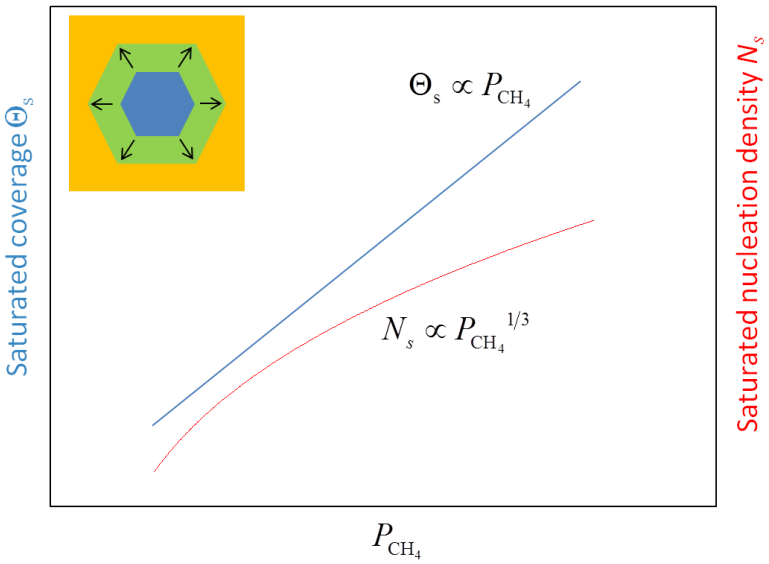

Figure 6.5: Power law dependence of the saturated coverage and nucleation density on the CH_4 partial pressure. The inset shows the coverage increases with the CH_4 partial pressure much more than the nucleation density.

6.2.4 Fitting Edge-attachment-controlled CVD Data

The proposed edge-attachment-controlled growth model can well describe a broad range of kinetic CVD data. The above analysis has shown that the convolution intensity controls the solutions to the kinetic equations, so the first step to fit the experimental data is to determine the value of p for each corresponding CVD condition. This can be done by using the definition of p, $p = (\Theta_{s2}/\Theta_{s1})^{1/3}$, where the values of Θ_{s2} and Θ_{s1} can be measured from the post-growth graphene/Cu samples as the coverage when the nucleation and growth reach saturation, respectively. The equations are then solved under each computed p and the derived solutions are used to fit the literature data. Figure 6.6(a) shows that the domain radius-growth time data points for $p = 0$, which are extracted from the publications reporting instantaneous nucleation, can be excellently fitted by the theoretic solution $L=L_c\cdot\tanh((t-t_0)/t_c)$.[71,73,269,271–273] The coverage-time data with $p = 0$ from Kidambi *et al* is also fitted using the analytical solution for $\theta(\beta)$ (see Figure 6.6(b)).[266] For general values of p ($0 < p < 1$), there are no analytic solutions so we set as fitting parameters the characteristic coverage Θ_c, the incubation period t_0 and the characteristic time t_c. They are evaluated at those that can minimize the residual-square-sum when fitting the accordingly normalized data $\Theta/\Theta_c - (t-t_0)/t_c$ against the numerical solution of $\theta(\beta)$. Figure 6.6(c), (d), and (e) show that the coverage-time data points with p = 0.36, 0.66, and 0.87 can be well fitted by the corresponding numerical $\theta(\beta)$ after they are normalized by the optimal characteristic scales, respectively.[62,267] For $p = 1$, the analytical solution for $\theta(\beta)$ is able to fit the data points of Hao *et al* (see Figure 6.6(e)).[62]

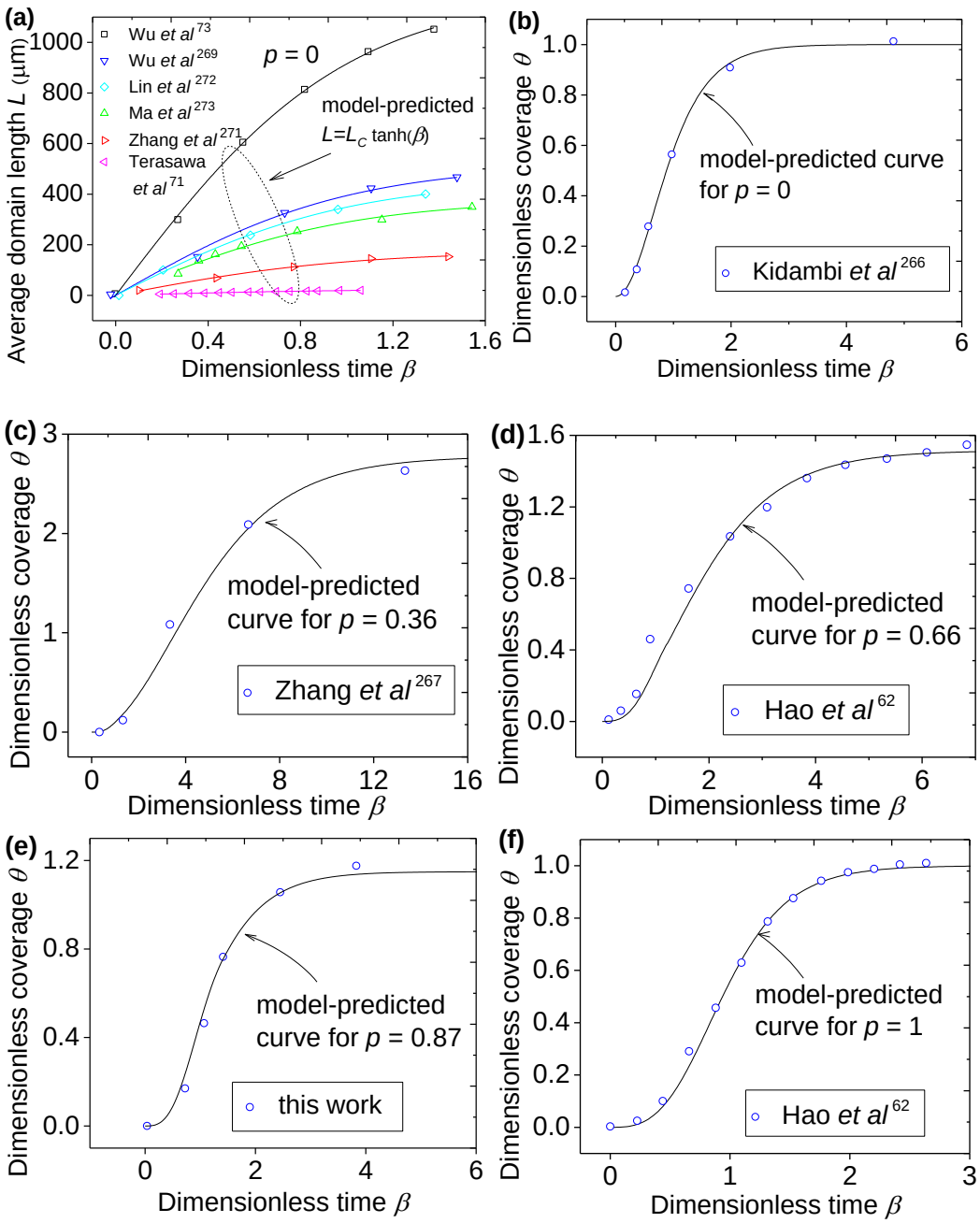

Figure 6.6:. (a) Fitting literature-reported time-dependence of average domain radius with $p = 0$. The original growth time t has been normalized into the dimensionless time $\beta = (t - t_0)/t_c$ using the fitted incubation period t_0 and the characteristic time scale t_c while the dimension of the domain radius is preserved. (b)-(f) Fitting the reported time-dependence of coverage with p = 0, 0.36, 0.66, 0.87 and 1 using the corresponding solution of $\theta(\beta)$, respectively. The CVD conditions used in this work are: 900 ^{o}C, 0.12 sccm CH_4, 10 sccm H_2 and 490 sccm Ar.

This model can also explicate the experimentally measured time-evolution of graphene nucleation density. Figure 6.7(a) shows that the nucleation density-growth time data series under five temperature, obtained from the in situ CVD experiments of Terasawa *et al*,[71] can be fitted by the predicted $n(\beta)$ for $p = 1$ to high accuracy. As far as

we know, this is the first quantitative description of the evolutionary nucleation density of the self-limiting graphene formation. Figure 6.7(b) demonstrates the equivalent fitting in the dimensionless representation where all of the temperature-series data have been normalized by the corresponding fitted parameters.

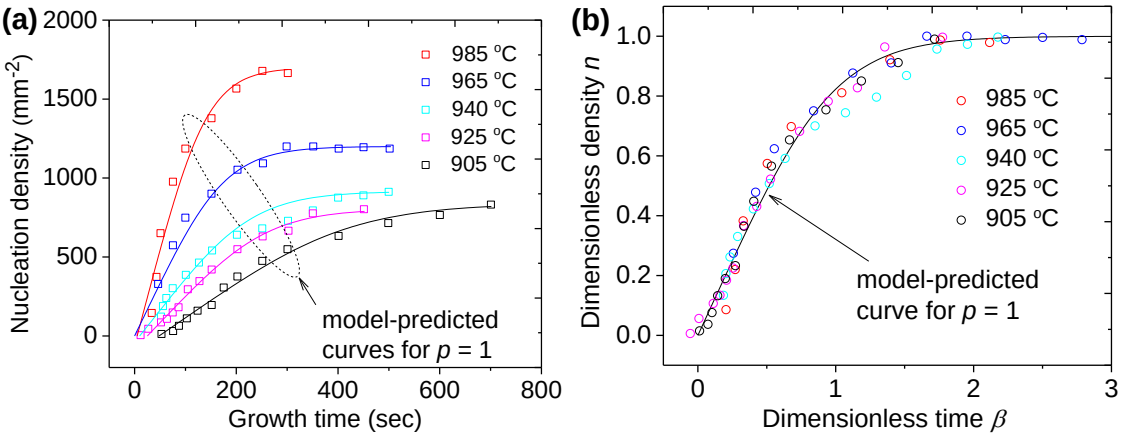

Figure 6.7: (a) Fitting the in situ time-dependence of the nucleation density under growth temperature of 905 °C, 925 °C, 940 °C, 965 °C, 985 °C using the $n(\beta)$ solution for $p = 1$. Data source: Terasawa *et al.*[71] (b) Dimensionless representation of the fitting results in (a). The original nucleation density-growth time data points have been normalized by the fitted parameters (the characteristic nucleation density N_c, the incubation time t_0, and the characteristic time t_c).

The above fitting analysis confirms that the proposed edge-attachment-controlled theory, for the first time, has correctly modelled a wide range of general graphene CVD processes. This is enabled by incorporating the continuous nucleation and the associated time-dependent inter-domain competitions. The continuous nucleation phenomenon does exist and play a prominent role in the real CVD processes. Hence this model has necessarily captured the most essential kinetics of the general graphene growth ($0 \le p \le 1$) while the previously established models assuming instantaneous nucleation are only applicable to one of the special subsets ($p = 0$).

6.3 Modelling the Surface-Diffusion-Controlled Growth Kinetics

6.3.1 First-order Rate Equations for Diffusion-controlled Growth

For the surface-diffusion-controlled graphene growth, the characteristic diffusion rate is significantly lower than the edge-attachment rate ($k_{diff} << k_{att}$) and hence the surface diffusion becomes rate-limiting. Obviously the continuous surface diffusion has to be maintained by the hydrocarbon concentration gradient. Therefore the hydrocarbon concentration field is intrinsically space-time dependent for the diffusion-controlled growth in contrast to being constantly homogenous all over the Cu surface for the edge-attachment-controlled growth. This indicates that a proper model for the diffusion-controlled graphene growth should self-consistently incorporate the evolutionary hydrocarbon concentration field.

The original graphene CVD process is two dimensional (2D), but, for simplicity, we will begin with modelling the diffusion-driven growth of the domain radius, i.e., the one dimensional (1D) diffusion-growth system. As will be shown later, 1D is the minimum dimension that reserves the non-trivial kinetic features. The evolutionary concentration field of the surface hydrocarbons can then be denoted as $C(x,t)$ where x is the spatial position in the 1D Cartesian coordinates and t is the growth time. Without loss of generality, we assume a homogenous distribution of the initial hydrocarbon concentration across the entire Cu surface, C_0, and a constant diffusion coefficient independent of space and time, D. It is fundamentally important to note that the underlying assumption of the diffusion-controlled growth ($k_{diff} << k_{att}$), necessarily requires instantaneous nucleation. This is essentially because the concentration of the hydrocarbons at any position is monotonically decreasing with time due to the irreversible nature of the diffusion process. Considering a position where a potential nucleus is to appear some time later, the nucleus should be formed right at the moment when the local hydrocarbon concentration reaches its maxima, i.e., when the supersaturation is established. Afterwards no more nucleation can occur in that position if it didn't happen at the supersaturation moment because the local concentration is always decreasing. The instantaneous nucleation further implies that in theory the sizes of all the graphene domains should be identical at any time. Therefore the evolutionary domain radius is space-independent and hence can be written as $L(t)=\sqrt{A(t)}$ in the

1D modelling system where $A(t)$ is the domain area measured from the 2D experimental system.

It is worth noting that the diffusion process and the growth process are interdependent. This is because the hydrocarbons diffusing towards the graphene domain edges feed the domain growth which in turn influences the spatial distribution of the hydrocarbons. Thereby the concentration field $C(x,t)$ and the domain radius $L(t)$ should be determined by coupled dynamic equations instead of separable equations. Similar to the inter-domain competitions that have been addressed for edge-attachment-controlled growth, the spatially neighbouring domains under diffusion-controlled kinetics also compete for surface hydrocarbons. This should induce the non-trivial damping effect on $L(t)$. To model the inter-domain competitions, the nearest nucleation sites are set equal-distanced by $2L_s$ along the x-axis (see Figure 6.8(i)). The hydrocarbons distributed between the nearest neighbouring sites diffuse symmetrically towards both $+x$ and $-x$ directions. The entire 1D system is now spatially periodic by $2L_s$ so we only need to study the processes within the interval of $[-L_s, L_s]$.

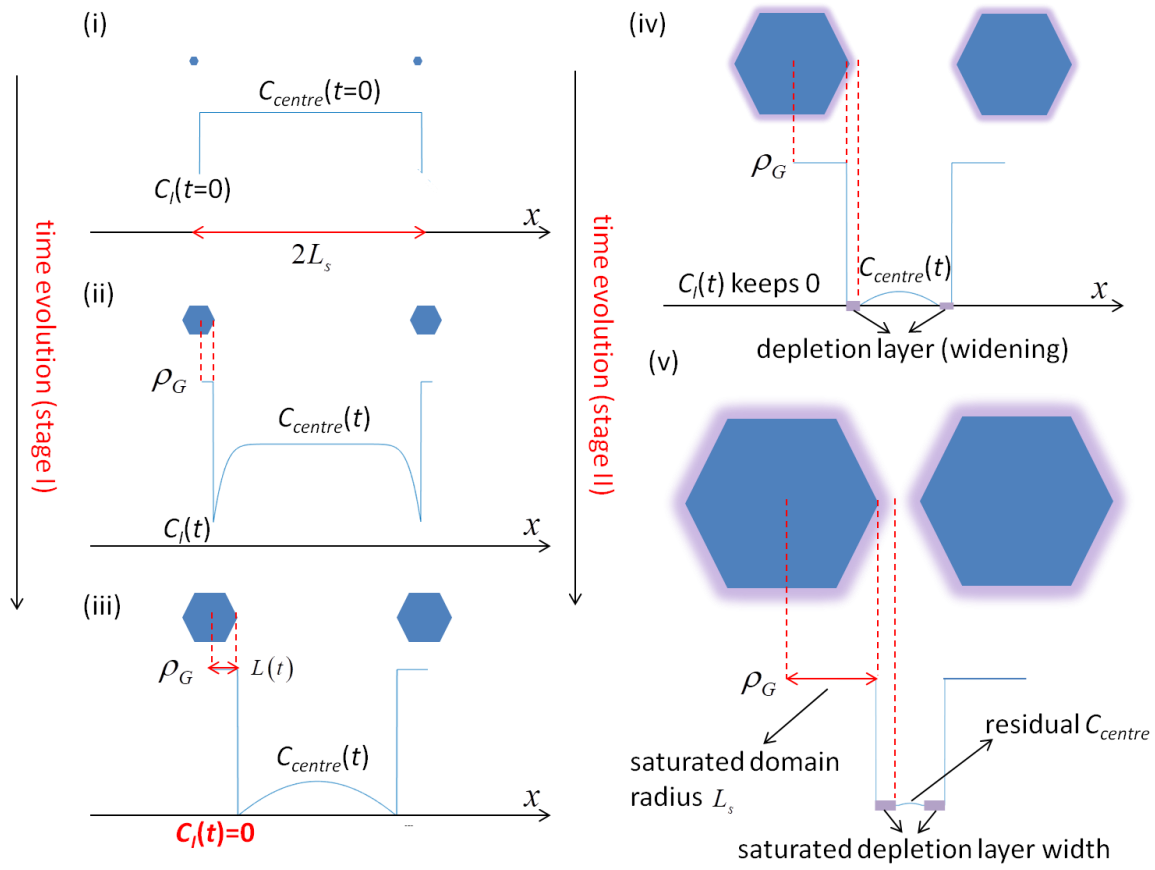

Figure 6.8: Schematic evolution of the diffusion-growth systems. (i) The initial instant. Two nucleus are distanced by $2L_s$ along the x-axis. Solid blue hexagons represent the graphene domains. Solid blue line represents the initial profile of the hydrocarbon concentration. $C_{centre}(t=0)$ and $C_I(t=0)$ are the initial concentration at the centre (x = 0) and the graphene-Cu interface, respectively. (ii) The hydrocarbons start diffusing towards both directions and the domains start growing. (iii) The graphene-Cu interfacial concentration decreases to zero as the domains continue to grow. This is the ending time of Stage I as well as the beginning time of Stage II. (iv) The depletion layer, represented by the purple glow, emerges and expands while the interfacial concentration keeps zero. (v) The net growth rate of domains decrease to zero and the system enters its saturated equilibrium state. (i) and (ii) are within Stage I while (iv) and (v) are within Stage II.

The concentration field $C(x,t)$ is governed by the Fick's law of diffusion:

$$D\cdot\frac{\partial^2 C(x,t)}{\partial x^2}=\frac{\partial C(x,t)}{\partial t} \qquad (6.3.1)$$

where D is the constant diffusion coefficient. The boundary condition for the concentration field is

$$C\left(x=L(t)-L_s,t\right)=C\left(x=L_s-L(t),t\right)=C_I(t) \quad (6.3.2)$$

where $x=L(t)-L_s$ is the position of the amorphous-crystalline interface, i.e., the graphene domain edge. Unlike the conventional diffusion problems with stationary

boundaries, the interface is dynamically moving outwards. Therefore, the interfacial concentration $C_I(t)$ is actually an unknown function of growth time that needs to be self-consistently determined from the diffusion-growth equations rather than a pre-initialized boundary condition that is given to solve the diffusion-growth equations. Denoting the initial homogenous hydrocarbon concentration as C_0, the initial condition for the concentration field is:

$$C(x,t=0)=\begin{cases}C_0,(-L_s<x<L_s)\\ C_I(0),(x=\pm L_s)\end{cases} \quad (6.3.3)$$

where $C_I(0)$ is the initial value of $C_I(t)$. Since nucleation partly consumes the local hydrocarbons, $C_I(0)$ should be lower than C_0 and could be zero in the extreme case when nucleation depletes all the hydrocarbons (see Figure 6.8(i)). We also assume the first-order reaction and a constant etching term for the diffusion-controlled growth. The growth rate equation can then be constructed using the mass conservation relation:

$$(\rho_G - C_I(t))\frac{dL(t)}{dt} = D\cdot\left.\frac{\partial C(x,t)}{\partial x}\right|_{x=L(t)-L_s} - E \quad (6.3.4)$$

where ρ_G is the constant area density of the crystallized carbon atoms inside graphene lattice and *E* is the constant etching rate (see Equations A2.1, A2.2, A2.3 in Appendix 2 for derivation details). The interfacial concentration $C_I(t)$ appears in both the boundary condition for the concentration distribution and the growth rate equation. This reflects the above-mentioned diffusion-growth inter-dependence.

6.3.2 Formation of the Depletion Layer

Since the interfacial hydrocarbons are depleted ahead of those on the farther Cu surface, $C_I(t)$ is expected to decrease to zero earlier than $C(x,t)$ as shown in Figure 6.8 (iii). It is worth noting that, upon the depletion of the interfacial concentration, a so-called 'depletion layer' will emerge. The depletion layer is spatially located between the graphene domain edge and the hydrocarbon concentration profile tail (see Figure 6.8(iv)) and hence can be seen as a transitional phase between the amorphous and the crystalline phase. Once the hydrocarbons have diffused into the depletion layer from the amorphous phase, they will transport across the depletion layer in an instant followed by immediate attachment onto the domain edge because k_{diff} is assumed much lower

than k_{att}. Therefore the hydrocarbon concentration inside the depletion layer remains zero. As the diffusion-growth process continues, the depletion layer is widening but the above properties preserve. The concept of the depletion layer has been raised in previous experimental research but not mathematically modelled in explicit forms hitherto.[206] From a mathematical perspective it is impossible to have physically reasonable solutions for $C(x,t)$, $C_I(t)$ and $L(t)$ without recognizing the expanding depletion layer. Therefore the depletion layer is inherent in our model.

Denoting as t_2 the moment when $C_I(t)$ reaches zero and the depletion layer appears (see Figure 6.8(iii)), the entire diffusion-growth process can be divided into two successive stages by t_2. The first stage, namely Stage I, corresponds to $0 \le t < t_2$ during which the interfacial concentration $C_I(t)$ decreases from its initial value $C_I(0)$ to zero (see Figure 6.8(i)-(iii)). The second stage, namely Stage II, corresponds to $t \ge t_2$ during which the deletion layer appears and widens (Figure 6.8(iv) and (v)). The time-dependence of the depletion layer width has to be determined by the self-consistent equations. The net domain growth rate decreases to zero when the concentration gradient at the hydrocarbon profile tail decreases to the level of the etching rate. This can be seen as the end of Stage II when the entire diffusion-growth system reaches the final equilibrium and both the domain size and the depletion layer width reach their saturated levels (see Figure 6.8 (v)). For a non-zero etching rate the hydrocarbon distribution will end with a non-zero residual profile around its centre.

A profound consequence of the formation of the depletion layer is that the evolutions of $L(t)$ and $C(x,t)$ within Stage I and Stage II are constrained by different boundary conditions. After defining the characteristic time scale $\tau = L_s^{\,2}/D$, the dimensionless position $\alpha = x/L_s$, the dimensionless time $\beta = t/\tau$, the dimensionless domain radius $l(\beta) = L(t)/L_s$ and the dimensionless etching constant $e = (L_s \cdot E)/\left(D \cdot (C_0 - C_I(0))\right)$, the equations and boundary conditions for Stage I and Stage II are accordingly transformed into their respective dimensionless forms as shown in Equations A2.4 and A2.5 in Appendix 2, where β_0 is the ending time of Stage I as well as the beginning time of Stage II, l_0 is the domain length at time β_0, and $d(\beta)$ is the time-dependent width of the depletion layer. Both β_0 and l_0 are to be determined from the Stage I equations and then used as the initial conditions for solving the Stage II equations. The

growth rate of the domain radius within Stage I is basically proportional to the hydrocarbon concentration gradient at the domain edge (α = l-1). In contrast, the edge concentration remains zero throughout Stage II and instead the corresponding growth rate is proportional to the gradient at the depletion-amorphous interface (α = l+d-1). The position of the depletion-amorphous interface is determined as the zero of the concentration profile, i.e., $C\left(l\left(\beta\right)+d\left(\beta\right)-1,\beta\right)=0$. The parameters that need to be initialized for solving $C(\alpha,\beta)$, $C_I(\beta)$, $l(\beta)$ and $d(\beta)$ are the initial concentration C_0 or equivalently its normalized quantity $\lambda_0 = C_0/\rho_G$, the initial interfacial concentration $C_I(0)$ or equivalently its normalized quantity $\lambda_I = C_I(0)/\rho_G$, and the dimensionless etching constant e.

6.3.3 Solutions to the Diffusion-controlled Growth Rate Equations

There is a unique solution to the concentration field $C(\alpha,\beta)$ satisfying the boundary conditions at both stages as shown in Equation A2.6 and A2.7 in Appendix 2. Remarkably the analytical solution for $C(\alpha,\beta)$ contains two complementary error function terms: $\mathrm{erfc}((1+\alpha)/(2\sqrt{\beta}))$ and $\mathrm{erfc}((1-\alpha)/(2\sqrt{\beta}))$. They represent the 'hydrocarbon sink' effects that are exerted on the concentration distribution by the enlarging graphene domains centred at α = -1 and α = 1, respectively. Therefore the sum of these two terms reflects how the inter-domain competitions for the hydrocarbons influence the concentration distribution, which has been ignored in previous studies considering only the growth of one single domain. Figure 6.9(a) plots the evolutionary spatial distribution of the hydrocarbon concentration at discrete time points, where the parameters are initialized at $\lambda_0 = 0.6$, $\lambda_I = 0.1$ and $e = 0.4$. The initial flat concentration profile evolves into a dome shape as the diffusion-growth proceeds. The interfacial concentration is monotonically decreasing to zero ($0 \le \beta < \beta_2$) and remains zero afterwards ($\beta \ge \beta_2$). The depletion layer appears at the beginning of Stage II ($\beta = \beta_2$) with its width, $d\left(\beta\right)$, increasing from zero. The final equilibrium state is reached at $\beta = \beta_s$ which features a non-zero residual concentration profile due to the assumed non-zero etching rate. Figure 6.9(b) shows the time-evolution of the central concentration $C\left(0,\beta\right)$ and the interfacial concentration $C_I\left(\beta\right)$ for λ_0 = 0.8, 0.6, 0.4 with λ_I fixed at 0.1 and e fixed at 0.4. Both decrease slower at smaller values of λ_0 due

to the accordingly lower concentration gradient. The central residual concentration, which is shown as the ending plateaux in Figure 6.9(b), is higher at lower λ_0 because fewer hydrocarbons are required to build smaller graphene domains.

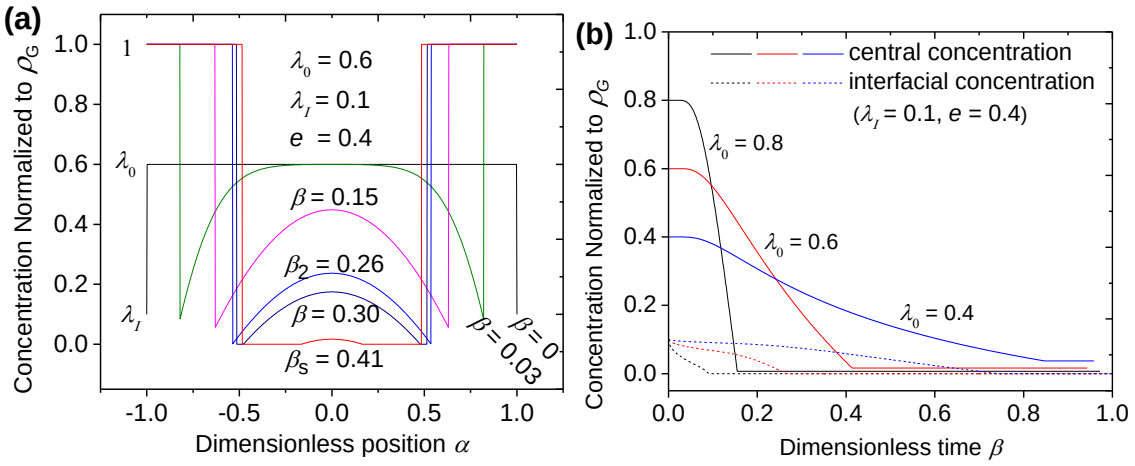

Figure 6.9: Space-time dependence of the hydrocarbon concentration field. (a) The spatial distribution of the hydrocarbon concentration at discrete time points. β_2 and β_s are the time when the system enters Stage II and the equilibrium state, respectively. (b)The time-evolution of the central concentration $C(0,\beta)$ and the interfacial concentration $C_I(\beta)$ for λ_0 = 0.8, 0.6, 0.4 with λ_I fixed at 0.1 and e fixed at 0.4.

Using the analytical solution of $C(\alpha,\beta)$, the domain growth rate equations at both stages can be expanded into the explicit forms as shown in Equation A2.8 and A2.9 in Appendix 2. The two exponential terms of the explicit rate equations represent the diffusion-driven hydrocarbon flux along the $-x$ and $+x$ directions which then feed the growth of the domain centred at α = -1 and α = 1, respectively. Their opposite signs suggest that the inter-domain competitions suppress the growth rates of each other. Therefore this model has correctly reflected the influences of the inter-domain competitions on both the diffusion process and the growth process. This is possible only after simplifying the 2D diffusion-growth problem into 1D because the original 2D system inevitably involves the complicated 2D geometric factors regarding the spatial distribution of the neighbouring domains and the domain shapes. Generally there are no analytical solutions to the growth rate equations so they have to be numerically solved.

Figure 6.10 shows the numerical solutions of the domain length and depletion layer width. Figure 6.10(a) plots the numerical $l(\beta)$ for λ_0 = 0.8, 0.6, and 0.4 with λ_I fixed at 0.1 and e fixed at 0.4. The domain radius increases with growth time during Stage I and Stage II. More specifically, as $\beta \to 0$, the time-evolution of the radius follows an

asymptotic square-root manner (see Equation A2.10 and A2.11 in Appendix 2 for derivation details):

$$l(\beta) \propto \sqrt{\beta}. \qquad (6.3.5)$$

Such a characteristic dependence originates from the essential assumption of the diffusion-controlled kinetics, i.e., $k_{diff} << k_{att}$. Notably it is essentially different from the initial time-dependence of the edge-attachment-controlled $l(\beta)$, which is found linear, $l \propto \beta$. The growth rate of $l(\beta)$ monotonically decreases and finally vanishes at the end of Stage II ($\beta \to \beta_s$) when $l(\beta)$ converges to its saturated level l_s. This should be understood as the necessary consequence of the inter-domain competition. For the special case of zero etching rate, the time β_s can be determined in the analytical form as shown in Equation A2.12 in Appendix 2. Figure 6.10(a) also shows that higher initial hydrocarbon concentration ($\lambda_0 = C_0/\rho_G$) causes not only higher growth rate but also larger saturated radius l_s and hence higher saturated coverage. Furthermore, Figure 6.10(c) shows that the saturated domain radius l_s varies almost linearly with the initial hydrocarbon concentration $\lambda_0 = C_0/\rho_G$. For the special case of zero etching rate, l_s simply equals C_0/ρ_G : $l_s = C_0/\rho_G$. This can be intuitively understood by noticing that the amount of the amorphous hydrocarbons at the initial state equals that of the crystallized hydrocarbons at the final saturated state. An equivalent mass conservation analysis of the original 2D system with zero etching shows that the saturated graphene coverage is directly proportional to the initial hydrocarbon concentration: $\Theta_s = C_0/\rho_G$. Therefore the saturated coverage is linearly proportional to the CH_4 partial pressure:

$$\Theta_s \propto P_{CH_4} \cdot \left(P_{H_2}\right)^{(x-4)/2}.$$

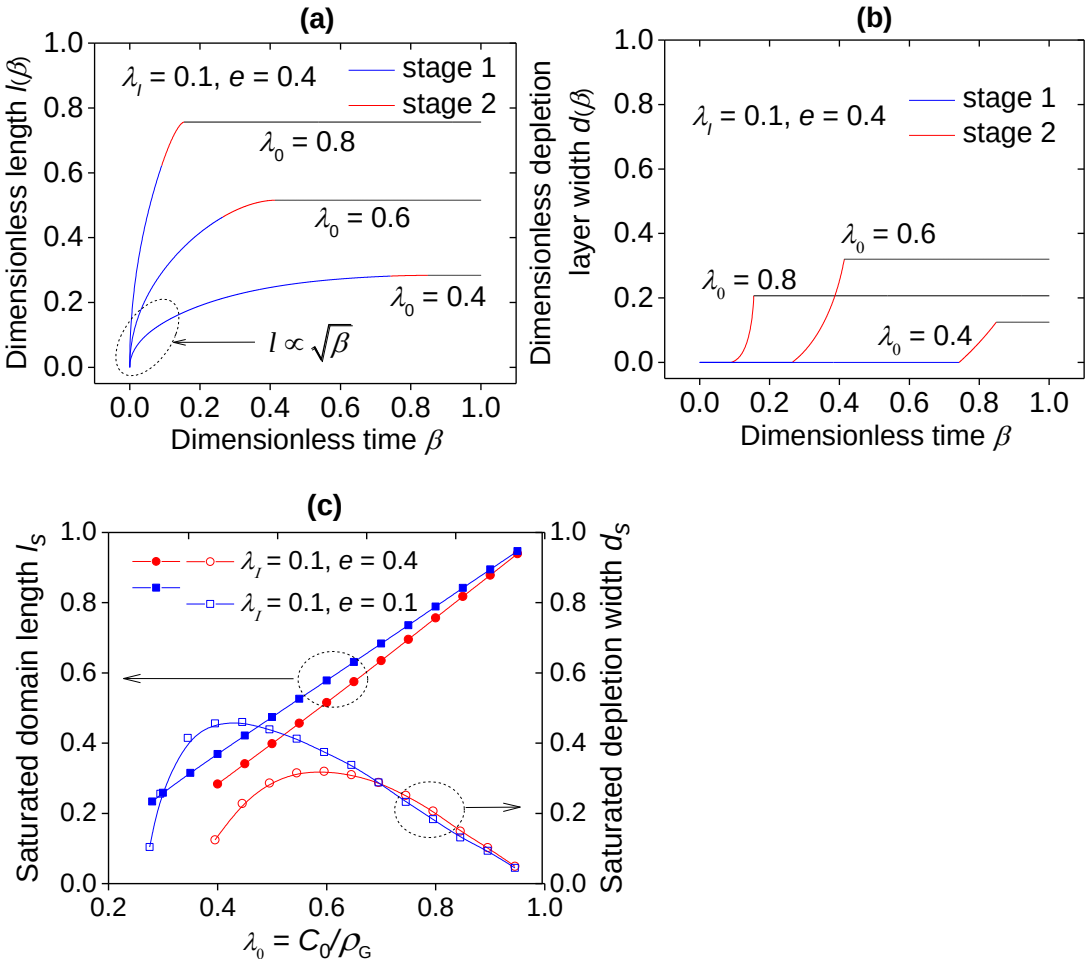

Figure 6.10: Solutions to the diffusion-growth equations. The time-dependence of (a) the domain radius $l(\beta)$ and (b) the depletion layer width $d(\beta)$ for λ_0 = 0.4, 0.6 and 0.8 with λ_I fixed at 0.1 and e fixed 0.4. (c) The dependence on the initial surface hydrocarbon concentration ($\lambda_0 = C_0/\rho_G$) of the saturated domain radius and the saturated depletion layer width for e = 0.1 and 0.4 with λ_I fixed at 0.1.

The width of the depletion layer $d(\beta)$ increases with growth time during Stage II (see Figure 6.10(b)) until it reaches its maximum value d_s. For zero etching rate d_s can be analytically determined as $d_s = 1 - l_s = 1 - C_0/\rho_G$. However, different from the domain radius $l(\beta)$, the growth rate of the depletion layer width $d(\beta)$ does not fade towards the end of Stage II. Its maximum value d_s does not vary monotonically with C_0/ρ_G. Instead Figure 6.10(c) shows a dome-shaped dependence of d_s on C_0/ρ_G. Small C_0/ρ_G results in small d_s because the diffusion-growth system reaches equilibrium before l_s and d_s can grow large. Large C_0/ρ_G results in small d_s because high graphene coverage can be achieved under large C_0/ρ_G which then suppresses the

expansion of the depletion layer. The dependence at large C_0/ρ_G regime is consistent with the conclusion of the phase-field simulations.[72] Figure 6.10(c) further shows that, for low levels of C_0/ρ_G, decreasing the etching rate can substantially increase the maximum depletion layer width d_s. This is because the diffusion-growth processes are allowed to proceed until the interfacial concentration gradient decreases to a lower level.

6.3.4 Fitting Diffusion-controlled CVD Data

The diffusion-controlled growth model can well describe a wide range of literature CVD data. As far as we know, there is no experimental data reported for the hydrocarbon concentration field $C(\alpha,\beta)$ and the depletion layer width $d(\beta)$, so we will focus on explaining the experimentally observable time-dependence of the domain radius, $l(\beta)$. Since this model predicts $l \propto \sqrt{\beta}$ as $\beta \to 0$, the initial domain area should linearly depend on the growth time: $l \propto \sqrt{\beta} \to A \propto l^2 \propto \beta$. Figure 6.11(a) shows the in situ data points of the average domain area against the growth time, i.e., *A*(*t*)-*t*, from Nie *et al*[264] where the graphene growth has been confirmed to be controlled by the surface diffusion. Fitting these data with a trial power function $A(t) \propto t^n$ gives $n = 1.08 \pm 0.02$, close to the model-predicted value of 1. The similar fitting on the in situ SEM data of Wang *et al* also finds a exponent of $n = 1.17 \pm 0.09$ (see Figure 6.11(b)).[206] Hence this model can well explain the experimentally observed linear time-evolution of the domain area at the beginning of the diffusion-controlled growth.

The power fitting is further performed on Wang's evolutionary area data of the individual domains against the number of neighbouring domains (see Figure 6.11(c)). The fitted exponent is 2.2±0.2, 2.1±0.1, 1.5±0.2 and 1.1±0.1 for the domains with 0, 1, 2 and 3 neighbours, respectively, as summarized in Figure 6.11(d). The increasing number of the neighbouring domains intensifies the inter-domain competitions for the limited surface hydrocarbons all of which could have otherwise fed the growth of one single domain. Consequently the characteristic diffusion rate becomes lower and the system turns more diffusion-controlled than edge-attachment-controlled. Therefore the variation of the fitted exponent further justifies both the diffusion-model-predicted initial linear dependence ($A \propto \beta$) and the edge-attachment-model-predicted initial

quadratic dependence ($A \propto \beta^2$). This also suggests the experimentally fitted power exponent can be used as a fingerprint for identifying the underlying kinetics.

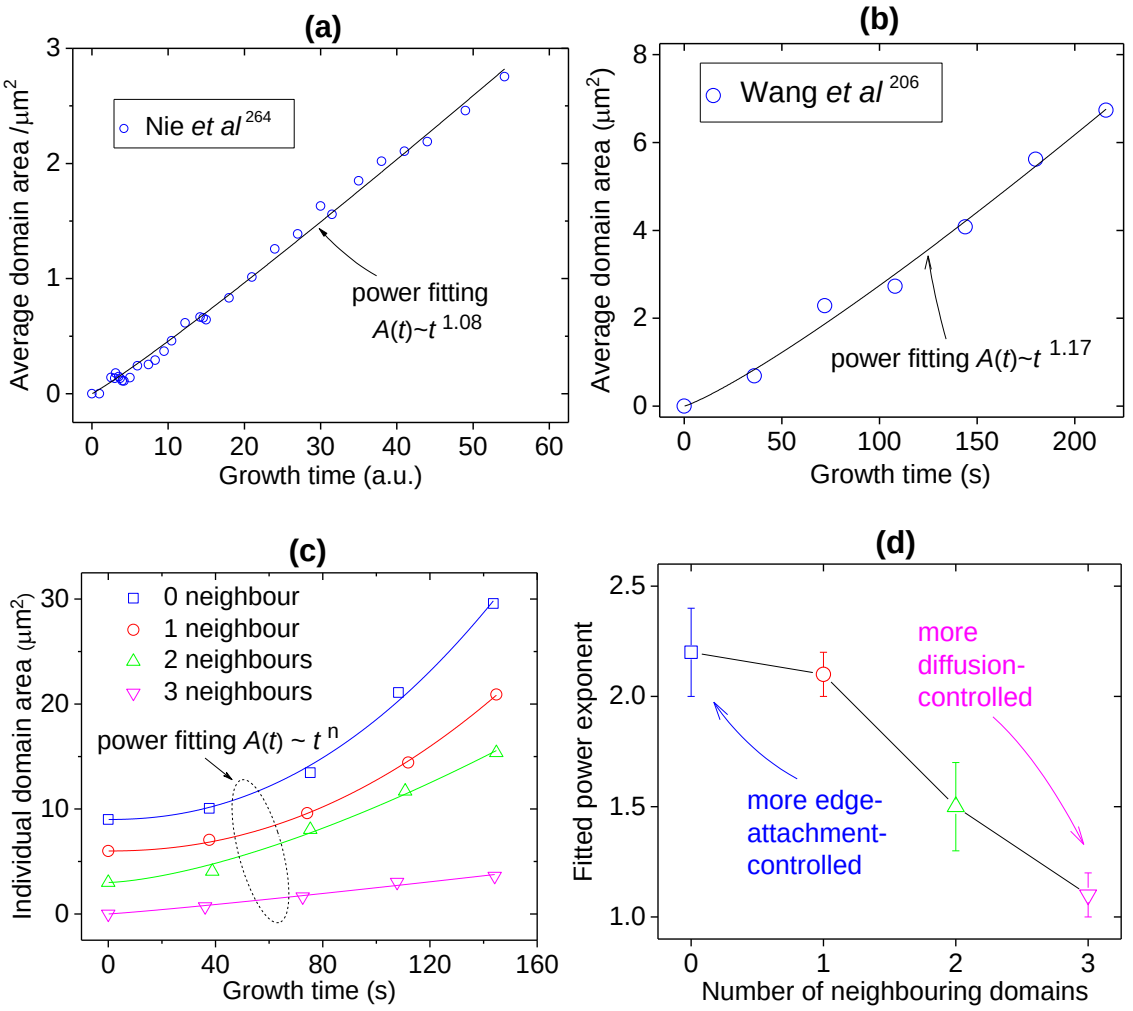

Figure 6.11: Fitting literature data using the diffusion-controlled growth model. (a) and (b) The initial dependence of the average domain area on the growth time is fitted with a power function $A(t) \propto t^{n}$. Data source: Nie *et al*,[264] and Wang *et al*,[206] respectively. (c) Power fitting of the initial time-dependences of the area sizes of the individual domains with 0, 1, 2 and 3 neighbours. The data series have been equally offset for clarity. Data source: Wang *et al*.[206] (d) Dependence of the fitted power exponent on the number of the neighbouring domains (extracted from (c)).

The full time-dependences of the single domain areas are fitted by our model as shown in Figure 6.12(a). The data points are extracted from the real time LEEM observation of graphene growth from Sutter *et al*.[254] The evolutionary domain area initially increases at an approximately constant rate which then gradually decreases to zero leading to a saturated plateaux. The original article has suggested that the evanescing growth rate is most likely caused by the inter-domain competitions for surface hydrocarbons. The etching rate constant in our modelling can be set zero since

the authors have observed no detectable domain shrinkage after terminating the carbon supply. We then set as fitting parameters the characteristic domain area A_c and the characteristic growth time t_c. They are evaluated at those that can minimize the residual-square-sum when fitting the accordingly normalized data $A/A_c - t/t_c$ against the numerical dimensionless solution. The optimal fitting is achieved under $\lambda_0 = 0.6$ and $\lambda_I = 0.1$ with A_c = 1150 μm^2 and t_c = 766 s (inset of Figure 6.12(a)). Figure 6.12(b) validates the suggested growth model on another set of $A(t)$ data,[61] which can be well described by the numerical solution under $\lambda_0 = 0.7$, $\lambda_I = 0.3$ and $e = 0$.

The above fitting analysis confirms that our model has elucidated the essential kinetics of the diffusion-controlled graphene formation. Particularly this model has proven the linear dependence of the domain area on the initial growth time and explained how the inter-domain-competition causes the time-convergence of the domain area towards the end of growth. In contrast, the previous models ignoring the inter-domain competitions are unable to explain the graphene formation processes.

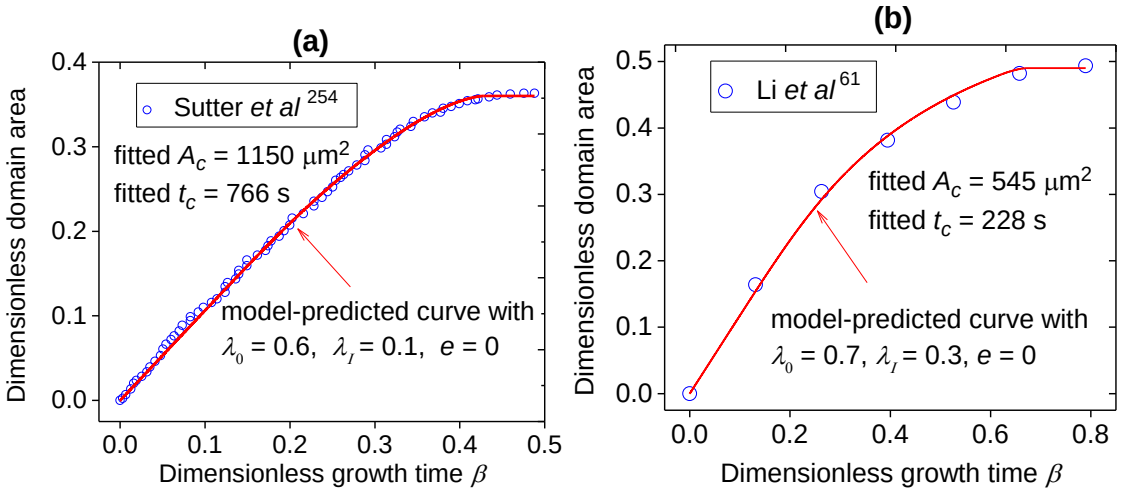

Figure 6.12: (a) The full time-dependence of the single domain area is fitted using the model-predicted solution for λ_0 = 0.6, λ_I = 0.1 and e = 0. Data source: Sutter *et al*.[254] (b) The full time-dependence of the single domain area is fitted using the model-predicted solution for λ_0 = 0.7, λ_I = 0.3 and e = 0. Data source: Li *et al*.[61]

6.4 Temperature Dependence of Graphene Growth Kinetics

Our modelling shows that there are six fundamental observables that could be temperature-dependent: (1) the domain radial growth rate, (2) the saturated domain radius, (3) the nucleation rate, (4) the saturated nucleation density, (5) the coverage growth rate, and (6) the saturated coverage. The radial growth rate can be suitably defined as the initial linear growth rate, i.e., $\lim_{t\to 0} dL/dt$, where L is the measured domain radius at the initial growth time t. The advantage of this definition is that the linear growth rate is approximately constant at low coverage, which has been rigidly proven in Section 6.2. Similarly the nucleation rate can be defined as $\lim_{t\to 0} dN/dt$. The coverage growth rate, however, has to be alternatively defined, because $\lim_{t\to 0} d\Theta/dt$ is close to zero for the S-shaped coverage-time dependence. A proper definition could be the maximum coverage growth rate $\left(d\Theta/dt\right)_{\max}$ which is normally achieved at the inflection point of the S-shaped curve.

To study the temperature dependence of the above mentioned kinetic observables, we have measured the time-evolution of the average domain sizes, nucleation density and coverage at 900 °C, 950 °C, 975 °C and 1000 °C. The results are shown in Figure 6.13(a), (b) and (c).The accordingly defined 'rate values' at each temperature as well as the saturated values are plotted against the growth temperature in Figure 6.13(d), (e) and (f). We see clearly Arrhenius-type temperature-dependences of the initial domain radial growth rate with the extracted energy barrier E_{att} = 2.9 ±0.2 eV and of the saturated domain radius with $E(L_s)$ = 2.49 ± 0.04 eV. The Arrhenius dependences are also found with the initial nucleation rate (E_{nuc} = - (3.7 ± 0.2) eV), the saturated nucleation density ($E(N_s)$ = - (4.9 ± 0.1) eV), and the maximum coverage growth rate (E_{cov} = 0.7 ± 0.1 eV). In contrast, the graphene coverage at each temperature can reach almost 100% given sufficient growth time (see Figure 6.13 (f)), and hence the apparent activation energy seems to be negligible.

The measured activation energies provide insight regarding the graphene formation mechanism. The E_{att} in our conditions (2.9 ± 0.2 eV) is close to that of Terasawa *et al* (2.7 ± 0.3 eV),[71] and roughly within the same range of Chuang *et al* (2.3 - 3.1 eV),[251] but significantly larger than some other reports (1.3 - 1.8 eV).[62,182,233] The theoretical energy barrier for the dissociative adsorption of CH_4 onto Cu surface is approximately

1.7 - 1.9 eV.[133,274,275] These are significantly lower than the measured value and hence the dissociative adsorption is unlikely rate-limiting in our conditions. The estimated

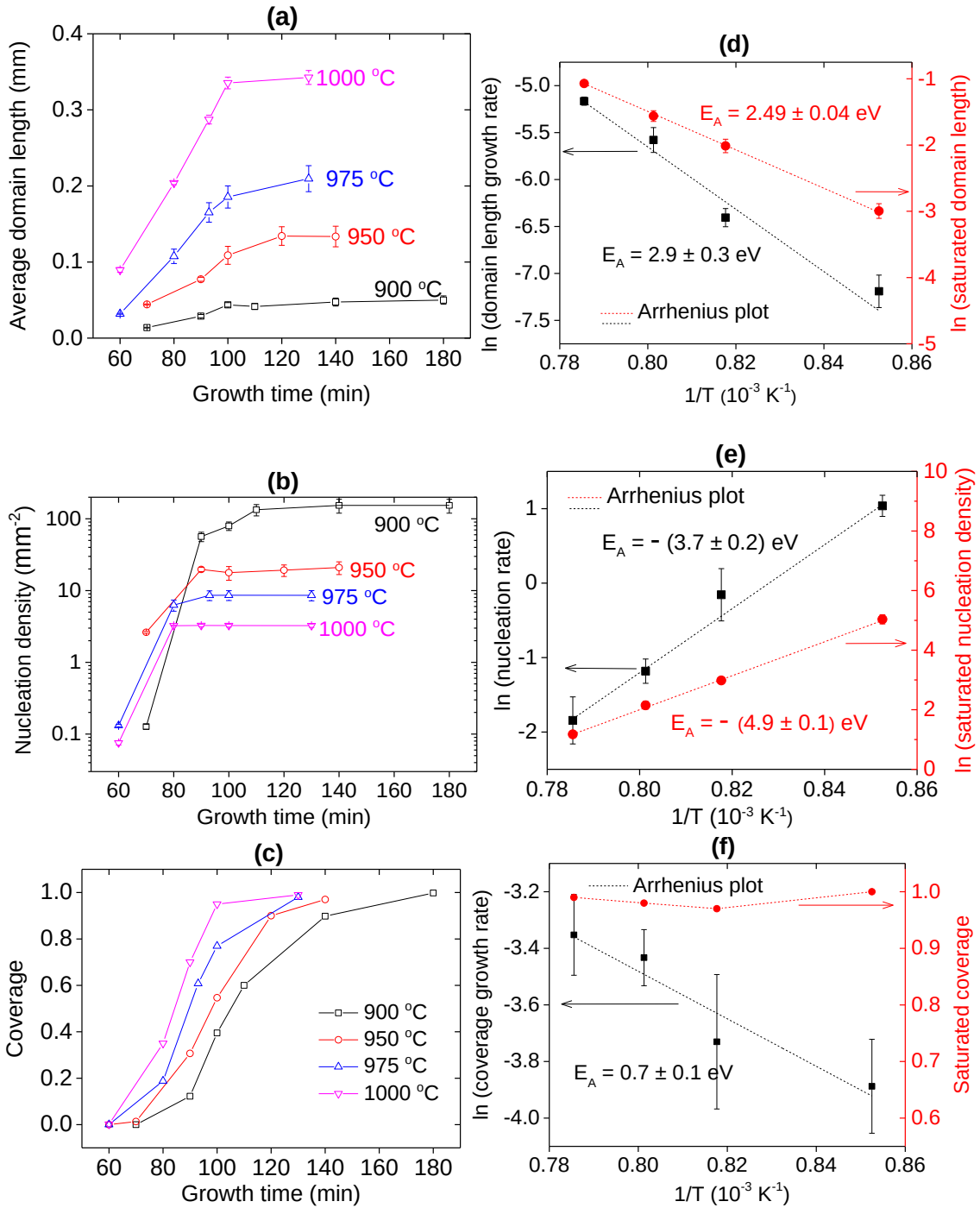

Figure 6.13: Measured time-dependences of (a) the average domain length, (b) the nucleation density, (c) coverage for ex situ CVD growth under 900 °C, 950 °C, 975 °C and 1000 °C. Extracted temperature-dependence of (d) the initial domain radius growth rate and the saturated domain radius, (e) the initial nucleation rate and the saturated nucleation density, (f) the maximum coverage growth rate and the saturated coverage. Source of the error bars: merged domains at high coverage and batch-to-batch variation.

barrier for the surface diffusion is 0.07 - 0.6 eV,[276,277] which is also much lower than our observed value. Therefore it would be logical to regard the edge attachment of the hydrocarbons as the rate-limiting step of the domain growth in our Cu-CVD conditions.

The measured values of E_{nuc} and $E(N_s)$ are negative due to lower nucleation density at higher growth temperature. This is consistent with many Cu-CVD experiments,[59,63,70,78,79,182,233,251] and hence high temperature is widely used to synthesize large graphene single crystallites by suppressing the nucleation density. To explicate the decline of the saturated nucleation density upon increasing temperature, Kim *et al* has analyzed the surface processes that compete for the hydrocarbons,[182] as shown in Figure 6.1, including (1) formation of a nucleus from the hydrocarbon itself, (2) diffusion of the hydrocarbon to be attached onto the edge of a existing nucleus, and (3) direct desorption from the Cu surface. An increase in the growth temperature causes the reduction of the nucleation density because it can lead to increase in the in the edge-attachment probability relative to the nucleation rate, which is further due to the increase in the surface mobility of the hydrocarbons (at the low temperature regime) or the hydrocarbon desorption rate (at the high temperature regime).[182] However the temperature-dependence of the nucleation density is more complicated in real Cu-CVD conditions than in theory. Vlassiouk *et al* has observed the absolute value of $E(N_s)$ is significantly lower at LPCVD than at APCVD.[63] They go on to claim that increasing temperature causes heavy Cu evaporation that also leads to successive desorption of the surface hydrocarbons rather than direct desorption of the hydrocarbons. This process is schematically represented by #4 in Figure 6.1. Meanwhile Chen *et al*[203] and Miseikis *et al*[82] have shown that suppressing the thermal Cu evaporation decreases the nucleation density by reducing the evaporation-induced surface vacancy sites, which are otherwise catalytically active. This phenomenon suggests that raising the growth temperature could also create more surface nucleation sites due to heavier Cu atom loss. In summary the measured activation energies for the nucleation rate and the saturated density reflect the collective consequences of the temperature-dependent surface processes. The fact that the measured activation energies are negative under most CVD conditions indicates the Cu-evaporation-induced density increase is generally overwhelmed by the other processes.

As for the coverage increase, the temperature seems to have negligible influence over its saturated value at least within the temperature ranges used in this research. This is

primarily because increasing the growth temperature will simultaneously increase the domain sizes and decrease the nucleation density. Vlassiouk *et al*[63] has observed the similar phenomenon over the temperature range of 950 °C to 1050 °C for both APCVD and LPCVD. Kim *et al*[183] has found only ~15% coverage increase when raising the growth temperature from 800 °C to 1000 °C.

Interestingly the five activation energies appear to be correlated rather than being independent. Given negligible temperature-dependence of the saturated coverage, in theory only the activation energy for the edge attachment E_{att} and the activation energy for the nucleation rate E_{nuc} are independent while the activation energy for the saturated domain length $E(L_s)$, the activation energy for the saturated nucleation density $E(N_s)$, and the activation energy for the coverage growth rate E_{cov} can be decomposed into their linear combinations. For the case of $p = 1$ Appendix 3 has provided a detailed proof where the energy relationships are found to be:

$$\begin{cases} E\left(L_s\right)=\dfrac{1}{3}\left(E_{att}-E_{nuc}\right) \\ E\left(N_s\right)=-\dfrac{2}{3}\left(E_{att}-E_{nuc}\right). \\ E_{cov}=\dfrac{1}{3}\left(2E_{att}+E_{nuc}\right) \end{cases}$$

For general values of p, similar arguments would lead to the generalized conclusion that and $E(L_s)$, $E(N_s)$, E_{cov} are linearly dependent on E_{att} and E_{nuc}. But unlike the case of $p = 1$, there are no closed-form expressions for their combination coefficients, which, instead, have to be numerically computed. According to the energy relationships for $p = 1$, we have calculated the theoretical values of $E(N_s)$, $E(L_s)$ and E_{cov} using the E_{att} and E_{nuc} measured from the CVD conditions in this research (see Table 6.1). The relative small discrepancy with the corresponding measured values appears to support the proposed energy relationships. The probable reason for the discrepancy could be that the actual parameter p in this research is ~0.87 instead of being exactly 1. It is difficult to test the energy relationships against literature data because most publications have not provided the complete energy values and the parameter p in their conditions is generally smaller than 1.

Table 6.1: Compare the calculated values of $E(N_s)$, $E(L_s)$ and E_{cov} to their measured values

	Measured (eV)	**Calculated (eV)**
E_{att}	2.9 ± 0.2	N/A
E_{nuc}	- (3.7 ± 0.2)	N/A
$E(L_s)$	2.49 ± 0.04	2.2 ± 0.2
$E(N_s)$	- (4.9 ± 0.1)	- (4.4 ± 0.3)
E_{cov}	0.7 ± 0.1	0.7 ± 0.2

6.5 Kinetics-controlled Domain Outlines

In Section 6.2 and 6.3 we have distinguished the edge-attachment-controlled growth versus the surface-diffusion-controlled growth and constructed kinetic models for each regime. It is natural to seek for a critical ratio to decide if a given growth is dominated by edge-attachment or surface diffusion. In real CVD experiments this is determined from the geometric characteristics of the domain outlines. Most experimental investigations regard the compact outlines as fingerprints of the edge-attachment-controlled growths and the dendritic outlines as fingerprints of the diffusion-controlled growth.[62,66,198,253,278,279] The phase-field simulations have been applied to explain such kinetics-dependent outline formation.[62,66,72] We will demonstrate in the coming discussions that our models can provide an equivalent explanation. But for the moment we will derive a theoretical formula for such a critical ratio. Assuming the concentration of the hydrocarbon at the domain edge is C_I, Equation 6.2.1 and 6.3.4 suggest that the hydrocarbon fluxes brought by the attachment process and the surface diffusion process are respectively:

$$\begin{cases} J_{att} \approx k_{att} \cdot C_I \\ J_{diff} \approx \dfrac{1}{\rho_G - C_I} \cdot D \cdot \left.\dfrac{\partial C}{\partial x}\right|_{\text{edge}} \approx \dfrac{1}{\rho_G - C_I} \cdot D \cdot \dfrac{C_0 - C_I}{L_s} \cdot \end{cases}$$

These two fluxes should be equal at the steady state: $J_{att} = J_{diff}$, from which the domain edge concentration can be approximately solved: $C_I \approx C_0 D/(k_{att}\rho_G L_s + D)$. Defining $k_{diff} \approx D/(\rho_G L_s)$, the steady state hydrocarbon flux is thus:

$$J = J_{att} = J_{diff} \approx \frac{C_0}{\frac{1}{k_{att}} + \frac{1}{k_{diff}}}.$$

This expression suggests that the above defined k_{diff} is the right characteristic surface diffusion rate. Therefore the desired critical ratio should be $k_{att}/k_{diff} \approx k_{att}\rho_G L_s/D$. The graphene growth is dominated by the edge-attachment process if $k_{att} << k_{diff}$ and by the surface diffusion process if $k_{att} >> k_{diff}$. The value of the critical ratio is closely related to the CVD process parameters since k_{att} and D are Arrhenius dependent on the growth temperature: k_{att}~exp(-E_{att}/k_BT), D~exp(-E_{diff}/k_BT). Yet in the real CVD experiments the forming gas pressure P_{CH_4} and P_{H_2} prove to have more profound effects in controlling the rate-limiting step. For instance, Jacobberger and Arnold[67] as well as Meca *et al*[66] have found that increasing H_2:CH_4 results in a shift from the diffusion-controlled to the edge-attachment-controlled growth. According to our model this trend might be attributed to the dependence of the diffusion coefficient D on the Cu surface chemical states. The increase of P_{H_2} causes the increase of the surface-adsorbed H concentration. It could be easier for the hydrocarbon species to diffuse on the Cu surface with more H adsorbed than CH_x adsorbed. However to confirm this DFT studies are needed to provide conclusive evidence which is beyond the scope of this research.

We now derive the domain outline formation from the established growth models. The 1D kinetic equations established in section 6.2 and 6.3 have not incorporated any geometric factors so the analysis needs to be based on the 2D equations. For the edge-attachment-controlled growth, the domain radius in the general 2D systems should be assumed to be orientation-dependent, i.e., $L(\theta,t)$, and the corresponding 2D nucleation-growth coupled equations could be constructed in the polar coordinates. Equation A4.1 in Appendix 4 have provided the explicit forms of the 2D equations where $A(t)$ is the domain area, $k_{att}(\theta)$ and $k_{growth\_etch}(\theta)$ are respectively the anisotropic rates of the edge attachment and edge etching. $F(\theta)$, the given initial domain outline, can be assumed to be arbitrarily irregular and consequently the initial domain has mixed types of graphene edges (see Figure 6.14 (i)). Artyukhov *et al*[95] and Ma *et al* [273]have shown that both the attachment rate (k_{att}) and the etching rate (k_{growth_etch}) of a graphene edge is proportional

to the concentration of the kink sites along the edge. Thereby k_{att} and k_{growth_etch} have similar dependence on the slanted angle of the edge, φ , relative to the zigzag orientation (φ should be distinguished from the polar coordinate angle θ):

$$\begin{cases} k_{att} \\ k_{growth\_etch} \end{cases} \propto \begin{cases} \frac{2}{3}\frac{\sin(\varphi)}{a_{C-C}}, & \text{for } 0^{o} < \varphi < 19.107^{o} \\ 2\sqrt{3}\frac{\sin(\varphi)}{a_{C-C}}, & \text{for } 19.107^{o} < \varphi < 30^{o} \end{cases},$$

where a_{C-C} = 0.142 nm is the C-C bond length in graphene lattice.[273] Obviously the zigzag edge (φ = 0) has the smallest attachment rate and smallest etching rate, and hence, according to the 2D kinetic equations, the smallest net growth rate. As the domain enlarges, the total length of the zigzag edges will increase while the other slanted edges will shorten due to their higher net growth rates (see Figure 6.14 (i)). Eventually the initial irregular domain with mixed edges will be transformed into a compact hexagonal domain with all-zigzag edges dominating its circumference (see Figure 6.14 (ii)). This process is the so-called kinetic Wulff construction (kWC) which has been used to address the shape formation of a single graphene domain.[93,95,280] The novelty of the analysis in this part is that the isotropic concentration term $C_0 - \rho_G \cdot N(t) \cdot A(t)$ in the 2D equations has justified the applicability of the kWC to the competitive growth of the multiple domains with the nucleation-growth convolution. This is reasonable because the surface diffusion, which has already been assumed much faster than the edge attachment, maintains a homogenous hydrocarbon concentration at any time. Once all of the domain edges have evolved into zigzag, the compact hexagonal outline will be preserved as the domain continues to grow because all of its zigzag edges are now propagating outward at the same net rates (see Figure 6.14(iii)).

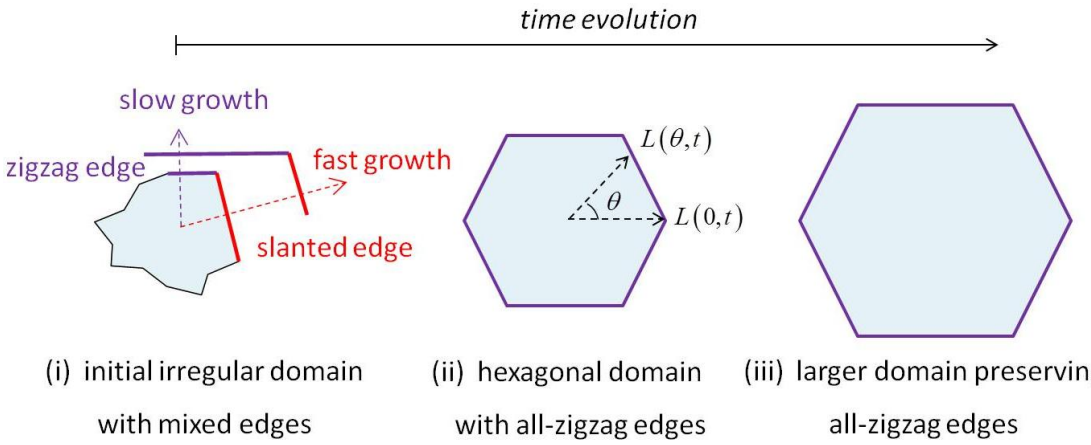

Figure 6.14: Schematic illustration for the formation of the compact domain outlines driven by the edge-attachment-controlled kinetics. (i) Initial irregular domain outline consisting of mixed edges. Purple and red lines represent the zigzag edge and an arbitrarily slanted edge. (ii) Formation of a compact hexagonal domain with all-zigzag edges via the kWC after sufficient growth time. $L(\theta,t)$ is the time-dependent domain radius along an arbitrary orientation θ while $L(0,t)$ is that along the [2 1 1 0] orientation. (iii) The compact domain enlarges with time preserving its all-zigzag edges.

For the diffusion-controlled growth, the corresponding 2D kinetic equations are also provided in Equation A4.2 in Appendix 4, where $\vec{r}=(r,\theta)$ is the position vector in the polar coordinates, ∇^2 is the 2D Laplace operator, $\vec{g}$ is the unit vector along the θ-orientation and $\partial C(\vec{r},t)/\partial \vec{g}\big|_{\vec{r}=(L(\theta,t),\theta)}$ is the directional derivative of the concentration field $C(\vec{r},t)$ along $\vec{g}$ at the position of $\vec{r}=(L(\theta,t),\theta)$. Of particular importance is the diffusion coefficient $D(\theta)$ which is explicitly orientation-dependent for the 2D case. Jung *et al*[281] has shown by the DFT calculations that the energy barriers for the surface diffusion of the carbon adatoms are anisotropic depending on the Cu facets. Taking Cu (100) as an instance (see Figure 6.15), the energy barrier for the carbon diffusion along the A-orientation is ~1.0 eV lower than that along the B-orientation and hence the diffusion coefficient along A, $D(\theta_A=0)$, is significantly larger than that along B, $D(\theta_B=\pi/4)$ (roughly three orders of magnitude difference under typical growth temperature of 1000 ℃). As there are multiple diffusion pathways equivalent to A and B, the anisotropic diffusion coefficient can be modelled as:

$$D(\theta)=D_0\cdot\left(1+\varepsilon\cos(n\theta)\right)$$

where D_0 represents the average magnitude of the diffusion coefficient, ε determines the strength of anisotropy and n is the order of rotational symmetry depending on the Cu

facets. Zero ε corresponds to the completely isotropic diffusion while larger ε represents intensified diffusion anisotropy. n should be evaluated at 4 for Cu facets with four-fold symmetry such as Cu (100) and 6 for those with six-fold symmetry such as Cu(111).

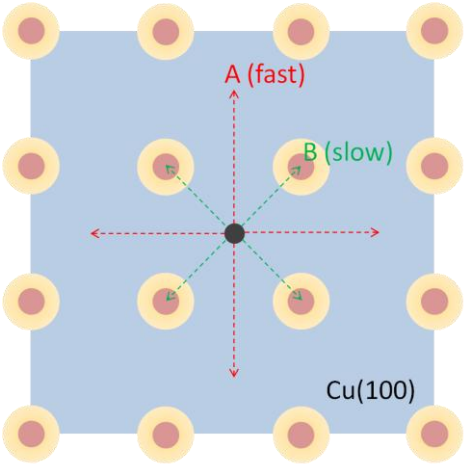

Figure 6.15: Schematic illustration for the anisotropic diffusion of the carbon atoms on Cu(100). Solid red circles surrounded by yellow circles represent the surface Cu atoms. The light blue area is regions with depleted electron density. The black circle represents the carbon atoms. The dashed red and green arrows represent the faster and slower diffusion directions for the carbon atoms, respectively. Adjusted from Jung *et al.*[281]

There are no analytical solutions to the 2D diffusion-growth equations due to the existence of the anisotropy term $\varepsilon\cos(n\theta)$. Yet half-quantitative analysis based on the equations is able to illustrate the evolution of the domain outlines. The initial concentration field and the initial interface concentration can be set homogenous, i.e., $C\left(\vec{r},t=0\right)=C_0$ and $C_I\left(\theta,t=0\right)=C_I\left(0\right)$. The initial nucleus can be assumed to be circular since it is small, i.e., $L\left(\theta,t=0\right)=L_0\ll L_s$ where L_s is the average distance between the nearest neighbouring nucleus (see Figure 6.16(i)). The detailed analysis in Appendix 4 shows that the nucleus grows faster along the A-equivalent orientations than along the B-equivalent orientations upon the onset of diffusion. The anisotropy of the diffusion-driven growth rate will lead to the anisotropy of the domain shape. The initial circular domain outline consequently becomes elongated along the fast-orientation relative to along the slow-orientation as shown in Figure 6.16(ii). Such a growth rate anisotropy can be continuously maintained since the anisotropy of diffusion further leads to the anisotropy of the hydrocarbon concentration field (see Appendix 4 for detailed derivation). Figure 6.16(iii) illustrates its further consequence. The major

branches along the A-orientations grow wider and larger. More noticeably, new side branches are expected to emerge near the tip along the A-orientations because the growth rate anisotropy exists all around the domain circumference. The entire domain now exhibits a primary level of fractal. The kinetic equations dictate that the growth rate anisotropy lasts for the entire growth process. Hence new lower-level side branches appear along the A-orientations as the existing branches continue to grow, which intensifies the level of fractal (see Figure 6.16(iv)). Eventually the anisotropic diffusion-growth kinetics drives the domain to evolve into a dendrite. Some of the neighbouring side branches merge as they grow larger and closer. This will consequently leave some symmetrically distributed voids, i.e., uncovered metal substrates, surrounded by the normal graphene lattice, which has been observed in growth of the dendritic graphene domains.[66]

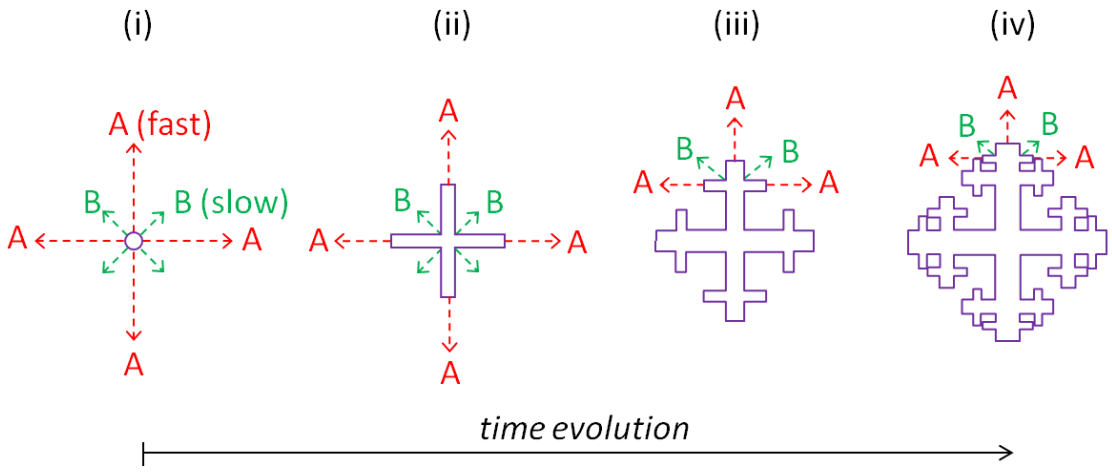

Figure 6.16: Schematic illustration for the formation of the dendritic domain outlines driven by the diffusion-controlled kinetics for the case of four-fold rotational symmetry. (i) The initial nucleus is assumed to be circular. A and B denotes the orientations of fast and slow diffusion/growth, respectively. (ii) The domain outline evolves into anisotropic upon diffusion and growth. (iii) Anisotropic domain outline with a primary level of fractal. (iv) Dendritic domain with an advanced level of fractal.

6.6 Conclusion

This work has formulated a quantitative model enabling a unified understanding of the essential kinetics of the general self-limiting graphene CVD processes. The novelty of this work is that it has revealed how the inter-domain competitions crucially impact the evolutionary graphene formation and hence become indispensable for understanding a

variety of kinetic phenomenon. For the edge-attachment-controlled growth with the most general continuous nucleation, the inter-domain competition induces the nucleation-growth convolution which influences the time-evolution of the graphene domain size, nucleation density and coverage. As the convolution intensity varies depending on the CVD process parameters, incorporating the corresponding convolution intensity enables this model to fit an enormous variety of kinetic data obtained under a wide range of growth conditions. Besides, this research has discovered that the graphene formation with general convolution intensity actually undergoes two evolution stages with different kinetics. The current models assuming zero convolution deal with only one of them without realizing the existence of the other. This model provides intuitive explication for the frequently observed linearity of $L(t)$ and $N(t)$ at the onset of growth as well as the S-shaped $\Theta(t)$. For the diffusion-controlled growth, this model shows that the graphene growth is fully coupled with the hydrocarbon diffusion. The initial domain radius is proven to increase with time in the square-root manner. Combined with its edge-attachment-controlled counterpart, the fitted power exponent of the initial radius-time dependence can be used as a fingerprint to identify the rate-limiting step of the general CVD processes. The convergence of the domain radius after sufficient growth time, which is ignored in previous models, has been quantitatively explained by the inter-domain competitions in our model. This model has further discovered the formation of the depletion layer. The kinetic features of the evolution of the depletion layer have been analyzed from a more quantitative and complete perspective than current knowledge. The critical ratio $k_{att}/k_{diff} \approx k_{att}\rho_G L_s/D$ is proposed to correlate the rate-limiting step to the CVD process parameters. In the edge-attachment-controlled and the diffusion-controlled regime, a half-quantitative analysis based on this model has illustrated the formation of compact and dendritic graphene domain outlines, respectively. The conclusions of this model are equivalent to those of the phase-field simulations. But the method of this work is physically more intuitive and mathematically more approachable than the phase-field simulations.

7 CONCLUSIONS AND OUTLOOK

This research was intended to advance the current graphene CVD technology, including the synthesis process optimization, the domain boundary visualisation, and the reaction kinetics modelling, towards an industrial-production-worth level.

In terms of the first question, the systematic optimization of the Cu-CVD method has lead to the synthesis of the high quality monolayer graphene which simultaneously satisfies three requirements: (1) full coverage, (2) millimetre-scale domain sizes and (3) strictly ensured process safety. Compared to the previous Cu-CVD recipes, this work is significantly more devoted to curing the pain points of the graphene manufacturers and hence potentially more applicable to the future large scale production. But the proposed CVD growth is still static. One avenue for further study would be to transform this technology into a R2R production manner without comprising the achieved properties. This should be feasible since the static growth technology has already controlled the concentration of the flammable gases below the LEL, which is necessary in a truly R2R CVD system.

The second part of this research has established a novel OM-based characterization technique that can spatially visualise the Cu-CVD graphene domains and domain boundaries. The principle of this visualisation method is distinctive in that it captures and utilizes the intrinsic morphologic features of the graphene-Cu interfaces. As a result this method is non-destructive to the sample graphene, a prominent advantage compared to the existing visualisation technologies. This research has also discovered a wealth of

Cu-facet-dependent graphene morphologic patterns, which implies the complex graphene-Cu interaction during the CVD process deserves deeper studies. One potential application of this visualisation technique in the future graphene-related industrial integration is to non-destructively locate the domain boundaries of the large area continuous graphene and identify the boundary-affected device units. However the proposed visualisation protocol is limited to the Cu-catalyzed CVD graphene with observable Cu evaporation. It is important to improve the design of the detection tool so that the case of little Cu evaporation is also covered.

The last section of this research has built a theoretical model for describing the kinetics of the self-limiting CVD graphene formation processes. The modelling shows the continuous nucleation and the inter-domain competition have non-trivial influences on the time evolution of the graphene nucleation density, domain size and coverage, but they are neglected by the previous investigations. The model has inherited some of the reasonable assumptions of the previous theoretical work. But the explicit treatment of the continuous nucleation and the inter-domain competition has enabled universal fitting of a much broader range of CVD kinetic data than the previous work. The model could be used as a guide to monitor the time-dependence of the graphene formation and to promote better control of the future mass production process. The conclusions derived from this model can explain the real CVD processes such as the dependence of graphene coverage and nucleation density on CH_4 partial pressure. Part of this research suggests the energy barriers associated with the self-limiting graphene formation could be internally dependent. Further research into this topic might find conclusive arguments from the first-principle calculations of the involved processes. This model also provides an alternative understanding of the kinetics-controlled formation of the graphene domain outlines with characteristic geometry.

REFERENCES

1. Novoselov, K. S. *et al.* Electric Field Effect in Atomically Thin Carbon Films. *Science* **306,** 666–669 (2004).
2. Geim, A. K. Graphene: Status and Prospects. *Science* **324,** 1530–1534 (2009).
3. Peierls, R. Quelques Propriétés Typiques des Corps Solides. *Ann. Inst. Henri Poincaré* **5,** 177–222 (1935).
4. Landau, L. Zur Theorie der Phasenumwandlungen II. *Phys Z Sowjetunion* **11,** 26–35 (1937).
5. Ferrari, A. C. *et al.* Science and Technology Roadmap for Graphene, Related Two-Dimensional Crystals, and Hybrid Systems. *Nanoscale* **7,** 4598–4810 (2015).
6. Schwierz, F. Graphene Transistors. *Nat. Nanotechnol.* **5,** 487–496 (2010).
7. Lin, Y.-M. *et al.* Wafer-Scale Graphene Integrated Circuit. *Science* **332,** 1294–1297 (2011).
8. Novoselov, K. S. *et al.* Two-dimensional Gas of Massless Dirac Fermions in Graphene. *Nature* **438,** 197–200 (2005).
9. Levendorf, M. P., Ruiz-Vargas, C. S., Garg, S. & Park, J. Transfer-Free Batch Fabrication of Single Layer Graphene Transistors. *Nano Lett.* **9,** 4479–4483 (2009).
10. Lin, Y.-M. *et al.* Operation of Graphene Transistors at Gigahertz Frequencies. *Nano Lett.* **9,** 422–426 (2009).

11. Lin, Y.-M. *et al.* 100-GHz Transistors from Wafer-Scale Epitaxial Graphene. *Science* **327,** 662–662 (2010).

12. Bonaccorso, F., Sun, Z., Hasan, T. & Ferrari, A. C. Graphene Photonics and Optoelectronics. *Nat. Photonics* **4,** 611–622 (2010).

13. Schedin, F. *et al.* Detection of Individual Gas Molecules Adsorbed on Graphene. *Nat. Mater.* **6,** 652–655 (2007).

14. Dan, Y., Lu, Y., Kybert, N. J., Luo, Z. & Johnson, A. T. C. Intrinsic Response of Graphene Vapor Sensors. *Nano Lett.* **9,** 1472–1475 (2009).

15. Pumera, M. Graphene in Biosensing. *Mater. Today* **14,** 308–315 (2011).

16. Hill, E. W., Vijayaragahvan, A. & Novoselov, K. Graphene Sensors. *IEEE Sens. J.* **11,** 3161–3170 (2011).

17. Mohanty, N. & Berry, V. Graphene-Based Single-Bacterium Resolution Biodevice and DNA Transistor: Interfacing Graphene Derivatives with Nanoscale and Microscale Biocomponents. *Nano Lett.* **8,** 4469–4476 (2008).

18. Ohno, Y., Maehashi, K., Yamashiro, Y. & Matsumoto, K. Electrolyte-Gated Graphene Field-Effect Transistors for Detecting pH and Protein Adsorption. *Nano Lett.* **9,** 3318–3322 (2009).

19. Li, X. *et al.* Transfer of Large-Area Graphene Films for High-Performance Transparent Conductive Electrodes. *Nano Lett.* **9,** 4359–4363 (2009).

20. Kim, K. S. *et al.* Large-scale Pattern Growth of Graphene Films for Stretchable Transparent Electrodes. *Nature* **457,** 706–710 (2009).

21. Kobayashi, T. *et al.* Production of a 100-m-long High-Quality Graphene Tansparent Conductive Film by Roll-to-Roll Chemical Vapor Deposition and Transfer Process. *Appl. Phys. Lett.* **102,** 023112 (2013).

22. Brownson, D. A. C., Kampouris, D. K. & Banks, C. E. An Overview of Graphene in Energy Production and Storage Applications. *J. Power Sources* **196,** 4873–4885 (2011).

23. Liu, Y., Xue, J. S., Zheng, T. & Dahn, J. R. Mechanism of Lithium Insertion in Hard Carbons Prepared by Pyrolysis of Epoxy Resins. *Carbon* **34,** 193–200 (1996).

24. Yoo, E. *et al.* Large Reversible Li Storage of Graphene Nanosheet Families for Use in Rechargeable Lithium Ion Batteries. *Nano Lett.* **8,** 2277–2282 (2008).

25. Pan, D. *et al.* Li Storage Properties of Disordered Graphene Nanosheets. *Chem. Mater.* **21,** 3136–3142 (2009).

26. Stoller, M. D., Park, S., Zhu, Y., An, J. & Ruoff, R. S. Graphene-Based Ultracapacitors. *Nano Lett.* **8,** 3498–3502 (2008).

27. Srinivas, G. *et al.* Synthesis of Graphene-like Nanosheets and Their Hydrogen Adsorption Capacity. *Carbon* **48,** 630–635 (2010).

28. Dikin, D. A. *et al.* Preparation and Characterization of Graphene Oxide Paper. *Nature* **448,** 457–460 (2007).

29. Yan, C. *et al.* Mechanical and Environmental Stability of Polymer Thin-Film-Coated Graphene. *ACS Nano* **6,** 2096–2103 (2012).

30. Palermo, V. Not A Molecule, Not A Polymer, Not A Substrate… the Many Faces of Graphene As A Chemical Platform. *Chem. Commun.* **49,** 2848–2857 (2013).

31. Jang, B. Z. & Zhamu, A. Processing of Nanographene Platelets (NGPs) and NGP Nanocomposites: a Review. *J. Mater. Sci.* **43,** 5092–5101 (2008).

32. Lahiri, J., Lin, Y., Bozkurt, P., Oleynik, I. I. & Batzill, M. An Extended Defect in Graphene as A Metallic Wire. *Nat. Nanotechnol.* **5,** 326–329 (2010).

33. Banhart, F., Kotakoski, J. & Krasheninnikov, A. V. Structural Defects in Graphene. *ACS Nano* **5,** 26–41 (2011).

34. Hashimoto, A., Suenaga, K., Gloter, A., Urita, K. & Iijima, S. Direct Evidence For Atomic Defects In Graphene Layers. *Nature* **430,** 870–873 (2004).

35. Yazyev, O. V. & Louie, S. G. Electronic Transport in Polycrystalline Graphene. *Nat. Mater.* **9,** 806–809 (2010).

36. Ugeda, M. M. *et al.* Electronic and Structural Characterization of Divacancies in Irradiated Graphene. *Phys. Rev. B* **85,** 121402 (2012).

37. Krasheninnikov, A. V. & Nieminen, R. M. Attractive Interaction Between Transition-Metal Atom Impurities And Vacancies In Graphene: A First-Principles Study. *Theor. Chem. Acc.* **129,** 625–630 (2011).

38. Emtsev, K. V. *et al.* Towards Wafer-Size Graphene Layers by Atmospheric Pressure Graphitization of Silicon Carbide. *Nat. Mater.* **8,** 203–207 (2009).

39. Emtsev, K. V., Speck, F., Seyller, T., Ley, L. & Riley, J. D. Interaction, Growth, and Ordering of Epitaxial Graphene on SiC{0001} Surfaces: A Comparative Photoelectron Spectroscopy Study. *Phys. Rev. B* **77,** 155303 (2008).

40. Maragó, O. M. *et al.* Brownian Motion of Graphene. *ACS Nano* **4,** 7515–7523 (2010).

41. Lotya, M. *et al.* Liquid Phase Production of Graphene by Exfoliation of Graphite in Surfactant/Water Solutions. *J. Am. Chem. Soc.* **131,** 3611–3620 (2009).

42. Hasan, T. *et al.* Solution-Phase Exfoliation of Graphite for Ultrafast Photonics. *Phys. Status Solidi B* **247,** 2953–2957 (2010).

43. Lotya, M., King, P. J., Khan, U., De, S. & Coleman, J. N. High-Concentration, Surfactant-Stabilized Graphene Dispersions. *ACS Nano* **4,** 3155–3162 (2010).

44. Hernandez, Y. *et al.* High-Yield Production of Graphene by Liquid-Phase Exfoliation of Graphite. *Nat. Nanotechnol.* **3,** 563–568 (2008).

45. Hassoun, J. *et al.* An Advanced Lithium-Ion Battery Based on a Graphene Anode and a Lithium Iron Phosphate Cathode. *Nano Lett.* **14,** 4901–4906 (2014).

46. Blake, P. *et al.* Graphene-Based Liquid Crystal Device. *Nano Lett.* **8,** 1704–1708 (2008).

47. Khan, U., O'Neill, A., Lotya, M., De, S. & Coleman, J. N. High-Concentration Solvent Exfoliation of Graphene. *Small* **6,** 864–871 (2010).

48. Torrisi, F. *et al.* Inkjet-Printed Graphene Electronics. *ACS Nano* **6,** 2992–3006 (2012).

49. Coraux, J., N'Diaye, A. T., Busse, C. & Michely, T. Structural Coherency of Graphene on Ir(111). *Nano Lett.* **8,** 565–570 (2008).

50. Ramón, M. E. *et al.* CMOS-Compatible Synthesis of Large-Area, High-Mobility Graphene by Chemical Vapor Deposition of Acetylene on Cobalt Thin Films. *ACS Nano* **5,** 7198–7204 (2011).

51. Reina, A. *et al.* Large Area, Few-Layer Graphene Films on Arbitrary Substrates by Chemical Vapor Deposition. *Nano Lett.* **9,** 30–35 (2009).

52. Orofeo, C. M., Ago, H., Hu, B. & Tsuji, M. Synthesis of Large Area, Homogeneous, Single Layer Graphene Films by Annealing Amorphous Carbon on Co and Ni. *Nano Res.* **4,** 531–540 (2011).

53. Li, X. *et al.* Large-Area Synthesis of High-Quality and Uniform Graphene Films on Copper Foils. *Science* **324,** 1312–1314 (2009).

54. Vlassiouk, I. *et al.* Large Scale Atmospheric Pressure Chemical Vapor Deposition of Graphene. *Carbon* **54,** 58–67 (2013).

55. Zhong, G. *et al.* Growth of Continuous Graphene by Open Roll-to-Roll Chemical Vapor Deposition. *Appl. Phys. Lett.* **109,** 193103 (2016).

56. Polsen, E. S., McNerny, D. Q., Viswanath, B., Pattinson, S. W. & Hart, A. J. High-Speed Roll-to-Roll Manufacturing of Graphene Using a Concentric Tube CVD Reactor. *Sci. Rep.* **5,** 10257 (2015).

57. Deokar, G. *et al.* Towards High Quality CVD Graphene Growth and Transfer. *Carbon* **89,** 82–92 (2015).

58. Lee, H. C. *et al.* Facet-Mediated Growth of High-Quality Monolayer Graphene on Arbitrarily Rough Copper Surfaces. *Adv. Mater.* **28,** 2010–2017 (2016).

59. Zhou, H. *et al.* Chemical Vapour Deposition Growth of Large Single Crystals of Monolayer and Bilayer Graphene. *Nat. Commun.* **4,** 2096 (2013).

60. Hofmann, S., Braeuninger-Weimer, P. & Weatherup, R. S. CVD-Enabled Graphene Manufacture and Technology. *J. Phys. Chem. Lett.* **6,** 2714–2721 (2015).

61. Li, X. *et al.* Graphene Films with Large Domain Size by a Two-Step Chemical Vapor Deposition Process. *Nano Lett.* **10,** 4328–4334 (2010).

62. Hao, Y. *et al.* The Role of Surface Oxygen in the Growth of Large Single-Crystal Graphene on Copper. *Science* **342,** 720–723 (2013).

63. Vlassiouk, I. *et al.* Graphene Nucleation Density on Copper: Fundamental Role of Background Pressure. *J. Phys. Chem. C* **117,** 18919–18926 (2013).

64. Geng, D. *et al.* Controlled Growth of Single-Crystal Twelve-Pointed Graphene Grains on a Liquid Cu Surface. *Adv. Mater.* **26,** 6423–6429 (2014).

65. Geng, D. *et al.* Uniform Hexagonal Graphene Flakes and Films Grown on Liquid Copper Surface. *Proc. Natl. Acad. Sci.* **109,** 7992–7996 (2012).

66. Meca, E., Lowengrub, J., Kim, H., Mattevi, C. & Shenoy, V. B. Epitaxial Graphene Growth and Shape Dynamics on Copper: Phase-Field Modeling and Experiments. *Nano Lett.* **13,** 5692–5697 (2013).

67. Jacobberger, R. M. & Arnold, M. S. Graphene Growth Dynamics on Epitaxial Copper Thin Films. *Chem. Mater.* **25,** 871–877 (2013).

68. Wu, B. *et al.* Self-organized Graphene Crystal Patterns. *NPG Asia Mater.* **5,** e36 (2013).

69. Artyukhov, V. I., Liu, Y. & Yakobson, B. I. Equilibrium at the Edge and Atomistic Mechanisms of Graphene Growth. *Proc. Natl. Acad. Sci.* **109,** 15136–15140 (2012).

70. Safron, N. S. & Arnold, M. S. Experimentally determined model of atmospheric pressure CVD of graphene on Cu. *J Mater Chem C* **2,** 744–755 (2014).

71. Terasawa, T. & Saiki, K. Radiation-Mode Optical Microscopy on the Growth of Graphene. *Nat. Commun.* **6,** 6834 (2015).

72. Xu, X. *et al.* Ultrafast Growth of Single-Crystal Graphene assisted by a Continuous Oxygen Supply. *Nat. Nanotechnol.* **11,** 930–935 (2016).

73. Wu, T. *et al.* Fast Growth of Inch-Sized Single-Crystalline Graphene from a Controlled Single Nucleus on Cu-Ni Alloys. *Nat. Mater.* **15,** 43–47 (2016).

74. Huang, P. Y. *et al.* Grains And Grain Boundaries In Single-Layer Graphene Atomic Patchwork Quilts. *Nature* **469,** 389–392 (2011).

75. Kim, K. *et al.* Grain Boundary Mapping in Polycrystalline Graphene. *ACS Nano* **5,** 2142–2146 (2011).

76. Yazyev, O. V. & Louie, S. G. Topological defects in graphene: Dislocations and grain boundaries. *Phys. Rev. B* **81,** 195420 (2010).

77. Jauregui, L. A., Cao, H., Wu, W., Yu, Q. & Chen, Y. P. Electronic properties of grains and grain boundaries in graphene grown by chemical vapor deposition. *Solid State Commun.* **151,** 1100–1104 (2011).

78. Yan, Z. *et al.* Toward the Synthesis of Wafer-Scale Single-Crystal Graphene on Copper Foils. *ACS Nano* **6,** 9110–9117 (2012).

79. Mohsin, A. *et al.* Synthesis of Millimeter-Size Hexagon-Shaped Graphene Single Crystals on Resolidified Copper. *ACS Nano* **7,** 8924–8931 (2013).

80. Gan, L. & Luo, Z. Turning off Hydrogen To Realize Seeded Growth of Subcentimeter Single-Crystal Graphene Grains on Copper. *ACS Nano* **7,** 9480–9488 (2013).

81. Li, J. *et al.* Facile Growth of Centimeter-Sized Single-Crystal Graphene on Copper Foil at Atmospheric Pressure. *J. Mater. Chem. C* **3,** 3530–3535 (2015).

82. Miseikis, V. *et al.* Rapid CVD Growth of Millimetre-Sized Single Crystal Graphene Using A Cold-Wall Reactor. *2D Mater.* **2,** 014006 (2015).

83. Duong, D. L. *et al.* Probing Graphene Grain Boundaries with Optical Microscopy. *Nature* **490,** 235–239 (2012).

84. Yu, S. U. *et al.* Fast Benchtop Visualization of Graphene Grain Boundaries using Adhesive Properties of Defects. *Chem. Commun.* **49,** 5474 (2013).

85. Kim, D. W., Kim, Y. H., Jeong, H. S. & Jung, H.-T. Direct Visualization of Large-Area Graphene Domains and Boundaries by Optical Birefringency. *Nat. Nanotechnol.* **7,** 29–34 (2012).

86. Yu, S. U. *et al.* Simultaneous Visualization of Graphene Grain Boundaries and Wrinkles with Structural Information by Gold Deposition. *ACS Nano* **8,** 8662–8668 (2014).

87. Son, J.-H. *et al.* Detection of Graphene Domains and Defects using Liquid Crystals. *Nat. Commun.* **5,** 3484 (2014).

88. Ago, H. *et al.* Visualization of Grain Structure and Boundaries of Polycrystalline Graphene and Two-Dimensional Materials by Epitaxial Growth of Transition Metal Dichalcogenides. *ACS Nano* **10,** 3233–3240 (2016).

89. Chen, H., Zhu, W. & Zhang, Z. Contrasting Behavior of Carbon Nucleation in the Initial Stages of Graphene Epitaxial Growth on Stepped Metal Surfaces. *Phys. Rev. Lett.* **104,** 186101 (2010).

90. Gao, J., Yip, J., Zhao, J., Yakobson, B. I. & Ding, F. Graphene Nucleation on Transition Metal Surface: Structure Transformation and Role of the Metal Step Edge. *J. Am. Chem. Soc.* **133,** 5009–5015 (2011).

91. Zhang, W., Wu, P., Li, Z. & Yang, J. First-Principles Thermodynamics of Graphene Growth on Cu Surfaces. *J. Phys. Chem. C* **115,** 17782–17787 (2011).

92. Van Wesep, R. G., Chen, H., Zhu, W. & Zhang, Z. Communication: Stable Carbon Nanoarches in the Initial Stages of Epitaxial Growth of Graphene On Cu(111). *J. Chem. Phys.* **134,** 171105 (2011).

93. Luo, Z., Kim, S., Kawamoto, N., Rappe, A. M. & Johnson, A. T. C. Growth Mechanism of Hexagonal-Shape Graphene Flakes with Zigzag Edges. *ACS Nano* **5,** 9154–9160 (2011).

94. Shu, H., Chen, X., Tao, X. & Ding, F. Edge Structural Stability and Kinetics of Graphene Chemical Vapor Deposition Growth. *ACS Nano* **6,** 3243–3250 (2012).

95. Artyukhov, V. I., Liu, Y. & Yakobson, B. I. Equilibrium at the Edge and Atomistic Mechanisms of Graphene Growth. *Proc. Natl. Acad. Sci.* **109,** 15136–15140 (2012).

96. Meng, L., Sun, Q., Wang, J. & Ding, F. Molecular Dynamics Simulation of Chemical Vapor Deposition Graphene Growth on Ni (111) Surface. *J. Phys. Chem. C* **116,** 6097–6102 (2012).

97. Zhang, X., Wang, L., Xin, J., Yakobson, B. I. & Ding, F. Role of Hydrogen in Graphene Chemical Vapor Deposition Growth on a Copper Surface. *J. Am. Chem. Soc.* **136,** 3040–3047 (2014).

98. Cheng, L.-C., Jiang, X., Wang, J., Chen, C. & Liu, R.-S. Nano–Bio Effects: Interaction of Nanomaterials with Cells. *Nanoscale* **5,** 3547–3569 (2013).

99. Castro Neto, A. H., Guinea, F., Peres, N. M. R., Novoselov, K. S. & Geim, A. K. The Electronic Properties of Graphene. *Rev. Mod. Phys.* **81,** 109–162 (2009).

100. Wallace, P. R. The Band Theory of Graphite. *Phys. Rev.* **71,** 622–634 (1947).

101. Ni, Z. H. *et al.* On Resonant Scatterers as a Factor Limiting Carrier Mobility in Graphene. *Nano Lett.* **10,** 3868–3872 (2010).

102. Mayorov, A. S. *et al.* Micrometer-Scale Ballistic Transport in Encapsulated Graphene at Room Temperature. *Nano Lett.* **11,** 2396–2399 (2011).

103. Geim, A. K. & Novoselov, K. S. The Rise of Graphene. *Nat. Mater.* **6,** 183–191 (2007).

104. Zhang, Y., Tan, Y.-W., Stormer, H. L. & Kim, P. Experimental Observation of the Quantum Hall Effect and Berry's Phase in Graphene. *Nature* **438,** 201–204 (2005).

105. Heersche, H. B., Jarillo-Herrero, P., Oostinga, J. B., Vandersypen, L. M. K. & Morpurgo, A. F. Bipolar Supercurrent in Graphene. *Nature* **446,** 56–59 (2007).

106. Zhou, S. Y. *et al.* Substrate-induced Bandgap Opening in Epitaxial Graphene. *Nat. Mater.* **6,** 770–775 (2007).

107. Oostinga, J. B., Heersche, H. B., Liu, X., Morpurgo, A. F. & Vandersypen, L. M. K. Gate-Induced Insulating State in Bilayer Graphene Devices. *Nat. Mater.* **7,** 151–157 (2008).

108. Han, M. Y., Özyilmaz, B., Zhang, Y. & Kim, P. Energy Band-Gap Engineering of Graphene Nanoribbons. *Phys. Rev. Lett.* **98,** (2007).

109. Li, X., Wang, X., Zhang, L., Lee, S. & Dai, H. Chemically Derived, Ultrasmooth Graphene Nanoribbon Semiconductors. *Science* **319,** 1229–1232 (2008).

110. Peres, N. M. R., Guinea, F. & Castro Neto, A. H. Electronic Properties of Disordered Two-Dimensional Carbon. *Phys. Rev. B* **73,** (2006).

111. Gusynin, V. P., Sharapov, S. G. & Carbotte, J. P. Unusual Microwave Response of Dirac Quasiparticles in Graphene. *Phys. Rev. Lett.* **96,** (2006).

112. Geng, H.-Z. *et al.* Effect of Acid Treatment on Carbon Nanotube-Based Flexible Transparent Conducting Films. *J. Am. Chem. Soc.* **129,** 7758–7759 (2007).

113. De, S. & Coleman, J. N. Are There Fundamental Limitations on the Sheet Resistance and Transmittance of Thin Graphene Films? *ACS Nano* **4,** 2713–2720 (2010).

114. Wu, Z. Transparent, Conductive Carbon Nanotube Films. *Science* **305,** 1273–1276 (2004).

115. Lee, J.-Y., Connor, S. T., Cui, Y. & Peumans, P. Solution-Processed Metal Nanowire Mesh Transparent Electrodes. *Nano Lett.* **8,** 689–692 (2008).

116. De, S. *et al.* Silver Nanowire Networks as Flexible, Transparent, Conducting Films: Extremely High DC to Optical Conductivity Ratios. *ACS Nano* **3,** 1767–1774 (2009).

117. Bae, S. *et al.* Roll-to-Roll Production of 30-Inch Graphene Films for Transparent Electrodes. *Nat. Nanotechnol.* **5,** 574–578 (2010).

118. D'Arsié, L. *et al.* Stability of Graphene Doping with MoO3 and I2. *Appl. Phys. Lett.* **105,** 103103 (2014).

119. D'Arsié, L. *et al.* Stable, Efficient P-Type Doping of Graphene by Nitric Acid. *RSC Adv* **6,** 113185–113192 (2016).

120. Zhu, Y., Sun, Z., Yan, Z., Jin, Z. & Tour, J. M. Rational Design of Hybrid Graphene Films for High-Performance Transparent Electrodes. *ACS Nano* **5,** 6472–6479 (2011).

121. Cooper, D. R. *et al.* Experimental Review of Graphene. *ISRN Condens. Matter Phys.* **2012,** 1–56 (2012).

122. Cançado, L. G. *et al.* Quantifying Defects in Graphene via Raman Spectroscopy at Different Excitation Energies. *Nano Lett.* **11,** 3190–3196 (2011).

123. Ferrari, A. C. *et al.* Raman Spectrum of Graphene and Graphene Layers. *Phys. Rev. Lett.* **97,** 187401 (2006).

124. Ferrari, A. C. Raman Spectroscopy of Graphene and Graphite: Disorder, Electron–Phonon Coupling, Doping and Nonadiabatic Effects. *Solid State Commun.* **143,** 47–57 (2007).

125. Ferrari, A. C. & Basko, D. M. Raman Spectroscopy as a Versatile Tool for Studying the Properties of Graphene. *Nat. Nanotechnol.* **8,** 235–246 (2013).

126. Yan, J., Zhang, Y., Kim, P. & Pinczuk, A. Electric Field Effect Tuning of Electron-Phonon Coupling in Graphene. *Phys. Rev. Lett.* **98,** (2007).

127. Pisana, S. *et al.* Breakdown of the Adiabatic Born–Oppenheimer Approximation in Graphene. *Nat. Mater.* **6,** 198–201 (2007).

128. Lee, C., Wei, X., Kysar, J. W. & Hone, J. Measurement of the Elastic Properties and Intrinsic Strength of Monolayer Graphene. *Science* **321,** 385–388 (2008).

129. Balandin, A. A. *et al.* Superior Thermal Conductivity of Single-Layer Graphene. *Nano Lett.* **8,** 902–907 (2008).

130. Reddy, C. D., Rajendran, S. & Liew, K. M. Equilibrium Configuration and Continuum Elastic Properties of Finite Sized Graphene. *Nanotechnology* **17,** 864–870 (2006).

131. Kudin, K. N., Scuseria, G. E. & Yakobson, B. I. C2F, BN, and C Nanoshell Elasticity from ab initio Computations. *Phys. Rev. B* **64,** (2001).

132. Frank, I. W., Tanenbaum, D. M., van der Zande, A. M. & McEuen, P. L. Mechanical Properties of Suspended Graphene Sheets. *J. Vac. Sci. Technol. B Microelectron. Nanometer Struct.* **25,** 2558 (2007).

133. Gajewski, G. & Pao, C.-W. ab initio Calculations of the Reaction Pathways for Methane Decomposition over the Cu (111) Surface. *J. Chem. Phys.* **135,** 064707 (2011).

134. Calizo, I., Balandin, A. A., Bao, W., Miao, F. & Lau, C. N. Temperature Dependence of the Raman Spectra of Graphene and Graphene Multilayers. *Nano Lett.* **7,** 2645–2649 (2007).

135. Seol, J. H. *et al.* Two-Dimensional Phonon Transport in Supported Graphene. *Science* **328,** 213–216 (2010).

136. Neugebauer, P., Orlita, M., Faugeras, C., Barra, A.-L. & Potemski, M. How Perfect Can Graphene Be? *Phys. Rev. Lett.* **103,** (2009).

137. Forbeaux, I., Themlin, J.-M., Charrier, A., Thibaudau, F. & Debever, J.-M. Solid-state Graphitization Mechanisms of Silicon Carbide 6H–SiC Polar Faces. *Appl. Surf. Sci.* **162–163,** 406–412 (2000).

138. Charrier, A. *et al.* Solid-state Decomposition of Silicon Carbide for Growing Ultra-Thin Heteroepitaxial Graphite Films. *J. Appl. Phys.* **92,** 2479–2484 (2002).

139. Hass, J., Millán-Otoya, J. E., First, P. N. & Conrad, E. H. Interface Structure of Epitaxial Graphene Grown on 4H-SiC(0001). *Phys. Rev. B* **78,** 205424 (2008).

140. Hass, J. *et al.* Highly Ordered Graphene for Two Dimensional Electronics. *Appl. Phys. Lett.* **89,** 143106 (2006).

141. Heer, W. A. de *et al.* Large Area and Structured Epitaxial Graphene Produced by Confinement Controlled Sublimation of Silicon Carbide. *Proc. Natl. Acad. Sci.* **108,** 16900–16905 (2011).

142. Kedzierski, J. *et al.* Epitaxial Graphene Transistors on SiC Substrates. *IEEE Trans. Electron Devices* **55,** 2078–2085 (2008).

143. Bonaccorso, F. *et al.* Production and Processing of Graphene and 2d Crystals. *Mater. Today* **15,** 564–589 (2012).

144. O'Neill, A., Khan, U., Nirmalraj, P. N., Boland, J. & Coleman, J. N. Graphene Dispersion and Exfoliation in Low Boiling Point Solvents. *J. Phys. Chem. C* **115,** 5422–5428 (2011).

145. Behrens, M. Über die Verteilung: der Lipase und Arginase zwischen Zellkern und Protoplasma der Leber. Mit 1 Figur im Text. *Hoppe-Seyler´s Z. Für Physiol. Chem.* **258,** 27–32 (2009).

146. Alzari, V. *et al.* Graphene-containing Thermoresponsive Nanocomposite Hydrogels of Poly(N-Isopropylacrylamide) Prepared by Frontal Polymerization. *J. Mater. Chem.* **21,** 8727–8733 (2011).

147. Williams, J. W., Van Holde, K. E., Baldwin, R. L. & Fujita, H. The Theory Of Sedimentation Analysis. *Chem. Rev.* **58,** 715–744 (1958).

148. Green, A. A. & Hersam, M. C. Solution Phase Production of Graphene with Controlled Thickness via Density Differentiation. *Nano Lett.* **9,** 4031–4036 (2009).

149. Petrone, N. *et al.* Chemical Vapor Deposition-Derived Graphene with Electrical Performance of Exfoliated Graphene. *Nano Lett.* **12,** 2751–2756 (2012).

150. Moldt, T. *et al.* High-Yield Production and Transfer of Graphene Flakes Obtained by Anodic Bonding. *ACS Nano* **5,** 7700–7706 (2011).

151. Shukla, A., Kumar, R., Mazher, J. & Balan, A. Graphene Made Easy: High Quality, Large-area Samples. *Solid State Commun.* **149,** 718–721 (2009).

152. Miyamoto, Y., Zhang, H. & Tománek, D. Photoexfoliation of Graphene from Graphite: an ab Initio Study. *Phys. Rev. Lett.* **104,** 208302 (2010).

153. Dhar, S. *et al.* A New Route to Graphene Layers by Selective Laser Ablation. *AIP Adv.* **1,** 022109 (2011).

154. Hackley, J., Ali, D., DiPasquale, J., Demaree, J. D. & Richardson, C. J. K. Graphitic Carbon Growth on Si(111) using Solid Source Molecular Beam Epitaxy. *Appl. Phys. Lett.* **95,** 133114 (2009).

155. Lippert, G. *et al.* Direct Graphene Growth on Insulator. *Phys. Status Solidi B* **248,** 2619–2622 (2011).

156. Ferrari, A. C. *et al.* Stress Reduction and Bond Stability during Thermal Annealing of Tetrahedral Amorphous Carbon. *J. Appl. Phys.* **85,** 7191–7197 (1999).

157. Ilie, A., Ferrari, A. C., Yagi, T. & Robertson, J. Effect of sp2-phase Nanostructure on Field Emission from Amorphous Carbons. *Appl. Phys. Lett.* **76,** 2627–2629 (2000).

158. Ferrari, A. C. *et al.* Density, sp3 Fraction, and Cross-Sectional Structure of Amorphous Carbon Films Determined by X-Ray Reflectivity and Electron Energy-Loss Spectroscopy. *Phys. Rev. B* **62,** 11089–11103 (2000).

159. Ilie, A. *et al.* Role of sp2 Phase in Field Emission from Nanostructured Carbons. *J. Appl. Phys.* **90,** 2024–2032 (2001).

160. Westenfelder, B. *et al.* Transformations of Carbon Adsorbates on Graphene Substrates under Extreme Heat. *Nano Lett.* **11,** 5123–5127 (2011).

161. Muñoz, R. & Gómez-Aleixandre, C. Review of CVD synthesis of graphene. *Chem. Vap. Depos.* **19,** 297–322 (2013).

162. Mattevi, C., Kim, H. & Chhowalla, M. A Review of Chemical Vapour Deposition of Graphene on Copper. *J Mater Chem* **21,** 3324–3334 (2011).

163. Kidambi, P. R. *et al.* The Parameter Space of Graphene Chemical Vapor Deposition on Polycrystalline Cu. *J. Phys. Chem. C* **116,** 22492–22501 (2012).

164. Vlassiouk, I. *et al.* Role of Hydrogen in Chemical Vapor Deposition Growth of Large Single-Crystal Graphene. *ACS Nano* **5,** 6069–6076 (2011).

165. Gao, L., Guest, J. R. & Guisinger, N. P. Epitaxial Graphene on Cu(111). *Nano Lett.* **10,** 3512–3516 (2010).

166. Li, Z. *et al.* Graphene Thickness Control via Gas-Phase Dynamics in Chemical Vapor Deposition. *J. Phys. Chem. C* **116,** 10557–10562 (2012).

167. Sutter, P. W., Flege, J.-I. & Sutter, E. A. Epitaxial Graphene on Ruthenium. *Nat. Mater.* **7,** 406–411 (2008).

168. Sutter, P., Sadowski, J. T. & Sutter, E. Graphene on Pt(111): Growth and Substrate Interaction. *Phys. Rev. B* **80,** (2009).

169. Wang, S. M. *et al.* Synthesis of Graphene on a Polycrystalline Co Film by Radio-Frequency Plasma-Enhanced Chemical Vapour Deposition. *J. Phys. Appl. Phys.* **43,** 455402 (2010).

170. Kwon, S.-Y. *et al.* Growth of Semiconducting Graphene on Palladium. *Nano Lett.* **9,** 3985–3990 (2009).

171. Miniussi, E. *et al.* Thermal Stability of Corrugated Epitaxial Graphene Grown on Re(0001). *Phys. Rev. Lett.* **106,** (2011).

172. Chen, L. *et al.* Growth of Uniform Monolayer Graphene Using Iron-Group Metals via the Formation of an Antiperovskite Layer. *Chem. Mater.* **27,** 8230–8236 (2015).

173. Yu, Q. *et al.* Graphene Segregated on Ni Surfaces and Transferred to Insulators. *Appl. Phys. Lett.* **93,** 113103 (2008).

174. Li, X., Cai, W., Colombo, L. & Ruoff, R. S. Evolution of Graphene Growth on Ni and Cu by Carbon Isotope Labeling. *Nano Lett.* **9,** 4268–4272 (2009).

175. Wofford, J. M., Nie, S., McCarty, K. F., Bartelt, N. C. & Dubon, O. D. Graphene Islands on Cu Foils: The Interplay between Shape, Orientation, and Defects. *Nano Lett.* **10,** 4890–4896 (2010).

176. Zhang, Y., Zhang, L. & Zhou, C. Review of Chemical Vapor Deposition of Graphene and Related Applications. *Acc. Chem. Res.* **46,** 2329–2339 (2013).

177. Li, X., Colombo, L. & Ruoff, R. S. Graphene Films: Synthesis of Graphene Films on Copper Foils by Chemical Vapor Deposition (Adv. Mater. 29/2016). *Adv. Mater.* **28,** 6264–6264 (2016).

178. Bhaviripudi, S., Jia, X., Dresselhaus, M. S. & Kong, J. Role of Kinetic Factors in Chemical Vapor Deposition Synthesis of Uniform Large Area Graphene Using Copper Catalyst. *Nano Lett.* **10,** 4128–4133 (2010).

179. Ciobîcă, I. M., Frechard, F., van Santen, R. A., Kleyn, A. W. & Hafner, J. A DFT Study of Transition States for C−H Activation on the Ru(0001) Surface †. *J. Phys. Chem. B* **104,** 3364–3369 (2000).

180. Zhang, C. J. & Hu, P. Methane Transformation to Carbon and Hydrogen on Pd(100): Pathways and Energetics from Density Functional Theory Calculations. *J. Chem. Phys.* **116,** 322 (2002).

181. Treier, M. *et al.* Surface-Assisted Cyclodehydrogenation Provides a Synthetic Route towards Easily Processable and Chemically Tailored Nanographenes. *Nat. Chem.* **3,** 61–67 (2011).

182. Kim, H. *et al.* Activation Energy Paths for Graphene Nucleation and Growth on Cu. *ACS Nano* **6,** 3614–3623 (2012).

183. Kim, H., Saiz, E., Chhowalla, M. & Mattevi, C. Modeling of the Self-Limited Growth in Catalytic Chemical Vapor Deposition of Graphene. *New J. Phys.* **15,** 053012 (2013).

184. Han, G. H. *et al.* Influence of Copper Morphology in Forming Nucleation Seeds for Graphene Growth. *Nano Lett.* **11,** 4144–4148 (2011).

185. Yuan, Q. *et al.* Magic Carbon Clusters in the Chemical Vapor Deposition Growth of Graphene. *J. Am. Chem. Soc.* **134,** 2970–2975 (2012).

186. Robertson, A. W. & Warner, J. H. Hexagonal Single Crystal Domains of Few-Layer Graphene on Copper Foils. *Nano Lett.* **11,** 1182–1189 (2011).

187. Wu, B. *et al.* Equiangular Hexagon-Shape-Controlled Synthesis of Graphene on Copper Surface. *Adv. Mater.* **23,** 3522–3525 (2011).

188. Yu, Q. *et al.* Control and Characterization of Individual Grains and Grain Boundaries in Graphene Grown by Chemical Vapour Deposition. *Nat. Mater.* **10,** 443–449 (2011).

189. Liu, Y., Dobrinsky, A. & Yakobson, B. I. Graphene Edge from Armchair to Zigzag: The Origins of Nanotube Chirality? *Phys. Rev. Lett.* **105,** 235502 (2010).

190. Liu, J. *et al.* Triangular Graphene Grain Growth on Cube-Textured Cu Substrates. *Adv. Funct. Mater.* **21,** 3868–3874 (2011).

191. Geng, D. *et al.* Large Area Growth of Five-Lobed and Triangular Graphene Grains on Textured Cu Substrate. *Adv. Mater. Interfaces* **3,** (2016).

192. Wang, C. *et al.* Growth of Millimeter-Size Single Crystal Graphene on Cu Foils by Circumfluence Chemical Vapor Deposition. *Sci. Rep.* **4,** (2014).

193. Dai, G.-P., Wu, M. H., Taylor, D. K. & Vinodgopal, K. Square-Shaped, Single-Crystal, Monolayer Graphene Domains by Low-Pressure Chemical Vapor Deposition. *Mater. Res. Lett.* **1,** 67–76 (2013).

194. Chen, Q. *et al.* Synthesis of Well-Aligned Millimeter-Sized Tetragon-Shaped Graphene Domains by Tuning the Copper Substrate Orientation. *Carbon* **93,** 945–952 (2015).

195. Cunha, T. H. R., Ek-Weis, J., Lacerda, R. G. & Ferlauto, A. S. Graphene Chemical Vapor Deposition at Very Low Pressure: the Impact of Substrate Surface Self-Diffusion in Domain Shape. *Appl. Phys. Lett.* **105,** 073104 (2014).

196. Wu, Y. *et al.* Crystal Structure Evolution of Individual Graphene Islands During CVD Growth on Copper Foil. *Adv. Mater.* **25,** 6744–6751 (2013).

197. Murdock, A. T. *et al.* Controlling the Orientation, Edge Geometry, and Thickness of Chemical Vapor Deposition Graphene. *ACS Nano* **7,** 1351–1359 (2013).

198. Fei, W., Yin, J., Liu, X. & Guo, W. Dendritic Graphene Domains: Growth, Morphology and Oxidation Promotion. *Mater. Lett.* **110,** 225–228 (2013).

199. Zhao, P. *et al.* The Role of Hydrogen in Oxygen-Assisted Chemical Vapor Deposition Growth of Millimeter-Sized Graphene Single Crystals. *Nanoscale* **8,** 7646–7653 (2016).

200. Wang, H. *et al.* Controllable Synthesis of Submillimeter Single-Crystal Monolayer Graphene Domains on Copper Foils by Suppressing Nucleation. *J. Am. Chem. Soc.* **134,** 3627–3630 (2012).

201. Chen, W. *et al.* Suppression of Grain Boundaries in Graphene Growth on Superstructured Mn-Cu(111) Surface. *Phys. Rev. Lett.* **109,** (2012).

202. Yuan, Q., Song, G., Sun, D. & Ding, F. Formation of Graphene Grain Boundaries on Cu(100) Surface and a Route Towards Their Elimination in Chemical Vapor Deposition Growth. *Sci. Rep.* **4,** 6541 (2014).

203. Chen, S. *et al.* Millimeter-Size Single-Crystal Graphene by Suppressing Evaporative Loss of Cu During Low Pressure Chemical Vapor Deposition. *Adv. Mater.* **25,** 2062–2065 (2013).

204. Bunch, J. S. *et al.* Impermeable Atomic Membranes from Graphene Sheets. *Nano Lett.* **8,** 2458–2462 (2008).

205. Mueller, N. S. *et al.* Growing Graphene on Polycrystalline Copper Foils by Ultra-High Vacuum Chemical Vapor Deposition. *Carbon* **78,** 347–355 (2014).

206. Wang, Z.-J. *et al.* Direct Observation of Graphene Growth and Associated Copper Substrate Dynamics by in Situ Scanning Electron Microscopy. *ACS Nano* **9,** 1506–1519 (2015).

207. Falvo, M. R. *et al.* Bending and Buckling of Carbon Nanotubes under Large Strain. *Nature* **389,** 582–584 (1997).

208. Qi, Z. & Park, H. S. Intrinsic Energy Dissipation in CVD-Grown Graphene Nanoresonators. *Nanoscale* **4,** 3460 (2012).

209. Tsen, A. W. *et al.* Tailoring Electrical Transport Across Grain Boundaries in Polycrystalline Graphene. *Science* **336,** 1143–1146 (2012).

210. Yakobson, B. I. & Ding, F. Observational Geology of Graphene, at the Nanoscale. *ACS Nano* **5,** 1569–1574 (2011).

211. Ogawa, Y. *et al.* Structure and Transport Properties of the Interface between CVD-Grown Graphene Domains. *Nanoscale* **6,** 7288–7294 (2014).

212. Xing, S., Wu, W., Wang, Y., Bao, J. & Pei, S.-S. Kinetic Study of Graphene Growth: Temperature Perspective on Growth Rate and Film Thickness by Chemical Vapor Deposition. *Chem. Phys. Lett.* **580,** 62–66 (2013).

213. Ning, J. *et al.* Comprehensive Nucleation Mechanisms of Quasi-Monolayer Graphene Grown on Cu by Chemical Vapor Deposition. *J. Cryst. Growth* **424,** 55–61 (2015).

214. Ohring, M. *Materials Science of Thin Films (Second Edition)*. (Academic Press, 2002).

215. Liang, X. *et al.* Toward Clean and Crackless Transfer of Graphene. *ACS Nano* **5,** 9144–9153 (2011).

216. Xie, J. & Spallas, J. P. Different Contrast Mechanisms in SEM Imaging of Graphene. *Agil. Appl. Note* (2012).

217. Lee, J., Zheng, X., Roberts, R. C. & Feng, P. X.-L. Scanning Electron Microscopy Characterization of Structural Features in Suspended and Non-Suspended Graphene by Customized CVD Growth. *Diam. Relat. Mater.* **54,** 64–73 (2015).

218. Wu, X. *et al.* Growth of Continuous Monolayer Graphene with Millimeter-sized Domains Using Industrially Safe Conditions. *Sci. Rep.* **6,** 21152 (2016).

219. Wu, X., Zhong, G. & Robertson, J. Nondestructive Optical Visualisation of Graphene Domains and Boundaries. *Nanoscale* **8,** 16427–16434 (2016).

220. Boyd, D. A. *et al.* Single-step Deposition of High-mobility Graphene at Reduced Temperatures. *Nat. Commun.* **6,** (2015).

221. Ryu, J. *et al.* Fast Synthesis of High-Performance Graphene Films by Hydrogen-Free Rapid Thermal Chemical Vapor Deposition. *ACS Nano* **8,** 950–956 (2014).

222. Nguyen, V. L. *et al.* Seamless Stitching of Graphene Domains on Polished Copper (111) Foil. *Adv. Mater.* **27,** 1376–1382 (2015).

223. Luo, Z. *et al.* Effect of Substrate Roughness and Feedstock Concentration on Growth of Wafer-Scale Graphene at Atmospheric Pressure. *Chem. Mater.* **23,** 1441–1447 (2011).

224. Hsieh, Y.-P. *et al.* Effect of Catalyst Morphology on the Quality of CVD Grown Graphene. *J. Nanomater.* **2013,** 1–6 (2013).

225. Shin, Y. C. & Kong, J. Hydrogen-Excluded Graphene Synthesis via Atmospheric Pressure Chemical Vapor Deposition. *Carbon* **59,** 439–447 (2013).

226. Seung Kim, Y. *et al.* Methane as An Effective Hydrogen Source for Single-Layer Graphene Synthesis on Cu Foil by Plasma Enhanced Chemical Vapor Deposition. *Nanoscale* **5,** 1221–1226 (2013).

227. Liu, L. *et al.* A Systematic Study of Atmospheric Pressure Chemical Vapor Deposition Growth of Large-Area Monolayer Graphene. *J. Mater. Chem.* **22,** 1498–1503 (2012).

228. Lee, Y. *et al.* Wafer-Scale Synthesis and Transfer of Graphene Films. *Nano Lett.* **10,** 490–493 (2010).

229. Jie Sun *et al.* Low Partial Pressure Chemical Vapor Deposition of Graphene on Copper. *IEEE Trans. Nanotechnol.* **11,** 255–260 (2012).

230. Ago, H. *et al.* Epitaxial Growth and Electronic Properties of Large Hexagonal Graphene Domains on Cu(111) Thin Film. *Appl. Phys. Express* **6,** 075101 (2013).

231. Hu, B., Ago, H., Orofeo, C. M., Ogawa, Y. & Tsuji, M. On the Nucleation of Graphene by Chemical Vapor Deposition. *New J. Chem.* **36,** 73–77 (2011).

232. Orofeo, C. M. *et al.* Influence of Cu Metal on the Domain Structure and Carrier Mobility in Single-Layer Graphene. *Carbon* **50,** 2189–2196 (2012).

233. Celebi, K. *et al.* Evolutionary Kinetics of Graphene Formation on Copper. *Nano Lett.* **13,** 967–974 (2013).

234. Zhang, B. *et al.* Low-Temperature Chemical Vapor Deposition Growth of Graphene from Toluene on Electropolished Copper Foils. *ACS Nano* **6,** 2471–2476 (2012).

235. Jacquet, P. A. Electrolytic and Chemical Polishing. *Metall. Rev.* **1,** 157–238 (1956).

236. Edwards, J. The Mechanism of Electropolishing of Copper in Phosphoric Acid Solutions II. The Mechanism of Smoothing. *J. Electrochem. Soc.* **100,** 223C–230C (1953).

237. Jia, C., Jiang, J., Gan, L. & Guo, X. Direct Optical Characterization of Graphene Growth and Domains on Growth Substrates. *Sci. Rep.* **2,** 707 (2012).

238. Venugopal, A. *et al.* Effective Mobility of Single-Layer Graphene Transistors as A Function of Channel Dimensions. *J. Appl. Phys.* **109,** 104511 (2011).

239. Novoselov, K. S. *et al.* A Roadmap for Graphene. *Nature* **490,** 192–200 (2012).

240. Clark, K. W. *et al.* Spatially Resolved Mapping of Electrical Conductivity across Individual Domain (Grain) Boundaries in Graphene. *ACS Nano* **7,** 7956–7966 (2013).

241. Wang, S., Suzuki, S. & Hibino, H. Raman Spectroscopic Investigation of Polycrystalline Structures of CVD-Grown Graphene by Isotope Labeling. *Nanoscale* **6,** 13838–13844 (2014).

242. Zhu, S. *et al.* Cu Hill and Graphene Grain Evolution in the Synthesis of Millimeter-Sized Single Crystal Graphene during Low Pressure Chemical Vapor Deposition. *RSC Adv.* **4,** 32941 (2014).

243. Kong, X. H. *et al.* Non-destructive and Rapid Evaluation of Chemical Vapor Deposition Graphene by Dark Field Optical Microscopy. *Appl. Phys. Lett.* **103,** 043119 (2013).

244. Wood, J. D., Schmucker, S. W., Lyons, A. S., Pop, E. & Lyding, J. W. Effects of Polycrystalline Cu Substrate on Graphene Growth by Chemical Vapor Deposition. *Nano Lett.* **11,** 4547–4554 (2011).

245. Safarian, J. & Engh, T. A. Vacuum Evaporation of Pure Metals. *Metall. Mater. Trans. A* **44,** 747–753 (2013).

246. Chatterjee, B. Anisotropy of Melting for Cubic Metals. *Nature* **275,** 203–203 (1978).

247. Häkkinen, H. & Manninen, M. Computer Simulation of Disordering and Premelting of Low-Index Faces of Copper. *Phys. Rev. B* **46,** 1725 (1992).

248. Hayashi, K., Sato, S. & Yokoyama, N. Anisotropic Graphene Growth Accompanied by Step Bunching on a Dynamic Copper Surface. *Nanotechnology* **24,** 025603 (2013).

249. Alstrup, I. & Tavares, M. T. Kinetics of Carbon Formation from CH4 + H2 on Silica-Supported Nickel and Ni-Cu Catalysts. *J. Catal.* **139,** 513–524 (1993).

250. Eres, G. *et al.* Cooperative Island Growth of Large-Area Single-Crystal Graphene on Copper Using Chemical Vapor Deposition. *ACS Nano* **8,** 5657–5669 (2014).

251. Chuang, M.-C. & Woon, W.-Y. Nucleation and Growth Dynamics of Graphene on Oxygen Exposed Copper Substrate. *Carbon* **103,** 384–390 (2016).

252. Geng, D. *et al.* Self-Aligned Single-Crystal Graphene Grains. *Adv. Funct. Mater.* **24,** 1664–1670 (2014).

253. Zhang, Y. *et al.* Vapor Trapping Growth of Single-Crystalline Graphene Flowers: Synthesis, Morphology, and Electronic Properties. *Nano Lett.* **12,** 2810–2816 (2012).

254. Sutter, P., Ciobanu, C. V. & Sutter, E. Real-Time Microscopy of Graphene Growth on Epitaxial Metal Films: Role of Template Thickness and Strain. *Small* **8,** 2250–2257 (2012).

255. Zhang, Y., Li, Z., Kim, P., Zhang, L. & Zhou, C. Anisotropic Hydrogen Etching of Chemical Vapor Deposited Graphene. *ACS Nano* **6,** 126–132 (2012).

256. Zhang, H. *et al.* Edge Morphology Evolution of Graphene Domains during Chemical Vapor Deposition Cooling Revealed through Hydrogen Etching. *Nanoscale* **8,** 4145–4150 (2016).

257. Ma, T. *et al.* Repeated Growth–Etching–Regrowth for Large-Area Defect-Free Single-Crystal Graphene by Chemical Vapor Deposition. *ACS Nano* **8,** 12806–12813 (2014).

258. Zhang, X. *et al.* Hydrogen-induced Effects on the CVD Growth of High-quality Graphene Structures. *Nanoscale* **5,** 8363–8366 (2013).

259. Yao, Y. & Wong, C. Monolayer Graphene Growth using Additional Etching Process in Atmospheric Pressure Chemical Vapor Deposition. *Carbon* **50,** 5203–5209 (2012).

260. Geng, D. *et al.* Fractal Etching of Graphene. *J. Am. Chem. Soc.* **135,** 6431–6434 (2013).

261. Zhang, Y. H. *et al.* Controllable Growth of Millimeter-size Graphene Domains on Cu Foil. *Mater. Lett.* **96,** 149–151 (2013).

262. Seifert, M., Drieschner, S., Blaschke, B. M., Hess, L. H. & Garrido, J. A. Induction Heating-assisted Repeated Growth and Electrochemical Transfer of Graphene on Millimeter-thick Metal Substrates. *Diam. Relat. Mater.* **47,** 46–52 (2014).

263. Qi, M. *et al.* Hydrogen Kinetics on Scalable Graphene Growth by Atmospheric Pressure Chemical Vapor Deposition with Acetylene. *J. Phys. Chem. C* **117,** 14348–14353 (2013).

264. Nie, S., Wofford, J. M., Bartelt, N. C., Dubon, O. D. & McCarty, K. F. Origin of the Mosaicity in Graphene Grown on Cu(111). *Phys. Rev. B* **84,** 155425 (2011).

265. Wu, P., Zhang, W., Li, Z. & Yang, J. Mechanisms of Graphene Growth on Metal Surfaces: Theoretical Perspectives. *Small* **10,** 2136–2150 (2014).

266. Kidambi, P. R. *et al.* Observing Graphene Grow: Catalyst–Graphene Interactions during Scalable Graphene Growth on Polycrystalline Copper. *Nano Lett.* **13,** 4769–4778 (2013).

267. Zhang, J., Hu, P., Wang, X. & Wang, Z. Structural Evolution and Growth Mechanism of Graphene Domains on Copper Foil by Ambient Pressure Chemical Vapor Deposition. *Chem. Phys. Lett.* **536,** 123–128 (2012).

268. Li, X. *et al.* Large-Area Graphene Single Crystals Grown by Low-Pressure Chemical Vapor Deposition of Methane on Copper. *J. Am. Chem. Soc.* **133,** 2816–2819 (2011).

269. Wu, T. *et al.* Triggering the Continuous Growth of Graphene Toward Millimeter-Sized Grains. *Adv. Funct. Mater.* **23,** 198–203 (2013).

270. Zhang, J. *et al.* CVD Growth of Large Area and Uniform Graphene on Tilted Copper Foil for High Performance Flexible Transparent Conductive Film. *J. Mater. Chem.* **22,** 18283–18290 (2012).

271. Zhang, H. *et al.* Effect of Hydrogen in Size-Limited Growth of Graphene by Atmospheric Pressure Chemical Vapor Deposition. *J. Electron. Mater.* **44,** 79–86 (2015).

272. Lin, L. *et al.* Rapid Growth of Large Single-Crystalline Graphene via Second Passivation and Multistage Carbon Supply. *Adv. Mater.* **28,** 4671–4677 (2016).

273. Ma, T. *et al.* Edge-controlled Growth and Kinetics of Single-crystal Graphene Domains by Chemical Vapor Deposition. *Proc. Natl. Acad. Sci.* **110,** 20386–20391 (2013).

274. An, W., Zeng, X. C. & Turner, C. H. First-principles Study of Methane Dehydrogenation on a Bimetallic Cu/Ni(111) Surface. *J. Chem. Phys.* **131,** 174702 (2009).

275. Au, C.-T., Ng, C.-F. & Liao, M.-S. Methane Dissociation and Syngas Formation on Ru, Os, Rh, Ir, Pd, Pt, Cu, Ag, and Au: A Theoretical Study. *J. Catal.* **185,** 12–22 (1999).

276. Wu, P., Zhang, W., Li, Z., Yang, J. & Hou, J. G. Communication: Coalescence of Carbon Atoms on Cu (111) Surface: Emergence of a Stable Bridging-Metal Structure Motif. *J. Chem. Phys.* **133,** 071101 (2010).

277. Yazyev, O. V. & Pasquarello, A. Effect of Metal Elements in Catalytic Growth of Carbon Nanotubes. *Phys. Rev. Lett.* **100,** 156102 (2008).

278. Bartelt, N. C. & McCarty, K. F. Graphene Growth on Metal Surfaces. *MRS Bull.* **37,** 1158–1165 (2012).

279. Witten, T. A. & Sander, L. M. Diffusion-Limited Aggregation, a Kinetic Critical Phenomenon. *Phys. Rev. Lett.* **47,** 1400–1403 (1981).

280. Ma, T. *et al.* Edge-controlled growth and kinetics of single-crystal graphene domains by chemical vapor deposition. *Proc. Natl. Acad. Sci.* **110,** 20386–20391 (2013).

281. Jung, D. H., Kang, C., Nam, J. E., Jeong, H. & Lee, J. S. Surface Diffusion Directed Growth of Anisotropic Graphene Domains on Different Copper Lattices. *Sci. Rep.* **6,** 21136 (2016).

APPENDICES

APPENDIX 1 MATHEMATICAL DETAILS FOR MODELLING EDGE-ATTACHMENT-LIMITED GRAPHENE GROWTH

Substituting Equations 6.2.3 and 6.2.4 into Equations 6.2.1 and 6.2.2 yields the first-order ordinary differential equations for $L(t)$, $N(t)$, and $\Theta(t)$:

$$\begin{cases} \dfrac{dL(t)}{dt} = \dfrac{1}{2}\{k_{att}\cdot[C_0 - \rho_G \cdot N(t)\cdot L(t)^2] - r_{growth\_etch}\} \\ \dfrac{dN(t)}{dt} = k_{nuc}\cdot[C_0 - \rho_G \cdot N(t)\cdot L(t)^2] - r_{nucleus\_etch} \\ \dfrac{d\Theta(t)}{dt} = \dfrac{d}{dt}\left(N(t)\cdot L(t)^2\right) \\ L(0) = 0 \\ N(0) = 0 \\ \Theta(0) = 0 \end{cases}, \qquad (A1.1)$$

where the initial domain radius $L(0)$, the initial nucleation density $N(0)$, and the initial coverage $\Theta(0)$ have been set zero for simplicity. When used to fit the experimental data, the actual initial moment can be set as the end of the experimentally measured incubation period.

Define k_1, k_2, Θ_{s1}, and Θ_{s2} as $\begin{cases} k_1 = k_{att}\cdot\rho_G \\ k_2 = k_{nuc}\cdot\rho_G \\ \Theta_{s1} = \dfrac{C_0 - r_{growth\_etch}/k_{att}}{\rho_G} \\ \Theta_{s2} = \dfrac{C_0 - r_{nucleus\_etch}/k_{nuc}}{\rho_G} \end{cases}$ (A1.2),

Equations A1.1 can be re-arranged into the new forms:

$$\begin{cases} \dfrac{dL(t)}{dt} = \dfrac{1}{2}k_1[\Theta_{s1} - N(t)\cdot L(t)^2] \\ \dfrac{dN(t)}{dt} = k_2[\Theta_{s2} - N(t)\cdot L(t)^2] \\ \dfrac{d\Theta(t)}{dt} = \dfrac{d}{dt}\left(N(t)\cdot L(t)^2\right) \\ L(0) = 0 \\ N(0) = 0 \\ \Theta(0) = 0 \end{cases}. \qquad (A1.3)$$

Define the characteristic domain radius L_c, the characteristic nucleation density N_c, the characteristic coverage Θ_c , the characteristic time t_c, the dimensionless domain radius l, the dimensionless nucleation density n, the dimensionless coverage θ, and the dimensionless time β as:

$$\begin{cases} L_c = \left(\frac{1}{2}\frac{k_1}{k_2}\right)^{1/3} \cdot \Theta_{s1}{}^{1/3} \\ N_c = \left(2\frac{k_2}{k_1}\right)^{2/3} \cdot \Theta_{s2}{}^{1/3} \\ \Theta_c = N_c \cdot L_c{}^2 = \Theta_{s1}{}^{2/3} \cdot \Theta_{s2}{}^{1/3} \\ t_c \triangleq \frac{2L_c}{k_1 \cdot \Theta_{s1}} \end{cases} \quad (\text{A1.4}) \quad \text{and} \quad \begin{cases} l = \frac{L(t)}{L_c} \\ n = \frac{N(t)}{N_c} \\ \theta = \frac{\Theta(t)}{\Theta_c} = \frac{\Theta(t)}{\Theta_{s1}^{2/3} \cdot \Theta_{s2}^{1/3}} = n \cdot l^2 \\ \beta = \frac{t}{t_c} \end{cases}, \quad (\text{A1.5})$$

Equations A1.3 can then be transformed into the dimensionless forms:

$$\begin{cases} \frac{dl}{d\beta} = 1 - p \cdot n \cdot l^2,\ l(0) = 0 \\ \frac{dn}{d\beta} = p^2 - n \cdot l^2,\ n(0) = 0 \\ \frac{d\theta}{d\beta} = \frac{d\left(n \cdot l^2\right)}{d\beta},\ \theta(0) = 0 \end{cases}. \quad (\text{A1.6})$$

For p = 1, Equations A1.6 become: $\begin{cases} \frac{dl}{d\beta} = 1 - l^3,\ n = l,\ l(0) = 0 \\ \frac{d\theta}{d\beta} = 3\theta^{2/3}(1-\theta),\ \theta(0) = 0 \end{cases}$. (A1.7).

They have analytic solutions in the implicit forms:

$$\begin{cases} \ln\left(\frac{l^2 + l + 1}{l^2 - 2l + 1}\right) + 2\sqrt{3} \cdot \arctan\left(\frac{2l+1}{\sqrt{3}}\right) = 6\beta + \frac{\pi}{\sqrt{3}} \\ n(\beta) = l(\beta) \\ \ln\left(\frac{\theta^{2/3} + \theta^{1/3} + 1}{\theta^{2/3} - 2\theta^{1/3} + 1}\right) + 2\sqrt{3} \cdot \arctan\left(\frac{2\theta^{1/3}+1}{\sqrt{3}}\right) = 6\beta + \frac{\pi}{\sqrt{3}} \end{cases}. \quad (\text{A1.8})$$

For p = 0, Equations A1.6 become:

$$\begin{cases} \frac{dl}{d\beta} = 1 - l^2,\ l(0) = 0 \\ \frac{d\theta}{d\beta} = 2\theta^{1/2}(1-\theta) \end{cases}. \quad (\text{A1.9})$$

They have analytical solutions in the explicit forms:

$$\begin{cases} l(\beta) = \tanh(\beta) \\ \theta(\beta) = (\tanh(\beta))^2 \end{cases}. \qquad (A1.10)$$

For general values of p, i.e., $0 < p < 1$, there are no analytic solutions during Stage 1 so the equations have to be numerically solved for each given value of p. It is noteworthy that there is even no closed-form equation for $\theta(\beta)$ during Stage 1 due to the relation $l(\beta) = p \cdot n(\beta) + (1 - p^3) \cdot \beta$. Hence $\theta(\beta)$ has to be numerically calculated using $\theta(\beta)=n(\beta)\cdot l(\beta)^2$. Since the nucleation density remains constant during Stage 2, the Stage 2 equations for $l(\beta)$ and $\theta(\beta)$ are analytically solvable:

$$\begin{cases} l(\beta) = \dfrac{1}{\sqrt{p \cdot n_s}} \tanh\left[\operatorname{arctanh}\left(p^{3/2}\right) + \sqrt{p \cdot n_s}\,(\beta - \beta_2) \right] \\ n(\beta) \equiv n_s \\ \theta(\beta) = n_s \cdot l(\beta)^2 \end{cases}, \quad (A1.11)$$

where n_s denotes the saturated nucleation density and β_2 is the ending time of Stage 1 as well as the beginning time of Stage 2. As $\beta \to \infty$, the growth reaches its final saturated state. The saturated domain radius l_s (dimensionless) and the saturated coverage θ_s (dimensionless) are dependent on the nucleation-growth convolution intensity p:

$$\begin{cases} l_s = \dfrac{1}{\sqrt{p \cdot n_s}} \\ \theta_s = \dfrac{1}{p} \end{cases}. \qquad (A1.12)$$

There are no analytical expressions for l_s, n_s and β_2 for general values of p so they have to be determined from the numerical solutions of $l(\beta)$ and $n(\beta)$. Yet for $p \ll 1$, the approximate analytical solutions for $l(\beta)$ and $n(\beta)$ exist:

$$p \ll 1 \quad \to \quad \begin{cases} l(\beta) \approx l_2 \cdot \dfrac{\beta}{\beta_2} \\ n(\beta) \approx \dfrac{1}{\sqrt[3]{9}} \dfrac{p^2}{(l_2/\beta_2)^{2/3}} \cdot Q\left(\dfrac{1}{3}, \dfrac{1}{3}\beta^3\right) \end{cases}, \qquad (A1.13)$$

where $l_2 = p/\sqrt{n_s}$ is the domain radius at $\beta = \beta_2$ and $Q(a,x)$ is defined as $Q(a,x) = e^{-x}\int_0^x z^{a-1}e^z dz$. The corresponding n_s and l_s can be expressed in the approximate analytical forms:

$$p \ll 1 \rightarrow \begin{cases} n_s \approx p^2 \\ l_s \approx p^{-3/2} \end{cases}. \qquad (A1.14).$$

Using the explicit expressions for p (Equations 6.5), the saturated nucleation density with dimensions in the case of p <<1 is obtained as:

$$N_s = n_s \cdot N_c \approx p^2 \cdot N_c \propto \frac{\Theta_{s2}}{(\Theta_{s1})^{2/3}} = \frac{K \cdot \frac{P_{CH_4}}{(P_{H_2})^{(4-x)/2}} - \frac{1}{K''} \cdot \exp\left(\frac{E_{nuc} - E_{nucleus\_etch}}{k_B T}\right)}{\left(K \cdot \frac{P_{CH_4}}{(P_{H_2})^{(4-x)/2}} - \frac{1}{K'} \cdot \exp\left(\frac{E_{att} - E_{growth\_etch}}{k_B T}\right)\right)^{2/3}} \propto \left(\frac{P_{CH_4}}{(P_{H_2})^{(4-x)/2}}\right)^{1/3}. \qquad (A1.15)$$

For p = 1, $\Theta_{s1} = \Theta_{s2} = \Theta_s$, so n_s = 1, and the saturated nucleation density with dimensions becomes :

$$N_s = n_s \cdot N_c = N_c \propto \Theta_s^{1/3} \propto \left(\frac{P_{CH_4}}{(P_{H_2})^{(4-x)/2}}\right)^{1/3}. \qquad (A1.16)$$

APPENDIX 2 MATHEMATICAL DETAILS FOR MODELLING SURFACE-DIFFUSION-CONTROLLED GRAPHENE GROWTH

Suppose the domain radius is $L(t)$ at time t and the its increment is ΔL within the infinitely small time interval [t, t+Δt]. This requires that the total amount of the crystallized carbon atoms increase by $\rho_G \cdot \Delta L$, which should be converted from the unbound hydrocarbons with the equal amount. There are three sources contributing to this amount. The first is the interfacial carbon which is 'eaten' by the propagating domain edge. This amount equals $C_I(t) \cdot \Delta L$. The second source is those hydrocarbons that diffuse towards the domain edge from the farther Cu surfaces driven by the concentration gradient. The Fick's first law of diffusion states that this amount is proportional to the interfacial concentration gradient:

$$D \cdot \left.\frac{\partial C(x,t)}{\partial x}\right|_{x=L(t)-L_s} \cdot \Delta t. \qquad (\text{A2.1})$$

The last term is the etching of the crystallized carbon atoms from the domain edge, $-E \cdot \Delta t$, where E is the constant etching rate. Putting the three terms into the mass conservation relation yields:

$$\rho_G \cdot \Delta L = C_I(t) \cdot \Delta L + D \cdot \left.\frac{\partial C(x,t)}{\partial x}\right|_{x=L(t)-L_s} \cdot \Delta t - E \cdot \Delta t, \qquad (\text{A2.2})$$

which, in the continuous limit $\Delta t \to 0$, leads to the differential form of the growth rate equation:

$$\left(\rho_G - C_I(t)\right)\frac{dL(t)}{dt} = D \cdot \left.\frac{\partial C(x,t)}{\partial x}\right|_{x=L(t)-L_s} - E. \qquad (\text{A2.3})$$

Combining Equations 6.3.1, 6.3.2, 6.3.3, and 6.3.4, the dimensionless equations and boundary conditions for Stage I and Stage II are respectively:

$$\text{Stage 1} \Rightarrow \begin{cases} \dfrac{\partial^2 C(\alpha,\beta)}{\partial \alpha^2} = \dfrac{\partial C(\alpha,\beta)}{\partial \beta} \\ C(\alpha = l-1, \beta) = C_I(\beta) \\ C(\alpha, \beta = 0) = \begin{cases} C_0, (-1 < \alpha \le 0) \\ C_I(0), (\alpha = -1) \end{cases} \\ \dfrac{dl}{d\beta} = \dfrac{1}{(\rho_G - C_I(\beta))} \cdot \left(\left. \dfrac{\partial C(\alpha,\beta)}{\partial \alpha} \right|_{\alpha = l-1} - e \cdot (C_0 - C_I(0)) \right) \\ l(0) = 0 \end{cases}, \qquad (A2.4)$$

$$\text{Stage 2} \Rightarrow \begin{cases} \dfrac{\partial^2 C(\alpha,\beta)}{\partial \alpha^2} = \dfrac{\partial C(\alpha,\beta)}{\partial \beta} \\ C(l(\beta) + d(\beta) - 1, \beta) = 0 \\ \dfrac{dl}{d\beta} = \dfrac{1}{(\rho_G - 0)} \cdot \left(\left. \dfrac{\partial C(\alpha,\beta)}{\partial \alpha} \right|_{\alpha = l+d-1} - e \cdot (C_0 - C_I(0)) \right), \\ l(\beta_0) = l_0 \\ d(\beta_0) = 0 \end{cases} \qquad (A2.5)$$

where β_0 is the ending time of Stage I as well as the starting time of Stage II, l_0 is the domain length at time β_0, and $d(\beta)$ is the time-dependent width of the depletion layer.

The analytical solution of the concentration field satisfying A2.4 and A2.5 is:

$$C(\alpha,\beta) = C_0 - \frac{C_0 - C_I(0)}{\operatorname{erfc}(\eta)} \left(\operatorname{erfc}\left(\frac{1-\alpha}{2\sqrt{\beta}} \right) + \operatorname{erfc}\left(\frac{1+\alpha}{2\sqrt{\beta}} \right) \right), \qquad (A2.6)$$

where erfc is the complementary error function and η is the positive root to the following equation:

$$\sqrt{\pi} \cdot \eta \cdot \exp(\eta^2) \cdot \operatorname{erfc}(\eta) = \frac{C_0 - C_I(0)}{\rho_G - C_I(0)}. \qquad (A2.7)$$

A physically reasonable diffusion-growth scenario requires $\rho_G > C_0 > C_I(0) \ge 0$ which guarantees the above equation has one and only one positive root.

The explicit forms of the domain growth rate equations for Stage I and Stage II are respectively:

$$\text{Stage 1} \Rightarrow \begin{cases} \dfrac{dl}{d\beta} = \dfrac{C_0 - C_I(0)}{\rho_G - \left\{ C_0 - \dfrac{C_0 - C_I(0)}{\operatorname{erfc}(\eta)} \left(\operatorname{erfc}\left(\dfrac{2-l}{2\sqrt{\beta}} \right) + \operatorname{erfc}\left(\dfrac{l}{2\sqrt{\beta}} \right) \right) \right\}} \times \\ \left\{ \dfrac{1}{\sqrt{\pi}} \cdot \dfrac{1}{\operatorname{erfc}(\eta)} \cdot \dfrac{1}{\sqrt{\beta}} \left(\exp\left(-\dfrac{l^2}{4\beta} \right) - \exp\left(-\dfrac{(2-l)^2}{4\beta} \right) \right) - e \right\} \\ l(0) = 0 \end{cases} \quad (\text{A2.8})$$

$$\text{Stage 2} \Rightarrow \begin{cases} C_0 - \dfrac{C_0 - C_I(0)}{\operatorname{erfc}(\eta)} \left(\operatorname{erfc}\left(\dfrac{l+d}{2\sqrt{\beta}} \right) + \operatorname{erfc}\left(\dfrac{2-l-d}{2\sqrt{\beta}} \right) \right) = 0 \\ \dfrac{dl}{d\beta} = \dfrac{C_0 - C_I(0)}{\rho_G - 0} \times \\ \left\{ \dfrac{1}{\sqrt{\pi}} \cdot \dfrac{1}{\operatorname{erfc}(\eta)} \cdot \dfrac{1}{\sqrt{\beta}} \left(\exp\left(-\dfrac{(l+d)^2}{4\beta} \right) - \exp\left(-\dfrac{(2-l-d)^2}{4\beta} \right) \right) - e \right\} \\ d(\beta_0) = 0 \\ l(\beta_0) = l_0 \end{cases} . \quad (\text{A2.9})$$

Under the limit of $\beta \to 0$, the Stage I equation for $l(\beta)$ (A2.8) recedes to the below asymptotic form:

$$\frac{dl}{d\beta} \approx \eta \cdot \exp(\eta^2) \cdot \frac{1}{\sqrt{\beta}} \exp\left(-\frac{l^2}{4\beta} \right). \quad (\text{A2.10})$$

Therefore the initial time-dependence of $l(\beta)$ is asymptotically square-root:

$$l(\beta) \approx 2\eta \cdot \sqrt{\beta}. \quad (\text{A2.11})$$

For e = 0, the residual central concentration is zero and hence the time to reach saturation is determined as:

$$C(\alpha = 0, \beta_s) = 0 \quad \Rightarrow \quad \operatorname{erfc}\left(\frac{1}{2\sqrt{\beta_s}} \right) = \frac{1}{2} \cdot \operatorname{erfc}(\eta) \cdot \frac{C_0}{C_0 - C_I(0)} \quad (\text{A2.12})$$

APPENDIX 3 PROOF FOR THE ACTIVATION ENERGY RELATIONSHIPS

Recall that the initial length growth rate for the edge-attachment-controlled regime is

$$\lim_{t\to 0}\frac{dL(t)}{dt}=\lim_{t\to 0}\frac{1}{2}k_1[\Theta_{s1}-N(t)\cdot L(t)^2]=\frac{1}{2}k_1\Theta_{s1},$$

where k_1 is proportional to the rate of the hydrocarbons being attached onto the domain edges, $k_1=\rho_G\cdot k_{att}\propto\exp\left(-E_{att}/k_BT\right)$. The change of the logarithm initial linear growth rate upon temperature change is :

$$\frac{\Delta\left(\lim_{t\to 0}\ln\frac{dL(t)}{dt}\right)}{\Delta\left(\frac{1}{T}\right)}=\frac{\Delta\left(\ln k_1\right)}{\Delta\left(\frac{1}{T}\right)}+\frac{\Delta\left(\ln\Theta_{s1}\right)}{\Delta\left(\frac{1}{T}\right)}.\ .$$

As has been shown by the experimental observations, the change of the logarithm of the saturated coverage is much less sensitive than that of the initial linear growth rate, particularly at high growth temperature approaching the Cu melting point. So the above relation is approximately:

$$\frac{\Delta\left(\lim_{t\to 0}\ln\frac{dL(t)}{dt}\right)}{\Delta\left(\frac{1}{T}\right)}\approx\frac{\Delta\left(\ln k_1\right)}{\Delta\left(\frac{1}{T}\right)}.$$

Therefore the activation energy for the linear growth rate can be approximated by E_{att}. Similar arguments reveal that the activation energy for the initial nucleation rate is approximately E_{nuc}:

$$-\frac{\Delta\left(\lim_{t\to 0}\ln\frac{dN(t)}{dt}\right)}{\Delta\left(\frac{1}{k_BT}\right)}\approx-\frac{\Delta\left(\ln k_2\right)}{\Delta\left(\frac{1}{k_BT}\right)}=E_{nuc}.$$

Both of these two conclusions hold for general edge-attachment-controlled growth. We now apply them to the extreme case of p =1. For p = 1, we have $\Theta_{s1}=\Theta_{s2}=\Theta_s$, so the dimensionless saturated domain length and nucleation density are both 1, i.e., l_s = 1 and θ_s = 1, and hence the original saturated domain length and nucleation density with physical dimensions (L_s and N_s) are:

$$\begin{cases} L_c = \left(\frac{1}{2}\frac{k_1}{k_2}\right)^{1/3} \cdot \Theta_{s1}^{\,1/3} \\ N_c = \left(2\frac{k_2}{k_1}\right)^{2/3} \cdot \Theta_{s2}^{\,1/3} \\ l = \frac{L(t)}{L_c} \\ n = \frac{N(t)}{N_c} \end{cases} \oplus \begin{cases} \Theta_{s1} = \Theta_{s2} = \Theta_s \\ l_s = 1 \\ \theta_s = 1 \end{cases} \Rightarrow \begin{cases} L_s = L_c = \left(\frac{k_1}{2k_2}\right)^{1/3} \cdot \Theta_s^{\,1/3} \\ N_s = N_c = \left(\frac{2k_2}{k_1}\right)^{2/3} \cdot \Theta_s^{\,1/3} \end{cases}.$$

Therefore the activation energy for the saturated domain length, $E(L_s)$, and the saturated nucleation density, $E(N_s)$, can be obtained as the linear combinations of that for the initial linear growth rate and nucleation rate:

$$\begin{cases} E(L_s) = -\dfrac{\Delta(\ln L_s)}{\Delta\left(\frac{1}{k_B T}\right)} \approx -\frac{1}{3} \cdot \dfrac{\Delta(\ln k_1 - \ln k_2)}{\Delta\left(\frac{1}{k_B T}\right)} \\ E(N_s) = -\dfrac{\Delta(\ln N_s)}{\Delta\left(\frac{1}{k_B T}\right)} \approx -\frac{2}{3} \cdot \dfrac{\Delta(\ln k_2 - \ln k_1)}{\Delta\left(\frac{1}{k_B T}\right)} \end{cases} \Rightarrow \begin{cases} E(L_s) = \frac{1}{3}(E_{att} - E_{nuc}) \\ E(N_s) = -\frac{2}{3}(E_{att} - E_{nuc}) \end{cases}.$$

The derived $E(N_s)$ is simply negative twice $E(L_s)$: $E(N_s) = -2E(L_s)$, which is a direct consequence of ignoring the temperature-dependence of the saturated coverage. Recall that the coverage growth equation for $p = 1$ has the closed-form expression:

$$\frac{d\theta}{d\beta} = 3\theta^{2/3}(1-\theta),$$

which corresponds to the following equation with dimensions:

$$\frac{d\Theta}{dt} = \frac{3}{\sqrt[3]{4}} k_1^{\,2/3} \cdot k_2^{\,1/3} \cdot \Theta^{2/3}(\Theta_s - \Theta).$$

The inflection point of the $\Theta(t)$ curve is determined by

$$\left.\frac{d^2\Theta}{dt^2}\right|_{\Theta=\Theta_i} = 0 \quad \Rightarrow \quad \Theta_i = \frac{2}{5}\Theta_s,$$

which indicates that the maximum coverage growth rate at the inflection point is:

$$\left(\frac{d\Theta}{dt}\right)_{\max} = \left.\frac{d\Theta}{dt}\right|_{\Theta=\Theta_i} \propto k_1^{\,2/3} \cdot k_2^{\,1/3} \cdot \Theta_s^{\,5/3}.$$

Similarly the activation energy for the coverage growth rate is:

$$E_{cov} = -\frac{\Delta\left(\ln\left(\frac{d\Theta}{dt}\right)_{\max}\right)}{\Delta\left(\frac{1}{k_B T}\right)} \approx -\frac{1}{3}\cdot\frac{\Delta\left(2\ln k_1 + \ln k_2\right)}{\Delta\left(\frac{1}{k_B T}\right)} \quad \Rightarrow E_{cov} = \frac{1}{3}\left(2E_{att} + E_{nuc}\right).$$

APPENDIX 4 KINETICS-CONTROLLED DOMAIN OUTLINES

The 2D kinetic equations for the edge-attachment-controlled growth are (in the polar coordinates):

$$\begin{cases} \dfrac{dL(\theta,t)}{dt} = \dfrac{1}{2}\cdot\{k_{att}(\theta)\cdot[C_0 - \rho_G \cdot N(t)\cdot A(t)] - r_{growth\_etch}(\theta)\} \\ \dfrac{dN(t)}{dt} = k_{nuc}\cdot[C_0 - \rho_G \cdot N(t)\cdot A(t)] - r_{nucleus\_etch} \\ \\ A(t) = \int_0^{2\pi} \dfrac{1}{2}\cdot L(\theta,t)^2\, d\theta \\ L(\theta, t=0) = F(\theta) \\ N(0) = 0 \end{cases} . \qquad (A4.1)$$

The 2D kinetic equations for the diffusion-controlled growth are (in the polar coordinates):

$$\begin{cases} \dfrac{\partial C(\vec{r},t)}{\partial t} = D(\theta)\cdot\nabla^2 C(\vec{r},t) \\ \left(\rho_G - C_I(\theta,t)\right)\dfrac{dL(\theta,t)}{dt} = D(\theta)\cdot\left.\dfrac{\partial C(\vec{r},t)}{\partial \vec{g}}\right|_{\vec{r}=(L(\theta,t),\theta)} - E \end{cases} . \qquad (A4.2).$$

Upon the onset of diffusion, the nucleus grows faster along the A-equivalent orientations than along the B-equivalent orientations because

$$\begin{cases} D(\theta_A) > D(\theta_B) \\ \left.\dfrac{\partial C(\vec{r},t)}{\partial \vec{g}}\right|_{\vec{r}=(L(\theta_A,t),\theta_A)} \approx \left.\dfrac{\partial C(\vec{r},t)}{\partial \vec{g}}\right|_{\vec{r}=(L(\theta_B,t),\theta_B)} \end{cases} .$$

The anisotropy of the diffusion-driven growth rate will lead to the anisotropy of the domain shape. The initial circular domain outline consequently becomes elongated along the fast-orientation relative to along the slow-orientation as shown in Figure 6.16(ii). Such an anisotropic growth rate can be continuously maintained. To see this we note that the initial gradient of the hydrocarbon flux is roughly equal along A to along B while the diffusion coefficient along A is much larger than along B. Hence the Fick's second law of diffusion, $\dfrac{\partial C}{\partial t} = D(\theta)\cdot\nabla^2 C$, dictates that the local consumption rate of

the hydrocarbons at the tip of A is faster than at B: $\left.\frac{\partial C}{\partial t}\right|_A > \left.\frac{\partial C}{\partial t}\right|_B$. The local concentration at A is thereby lower than at B: $C(A,t) < C(B,t)$. The average directional derivative of the concentration field along A from the domain tip to a farther Cu surface region, where the concentration has not yet been noticeably influenced, is obviously larger than that along B:

$$\left(\left\langle \left.\frac{\partial C}{\partial \vec{g}}\right|_A \right\rangle \approx \right) \frac{C_{far} - C_A}{r_{far} - r_A} > \frac{C_{far} - C_B}{r_{far} - r_B} \left(\approx \left\langle \left.\frac{\partial C}{\partial \vec{g}}\right|_B \right\rangle \right)$$

since $C_{far} - C_A > C_{far} - C_B$ and $r_{far} - r_A < r_{far} - r_B$. An direct consequence of this inequality relation is that the average growth rate shortly after the current moment is still expected to be higher along A than along B because the growth rate is basically proportional to the hydrocarbon flux:

$$\frac{dL(\theta,t)}{dt} \cdot \left(\rho_G - C_I(\theta,t)\right) \propto D(\theta) \cdot \left.\frac{\partial C\left(\vec{r},t\right)}{\partial \vec{g}}\right|_{\vec{r}=\left(L(\theta,t),\theta\right)} .$$

Although the pre-factor $\rho_G - C_I(\theta,t)$ is larger at A than at B, their magnitude difference is much smaller than that between $D(\theta_A)$ and $D(\theta_B)$, because $C_I(\theta,t)$, the remaining concentration after nucleation has largely consumed the local hydrocarbons, is significantly lower than ρ_G . Therefore it is reasonable to claim that $\frac{dL(\theta_A,t)}{dt} > \frac{dL(\theta_B,t)}{dt}$, i.e., the growth rate anisotropy can be continuously maintained.